

Surface Plasmons in Sub-wavelength Structures from Near Infrared to Terahertz Range

ZHANG, Zhongxiang

A Thesis Submitted in Partial Fulfillment
of the Requirements for the Degree of
Doctor of Philosophy
in
Electronic Engineering

The Chinese University of Hong Kong
September 2011

UMI Number: 3504713

All rights reserved

INFORMATION TO ALL USERS

The quality of this reproduction is dependent on the quality of the copy submitted.

In the unlikely event that the author did not send a complete manuscript and there are missing pages, these will be noted. Also, if material had to be removed, a note will indicate the deletion.



UMI 3504713

Copyright 2012 by ProQuest LLC.

All rights reserved. This edition of the work is protected against unauthorized copying under Title 17, United States Code.



ProQuest LLC.
789 East Eisenhower Parkway
P.O. Box 1346
Ann Arbor, MI 48106 - 1346

ABSTRACT OF THESIS ENTITLED:**Surface Plasmons In Sub-Wavelength Structures From Near
Infrared To Terahertz Range****Submitted by ZHANG Zhongxiang**For the degree of Doctor of Philosophy in Electronic Engineeringat The Chinese University of Hong Kong in December 2011

Surface plasmons, also known as surface plasmon polaritons (SPP), belong to a kind of electromagnetic waves existing on the interface between metal and dielectric. In general, a metal's intrinsic plasma frequency is in the ultraviolet or visible range. The incident electromagnetic wave is highly localized at the metal-dielectric interface when its frequency gets close to the plasma frequency. According to the dispersion relationship, the confinement breaks down when the propagation constant is reduced at low frequencies from near infrared to terahertz range, where the permittivity of metals described by the Drude Model is much larger than that in the UV and visible range.

The introduction of roughness on a smooth metal surface provides a way to modify the terahertz wave behavior at the metal-dielectric interface. This idea has led to the research on the designs of structures which produce "spoof plasmons" and extraordinary transmission in the optical and terahertz ranges. We demonstrate a 3-dimensional (3D) structure composed of two metallic layers of complementary cross patterns sandwiching a polyimide dielectric. Three transmission peaks in the terahertz range are clearly observed experimentally for devices with different dimensions of the same structure. These resonant peaks agree very well with those

obtained from simulation. A simplified dual-layer metallic structure then is developed to demonstrate polarization-dependent plasmonic coupling. They exhibit polarization-dependent transmittance with large extinction ratios. Simulation and experimental results on structures with different wire-to-hole orientations provide strong evidence that the resonance peaks are caused by plasmonic coupling between the two metallic layers. A simplified *LC*-circuit model is proposed to explain the coupling mechanism and to estimate the peak frequencies. Our results suggest that specific electromagnetic response can be achieved by appropriate design of the geometrical patterns on the two metallic layers and a suitable polarization of the incident wave. The phase response of the structure is studied and 2π phase shift is found in this structure which depends on the dimension of the structure. The devices may help the design of multi-mode THz filters, THz waveguide, THz wave plate, THz planar lens etc.

An important future application of SPPs may be the integration of photonic and electronic circuits at nanometer-scale dimensions. In order to achieve that goal, plasmonic waveguides are indispensable. Initial studies of SPPs on metal films have stimulated the search for methods of transmitting SPPs in tiny waveguides such as metallic nanowires, SPP band gap structures, nano-particle chain arrays, metal stripe waveguide and hybrid plasmonic waveguide consisting of a dielectric wire placed close to a metal surface. The hybrid waveguide has been further developed into a plasmon nanolaser. To develop high-performance sub-wavelength scale plasmon waveguide, we propose a nano-scale fiber with embedded metal wires and

show by simulation that a hybridization of the gap plasmon mode and the single-wire SPP mode can produce a low-loss plasmonic waveguide mode. Our approach demonstrates how complex plasmonic structures can be realized by versatile fiber technology to achieve a good balance between confinement and loss.

The research on plasmon waveguide would provide a straight-forward way to access better lasing scheme. Quantum cascade laser (QCL) emits in the mid- to far-infrared and terahertz range. The repeated stack of semiconductor multiple quantum well heterostructures provide the gain media in this spectral range. In this thesis, we also demonstrate how plasmonic structures can be used to improve the performance of a QCL in mid-infrared to terahertz range.

摘要

表面等離子體，也被稱為表面等離子激元，是一種存在于金屬與介質界面的一種電磁波。通常金屬本征等離子體共振頻率是在紫外或者可見光波段。當入射的電磁波頻率接近等離子體共振頻率時就會被高度局域化在金屬介質分界面。在低頻率區域如近紅外到太赫茲波段，金屬的介電常數比在可見光和紫外波段要大很多。根據色散關係，在這些波段範圍，因為傳播常數的變小，表面波的限制性將被打破。

在金屬光滑表面引入的不平整提供了一種在金屬介質分界面改變表面波行為的方法。這個想法引發了在光和太赫茲波段對“偽表面等離子體”和超常透射的研究。我們實現了一種由雙層的三維的結構，這種結構由兩層互補的金屬十字圖案夾著一塊聚酰亞胺薄膜組成。在太赫茲波段，我們在這種不同尺寸的結構中清晰觀察到了三個共振峰。這些共振峰與仿真結果吻合的很好。在此基礎上，我們提出了一種簡化的偏振相關的雙層金屬結構實現同樣的表面等離子體耦合。這種結構表現出偏振相關的高消光比的穿透特性。對於具有不同的金屬線-孔夾角的結構的研究結果表明，這些共振峰是由兩層金屬間的表面等離子體耦合產生的。我們提出了簡化的 L-C 電路模型來解釋這種耦合機制和估算共振峰的位置。我們的結果表明特定的電磁響應可以通過對結構的合理設計和調整入射光的偏振來實現。同時，我們對互補結構的相位響應作了研究，結果表明了在那種結構中通過改變結構尺寸可以實現 2π 的相位偏移。該種結構可以被做成多模太赫茲濾波器、太赫茲波導、太赫茲波片、太赫茲平面透鏡等。表面等離子體激元的一個重要應用是在納米尺度的光電集成。為了開發一種高性能的亞波長表面等離子體波導，我們提出了一種在納米光纖中嵌入金屬線的

設計。仿真結構表明，在這種結構中，gap plasmon 模式和單一金屬線的等離子體激元模式的混合可以產生一種損耗很小的表面等離子體波導模式。我們的方法在成熟的光纖技術中實現通過設計複雜的等離子體結構實現波導限制與損耗的平衡。

對於波導的研究通過加入增益介質可以直接提供一種激光設計。量子級聯激光器在中紅外和遠紅外波段發射激光，重複地疊加量子井結構可以在這個波段提供增益介質。在本文中，我們研究了如何通過表面等離子體結構提高中紅外與太赫茲量子級聯激光器的性能。

Acknowledgements

I would like to express my gratitude to all those who gave me the possibility to complete this thesis and make my PhD study fruitful.

I am deeply indebted to my supervisor Prof. K.T. Chan, who trained me to be a good researcher during the past 4-year PhD study. His expertise and research insight guided me into the field of plasmonics, which is a topic well worthy of study and fits my background and interest. He taught me how to find out the problems and solve the problems as a PhD. He showed me how to think like a good researcher and guided me to gain a systematic practice on experimental techniques. His useful suggestions always make me out of confusion and his kindness always encourage me to overcome the obstacles in both research and life. Especially, I really appreciate his great support to my research activities in the past 4 years. These visiting activities will be important parts of my life experience but not just research.

I really want to thank Prof. Y.C. Huang in National Tsinghua University as much as possible. He really impressed me during my first visit to Taiwan in 2006 for his passion on research and kindness to students. He has very clear concepts on fundamentals and deep insight into his research area, which make me learn a lot during the discussion with him. He is also a very good friend in life when I lived in Taiwan.

I would like to thank Prof. Federico Capasso and Dr. N.F. Yu in Harvard School of Engineering and Applied Science (SEAS) for accepting me as a visiting student to Harvard University. Prof. Capasso really impressed me by his passionate pursuit of high level research. His broad perspective makes me learn a lot during the discussion. Dr. Yu gave me many useful suggestions on research and spent so much time on discussion with me on my research topic. He also directly taught me some processes in the clean room for fabrications.

I am very thankful to Prof. S.L. He in Zhejiang University for his helpful discussion on my research topic and hosting my visit to his group in 2009. He is a very active researcher and very nice to his students as a group leader.

I also like to thank Prof. M.L. Hu in Tianjin University for his useful guidance and discussion in my research topics. His is an expert in fiber optics and his wealthy knowledge helps me a lot during discussion. He is also a very good friend of mine in life.

I am also grateful to Prof. Chester Shu and Prof. H.K. Tsang in Opto lab in CUHK for their kindly concern and help. Prof. Shu gave me great help and support during the application for the visiting program. I am very thankful to Prof. J.B. Xu and Prof. Aaron Ho in Solid State lab.

They gave me very useful suggestions on my research during my qualify exam. Prof. J.B. Xu also taught me a lot during my taking his course on nano electronics.

I wish to express my appreciation to Prof. C.L. Pan in National Chiao Tung University in Taiwan for his great help with measuring my first batch of samples in THz-TDS system. He also taught me a lot during his course on ultrafast optics. I also wish to thank Prof. C.W. Chow for his providing some instruments when I was in Taiwan.

I would like to thank Ms. L.C. Ho in Opto lab for her great help on the technical issues during my experiments. She gave me many useful suggestion and assistance in many details. I also want to express my appreciation to Dr. W.Y. Cheung for his great help in micro fabrication techniques. He taught me many tricks in fabrication. I wish to thank Mr. M.T. Yeung and Mr. Albert Wong for their assistance in the clean room.

I wish to thank my colleague Miss M.Y. Chen for her helpful discussion on metamaterials and great help with the sample fabrication. I also want to thank Dr. K.J. Chen for his patient instruction on how to handle some THz components. I would like to express my thanks to Dr. C.M. Sun for his great effort on testing the photoconductive antennas in THz-TDS system. I would like to thank Dr. H. He and Dr. T. Yang for their great help in lab and my living in Hong Kong. I would like to thank Mr. J.B. Du, Mr. Y.H. Dai and Mr. K.P. Lei for their useful instruction on fiber handling and instrument usage. I wish to thank Dr. X. Chen for his useful discussion on waveguide. Besides, I want to thank Miss J.J. Liu, Mr. Z.L. Ma in our group for their kind help. Sincere thanks are extended to Dr. L. Xu, Mr. Chris Wong, Mr. L. Wang, Miss K.Y. Fung, Mr. M.G. Lo and Miss X.L. Fu and all other lab members.

My keen appreciation goes to Miss Y.X. Cui in Zhejiang University for her useful discussion on the CST simulation. I am grateful to Dr. C.L. Wang in Tianjin University for his help with the measurement in THz-TDS and useful discussions. Sincere thanks are extended to Dr. Y.J. Song who taught me how to operate Ti:Sapphire laser. I also wish to thank Dr. T.D. Wang, Dr. S.T. Lin and Dr. H.L. Chang in NTHU for their great help in lab during my studying in Taiwan. Besides, I would like to thank Dr. J. Lin, Dr. S. Menzel, Mr. M. Kats and Mr. R. Blanchard in Harvard University for help with fabrication and discussion.

Finally, I would like to express my heartfelt gratitude to my parents and my brother. Thank you for making my world a better place to be and witnessing each step of my growth. You have all my honors.

Thank you all!

Table of Contents

Abstract -----	i
Acknowledgements -----	vi
Table of Contents -----	viii
List of Tables and Figures -----	xi
List of Abbreviations -----	0
Chapter 1: Introduction -----	1
1.1 Introduction to surface plasmon-----	1
1.2 Surface plasmons in sub-wavelength structures-----	6
1.3 Organization of the thesis-----	11
References-----	16
Chapter 2: Surface plasmons in infrared range -----	22
2.1 Surface waves at the metal-dielectric interface-----	22
2.1.1 Drude model and metal-----	22
2.1.2 Propagation of surface plasmons on metal surface-----	31
2.2 Spoof surface plasmon-----	35
2.3 Introduction to THz wave and THz-TDS-----	39
2.3.1 THz wave and THz-TDS system-----	39
2.3.2 Applications of THz-TDS on spoof surface plasmon-----	45
2.4 Summary-----	53
References-----	54
Chapter 3: THz transmission in plasmonic structures -----	57
3.1 Introduction-----	57
3.2 Multimode transmission in complementary plasmonic structure-----	59
3.2.1 Mode splitting due to the coupling-----	60
3.2.2 Bloch state in periodic structures-----	66
3.3 Polarization-dependent plasmonic coupling in dual-layer structure-----	69
3.3.1 Polarization-sensitive transmission-----	69

3.3.2 LC circuit model -----	73
3.4 Phase response of dual-layer structure-----	78
3.4.1 0-to- 2π -phase-shift due to the coupling -----	79
3.4.2 Planar phase engineering devices-----	80
3.5 Summary -----	83
References -----	85
Chapter 4: Plasmon waveguide and cavity-----	88
4.1 Introduction to plasmon waveguide-----	88
4.2 Plasmonic waveguiding in a hexagonally ordered metal wire array--	89
4.2.1 Metal wire array in fiber -----	91
4.2.2 Propagation and dispersion-----	93
4.3 Plasmonic cavity -----	101
4.3.1 Plasmonic ring cavity based on long-ranged plasmon waveguide-----	102
4.3.2 Biosensor based on plasmonic cavity -----	103
4.4 Summary -----	108
References -----	110
Chapter 5: Active Plasmonics-----	115
5.1 Introduction -----	115
5.2 Quantum cascade laser in mid-IR and THz range-----	117
5.2.1 Introduction -----	117
5.2.2 Laser fabrication and characterization-----	120
5.3 Plasmon laser based on 1D deep subwavelength grating-----	124
5.3.1 Dispersion tailoring-----	125
5.3.2 Group velocity and loss -----	130
5.4 Summary -----	135
References -----	136
Chapter 6: Conclusions and Future Work -----	139
6.1 Conclusions -----	139

6.2 Future Works	140
6.2.1 Phase engineering devices in THz range	140
6.2.2 Passive and active sensor in infrared range	141
6.2.3 Nonlinearity in plasmonic structures	143
References	145
Publication List	146

List of Tables and Figures

Table 2-1 Drude model parameters for metals

Table 3-1 Parameters in LC-circuit Model

Fig. 1-1 Lycurgus cup without (left) and with (right) light passing through the glass.

Fig. 1-2 The annual numbers of the publication related to “surface plasmon”.

Fig. 1-3 Schematic representation of the surface plasmon propagating along the metal-dielectric interface. The exponential dependence of the electromagnetic field intensity on the distance away from the interface is shown on the right.

Fig. 1-4 Structure of the thesis shown by flow chart.

Fig. 2-1 (a) Driven by external electric field, the free electrons in metal form the current density J ; (b) The schematic of the motion for electrons in metal; (c) When bound electrons in lattice respond to the external electric field, the temporary separation of positive and negative charges forms the polarization.

Fig. 2-2 The validity limits of Drude model.

Fig. 2-3 (a) The real and imaginary parts of Al, Ag, Au and Cu in wide frequency range; Zoom view of the curve in low frequency range of the real part (b) and imaginary part (c).

Fig. 2-4 The discontinuity of E_z at the interface between metal and dielectric.

Fig. 2-5 Dispersion configuration of SPs at single metal-dielectric interface.

Fig. 2-6 (a) 1-D array of grooves; (b) Effective medium approximation.

Fig. 2-7 Dispersion relation of the spoof SPs in a groove array.

Fig. 2-8 Electric field of a measured THz pulse and the simulated field of the exciting optical pulse are shown in (a), whereas the amplitude spectrum is shown in (b).

Fig. 2-9 Schematic of bowtie photoconductive antenna (left-hand side) and THz wave generation pumped by a femtosecond laser pulse with 800nm wavelength (right-hand side).

Fig. 2-10 Schematic of the coupling between THz emitter and detector.

Fig. 2-11 The sampling process of THz pulse by using femtosecond optical pulse.

Fig. 2-12 Schematic of THz_TDS setup.

Fig. 2-13 Typical output of THz_TDS setup.

Fig. 2-14. (a) Schematic of the structure; (b) Experimental result from THz-TDS and the simulation result; (c) and (d) the surface current distributions of the two metal layers at 0.36THz.

Fig. 2-15 Magnetic and electric resonant frequencies versus (a) L at $W=76\mu\text{m}$, $P=402\mu\text{m}$; (b) W at $L=260\mu\text{m}$, $P=402\mu\text{m}$; and (c) P at $L=260\mu\text{m}$, $W=76\mu\text{m}$.

Fig. 2-16 (a) The schematic of the fishnet structure. (b) The measured transmittance of the sample with thickness of $PI=12.5\mu\text{m}$ under different incident angles. (c) The measured transmittance of the samples with different thickness of PI under the 200 incident angle. The dips in the grey regions are the two MPP modes and the main peak corresponds to the electric resonant mode.

Fig. 2-17 Dispersion of the MPP modes.

Fig. 3-1 Free Standing Terahertz Bandpass Filter (Measurement Result and Simulation Result).

Fig. 3-2 (a) Schematic of the complementary structure. G , K and J denote the period of the structure, the member length and the member width of the cross, respectively. Measured and simulated transmittance through the structure for samples with $(G, K, J) = (301, 195, 29)\mu\text{m}$ (b) and $(402, 260, 76)\mu\text{m}$ (c). The dashed lines show the resonant frequency for the single layer case. Wood's anomaly is indicated by★.

Fig. 3-3 (a) and (b): The simulated current distributions calculated by CST Micro Wave Studio for the ω_- and ω_+ modes, respectively; (c) and (d): a pictorial pattern of the magnetic field corresponding to the ω_- and ω_+ modes, respectively, in the cross-section plane XX' .

Fig. 3-4 Simulated transmission characteristics of Sample A as a function of dielectric thickness H . The circles indicate the resonant frequencies of Sample A_S.

Fig. 3-5 (a) Transmission curve measured in a THz-TDS system with beam waist around 0.8mm; (b) The simulated current distributions for the ω_C mode; (c) Simulated transmission curves for samples with different unit cell periods but the same patterned shape and size as Sample A.

Fig.3-6 Schematic of the wire-hole structure. (a) 3-dimensional view; (b) x-y plane view; and (c) y-z plane view.

Fig. 3-7 Experimental and simulation result for (a) $\beta = 0^\circ$, $E//\text{wire}$; (b) $\beta = 60^\circ$, $E//\text{wire}$; (c) $\beta = 90^\circ$, $E//\text{wire}$; (d) $\beta = 0^\circ$, $E\perp\text{wire}$; (e) $\beta = 60^\circ$, $E\perp\text{wire}$; and (f) $\beta = 90^\circ$, $E\perp\text{wire}$. The blue curves in (a)-(c) show the transmittance obtained by using LC-circuit model.

Fig. 3-8 (a) Inductively coupled LC-circuit for the structure; (b) Equivalent circuit with additive magnetic coupling; (c) Equivalent circuit with subtractive magnetic coupling; (d) Magnetic field distribution for (b); and (e) Magnetic field distribution for (c).

Fig. 3-9 State transition by changing β for (a) $E // \text{wire}$ and (b) $E \perp \text{wire}$.

Fig. 3-10 (a) Amplitude and (b) phase response of the complementary structure with substrate.

Fig. 3-11 Electric field in the structure for complementary structure (a) at the frequency without phase shift; (b) at the frequency with phase shift.

Fig. 3-12 (a) Fabrication process; (b) SEM image of the fabricated samples before a-silicon deposition.

Fig. 3-13 Reflection spectra for cross width $W=250\text{nm}$ with different cross length L .

Fig. 4-1 Basic surface plasmon models: (a) metal-insulator interface; (b) MIM structure; (c) IMI structure.

Fig. 4-2 A stack of glass tubes and rods (a) is constructed as a macroscopic "preform" with the required photonic crystal structure. It is then fused together and drawn down to fiber (c) in two stages using a standard fiber drawing tower. To soften the silica glass, the furnace (b) runs at 1800° to 2000°C .

Fig. 4-3 (a) 3-dimensional schematic of the metal wire array in fiber; (b) Cross section of the hexagonally ordered wires.

Fig. 4-4 Calculated modal profiles are shown for: (a) $d=40\text{nm}$; (b) $d=110\text{nm}$; (c) $d=130\text{nm}$; (d) $d=160\text{nm}$. And $s=200\text{nm}$. The white arrows in (a)-(d) represent the orientation of the electric field.

Fig. 4-5 (a) The real and imaginary parts of the effective mode index versus the diameter of the metallic wire. Inset: FOM versus the diameter d . **(b)** Calculated propagation length versus the diameter of the metal wire for the separation $s=200\text{nm}$, 300nm , 400nm and the single wire.

Fig. 4-6. The dispersion relations of the waveguide modes for $d = 20\text{nm}$ (wire modes ■ ● ▲ ▼ ◆ ☆), 130nm (hybrid modes ■ ◆ ▲ ▼ ◆ ☆) and 195nm (gap modes □ ○ △ ▽ ◆ ☆). The grey region is the silica light cone.

Fig. 4-7 Higher order modal profiles for $d=130\text{nm}$ and $s=200\text{nm}$ with different mode index.

Fig. 4-8 Broken of symmetry. **(a)** Random distributed nano wires; **(b-f)** 6-fold rotational symmetry is broken by taking out the wires one by one.

Fig. 4-9 Different optical microcavities with different Q_s and V_s , depending on the confinement methods.

Fig. 4-10 WGM in microtoroid dielectric cavity.

Fig. 4-11 Photonic and plasmonic coupled modes in plasmonic WGM cavity.

Fig. 4-12 Excitation of surface plasmon on smooth metal surfaces by **(a)** Kretschmann configuration and **(b)** Otto configuration. **(c)** Surface plasmon resonance biosensor: principle of operation.

Fig. 4-13 (a) 3-D and **(b)** top view of the SPR sensor element.

Fig. 5-1 (a) Interband transition in conventional semiconductor laser; **(b)** intersubband transition in quantum cascade laser.

Fig. 5-2 QCL with bound-to-continuum design for broad gain at $10\mu\text{m}$ wavelength.

Fig. 5-3 Fabrication of nano grating on active region of QCL.

Fig. 5-4 Fabrication process for mid-IR QCL

Fig. 5-5 FTIR manufactured by Bruker Inc.

Fig. 5-6 Propagation and emission in QCL waveguide.

Fig. 5-7 (a) Model setup in FDTD. **(b)** Propagation of spoof surface plasmon in QCL.

Fig. 5-8 Simulation setup for calculating the dispersion of the metallic grating in Lumerical FDTD.

Fig.5-9 Simulated dispersion relation for 500nm -pitch grating with depth= **(a)** 250nm ,

(b) 400nm, (c) 500nm.

Fig. 5-10 (a) The simulation result (color 3D image) and Drude model fitting curve (white line) for 500nm-pitch grating with depth=500nm. (b) Propagating length in different groove depth.

Fig. 5-11 (a) The simulation result (color 3D image) and Drude model fitting curve (white line) for 5um-pitch grating with depth=3um. (b) Group velocity and propagating length v.s. frequency.

Fig. 5-12 (a) SEM image of the SPASER chips; (b) Initial measurement result for the chip with 4.2um-depth grooves.

Fig. 6-1 $\lambda/4$ wave plate.

Fig. 6-2 Fluidic detection limits for protein sensing.

Fig. 6-3 Gratings in a metal surface can enhance nonlinearity originated from intense field enhancement involving both localized and propagating surface plasmons. (a) Light is coupled into a localized nanocavity mode, assisted by propagating surface plasmons (red wavy arrows). (b) An emitter positioned in a groove exhibits enhanced emission and collimation effect. (c) Schematic of the four-wave mixing experiment.

List of Abbreviations

CST_MWS	Computer Simulation Technology Micro Wave Studio
EOT	Extraordinary Optical Transmission
EBL	Electron Beam Lithography
FWM	Four Wave Mixing
HFSS	High Frequency Structure Simulator
IMI	Insulator-Metal-Insulator
LSP	Localized Surface Plasmon
MIM	Metal-Insulator-Metal
NIM	Negative Index Materials
PCF	Photonic Crystal Fiber
PEC	Perfect Electric Conductor
PECVD	Plasma Enhanced Chemical Vapor Deposition
PI	Polyimide
PL	Photo Lithography
PNCG	Plasmonic Nano Cavity Grating
PR	Photo Resist
RIE	Reactive Ion Etching
SERS	Surface Enhanced Raman Scattering
SP	Surface Plasmon
SPP	Surface Plasmon Polariton
SPR	Surface Plasmon Resonance
TE	Transverse Electric
THz-TDS	Terahertz Time Domain Spectroscopy
TM	Transverse Magnetic
WGM	Whispering Gallery Mode

Chapter 1: Introduction

1.1 History and Development of Surface Plasmon

Surface plasmon (SP) is a rapid developing research area which has been applied in many fields such as nanophotonics, biosensor, Surface Enhanced Raman scattering (SERS), photonic circuits, semiconductor nanofabrication, microscopy, display technology et al. SPs are collective charge oscillation which occur at the dielectric and conductor interface. Mathematically, the wave function of the surface plasmons originates from the opposite sign of the real part of permittivity across the interface. Compared with bulk or volume plasmons which are also called plasma or electron gas, SPs have lower energy. When SPs are coupled with photons, the resulting surface wave generating at the interface is called surface plasmon polariton (SPP). In the past decade, SPP has attracted many researchers' attention for its potential to demonstrate the integration of optical and electrical systems and enable a wider scope to understand the interaction between photon and electrons with abundant physics.

Though the scientists began to study the surface plasmon at the beginning of twentieth century, the unique properties of surface plasmon had been employed by ancient people. A very good example is the Lycurgus cup, which dates from 4th century AD. The cup is made from dichroic glass - it is a jade green color but it turns to ruby red if held to light. The cup gets its name from the depiction of the

triumph of Dionysus over Lycurgus from the 6th book of Homer's Iliad. The cup is in the British museum, London. It is shown by Fig. 1-1. The scientific investigation on surface plasmons dates back to early twentieth century. In 1902, Robert W. Wood observed the uneven distribution of light in the reflection measurements on metallic gratings [1]. Later soon in 1904, based on the development of Drude model for metal [2, 3] and electromagnetic theory of "Rayleigh scattering" raised by Lord Rayleigh, Maxwell Garnett described the bright colors observed in metal glasses and metallic films, which is the earliest scientific work trying to study the nano metallic particles [4]. At the same year, Lord Rayleigh earned the Nobel Prize for Physics for his discovery of element Argon. Rayleigh also discovered the phenomenon now called Rayleigh scattering, explaining why the sky is blue, and predicted the existence of the surface waves now known as Rayleigh waves. In the year 1908, Gustav Mie published his famous theory for the light scattering by spherical particles, which is named "Mie scattering" [5].

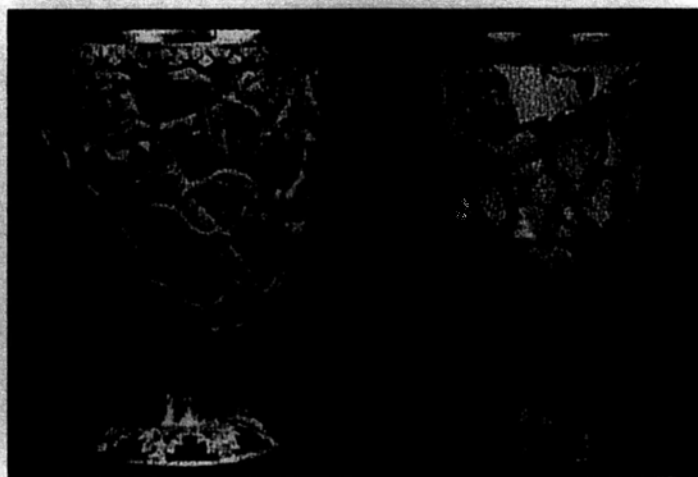


Fig. 1-1 Lycurgus cup without (left) and with (right) light passing through the glass.

In the following almost fifty years, no significant progress was made on the

theory related to surface plasmon. Until 1956, David Pines tried to study the origins of the loss in metal [6]. David described the intrinsic energy loss experienced by fast electron traveling through metals and gave out the concept that the collective oscillation of the free electrons in metals would introduce losses. This kind of oscillation was named "plasmon". Another famous researcher, Robert Fano, introduced the concept of "polariton" to describe the interaction between the bound electrons and the incident light [7]. Fano is famous for "Fano resonance", whose line-shape is due to interference between two scattering amplitudes. One is due to scattering within a continuum of states (the background process) and the second due to a excitation of a discrete state (the resonant process). A milestone was made by Rufus Ritchie in 1957. Ritchie published his work in this year to show that the plasmon modes can exist on the dielectric-metal interface and discuss the loss in metallic thin films [8]. This is the first theoretical study on surface plasmon. In 1968, Ritchie and his coworkers published their work to describe the Wood's anomaly for metal grating by introducing the theory of surface plasmons [9]. It has been almost seventy years after Wood observed the unexplained features on metallic gratings. Another milestone made in this year was from Andreas Otto, Erich Kretschmann and Heinz Raether. They presented their methods to excite the surface plasmons on metal film by frustrated total reflection [10, 11]. Until now, this is the most popular commercialized design in the application of surface plasmon sensor.

By the year 1968, it seems that all the theoretical issues for surface plasmon had been solved. Actually, another important branch for the research of surface plasmon

has not been paid much attention to, which was described by Maxwell Garnett in 1904. This will lead to broad applications for localized surface plasmon (LSP) in biophotonics and nanophotonics. In 1970, Uwe Kreibig and Peter Zacharias tried to compare the electronic and optical response of gold and silver nano particles [12]. This is the first description of the optical response of nano particles by introducing the theory of surface plasmons. In 1974, Stephen Cunningham and his coworkers raised the term of “surface plasmon polariton” (SPP) which emphasized the coupling between light wave and oscillating electrons and reflect the hybrid nature [13]. In this year, another important work was done by Martin Fleischmann and his coworkers. They observed strong Raman scattering from pyridine molecules in the vicinity of roughed silver surface [14]. This was the first presentation of the enhancement of Raman scattering by the surface plasmons. But they did not realized theoretical explanation at that time. This discovery led to another popular research field of the surface plasmons: surface enhanced Raman scattering (SERS). A systematic presentation of the diffraction of light by metallic gratings from the view of phase matching was made by H. Raether in 1988 [15]. The current research stage for surface plasmon had been set by all these efforts and discoveries.

To extend the study on surface plasmons from fundamental theory to applications, many research areas have been established in different technological fields including biosensor, photolithography, optical data storage, nano lasers et al to approach the physical limits. All these development leads to the notion of “plasmonics” which means a subject of metal-based optics and nanophotonics. The

first commercialized surface-plasmon-based biosensor was developed in 1991. Large amount of papers were published on bio sensor in the coming decade. In 1997, Junichi Takahara and his coworkers presented the surface plasmon waveguide in nano scale based on metallic nano wire [16]. Later in 1998, Ebbesen and his coworkers reported the discovery of optical extraordinary transmission (EOT) in the periodic subwavelength structures [17]. This work stimulated large amount of publications on EOT and subwavelength structures. A brief review will be given on this area in Chapter 2. In 2001, J.B. Pendry suggested that a thin metallic film can demonstrate a “perfect lens” to overcome the diffraction limit of traditional lens [18] by introducing the concept of “negative refraction”. This kind of perfect lens was experimentally demonstrated by Xiang Zhang and his coworkers by a silver thin film in 2005 [19]. To extend the application of the lens from near field to far field, hyperlens was developed by the same group in 2007 [20]. Another popularly investigated area is cloaking which is predicted by J.B. Pendry in 2006 [21] and experimentally demonstrated in microwave range at the same time [22]. Tremendous publications form the explosive areas of metamaterials and transformation optics.

The rapid development of the research on surface plasmon can be reflected by the growth of the publications. A simple statistic is performed on the website of ScienceDirect (<http://www.sciencedirect.com>) by searching the key word “surface plasmon”. The annual numbers of the related publication are shown by the column chart in Fig. 1-2. From this figure, we can see that during 1990s and 2000s, the

amount of the publications experiences an over five-time growth. In 2011, the number of the first four months has exceeded the half of 2010. The rapid development on this field in the past twenty years should attribute to the development of nano fabrication, imaging and analysis tools.

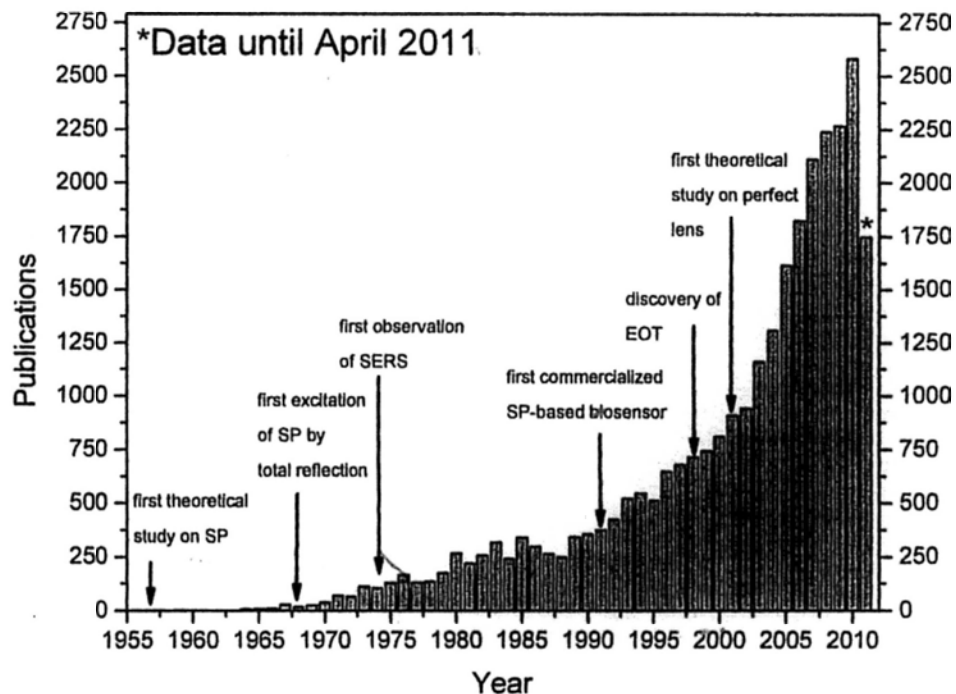


Fig. 1-2 The annual numbers of the publication related to “surface plasmon”.

1.2 Surface plasmons in subwavelength structures

Surface plasmons represent electromagnetic surface waves that have their intensity maximum in the surface and exponentially decaying fields perpendicular to it. It has lower energy than bulk (or volume) plasmons which quantise the longitudinal electron oscillations about positive ion cores within the bulk of an electron gas (or plasma). When surface plasmons couple with a photon, the

resulting hybridised excitation is called a surface plasmon polariton (SPP) [13]. This SPP can propagate along the surface of a metal until energy is lost either via absorption in the metal or radiation into free-space. Fig. 1-3 shows the schematic of the electron surface wave propagating along the metal-dielectric interface. The oscillation is coherent and coupled with the incident electromagnetic wave. The wave can be expressed by the equation:

$$E = E_0 \exp[-i(k_x x \pm k_z z - \omega t)]. \quad (1.1)$$

Here k_x and k_z are the k-vectors in x direction and z direction, respectively. And k_x and k_z has the following relation:

$$k_x^2 + k_{zi}^2 = \left(\frac{\omega}{c}\right)^2 \epsilon_i \quad (i=1,2). \quad (1.2)$$

Here ϵ_i means the permittivity of metal or dielectric shown in Fig. 1-3. The dispersion of surface plasmon defines that k_x is larger than the wave vector in dielectric. Then k_{zi} is an imaginary number and the electric field in z direction exponentially decays from the maxima at the interface:

$$E_z \sim \exp(-|k_z|z). \quad (1.3)$$

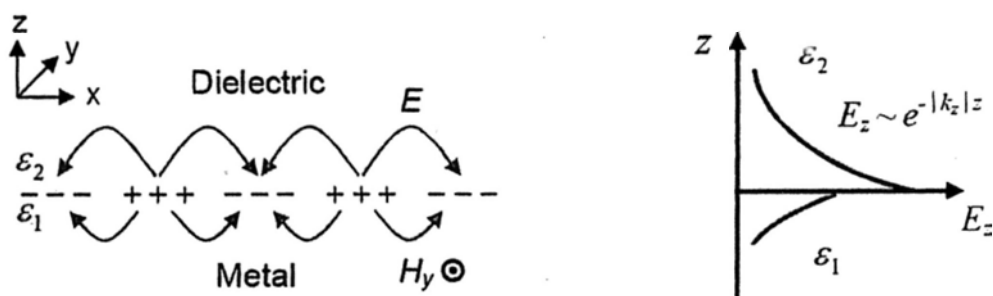


Fig. 1-3 Schematic representation of the surface plasmon propagating along the metal-dielectric interface. The exponential dependence of the electromagnetic field intensity on the distance away from the interface is shown on the right.

The most popular application for the surface plasmon at metal-dielectric interface is the SP-based biosensor, which has been commercialized. It seems that all the theory about SPs at the single interface has been clear and set the stage for the application. For most SP-based applications, we have to excite the surface wave and characterize it. To search diverse design and application for the devices, structures or roughness is introduced into the surface. A systematic study on rough surface was performed in 1988 [15]. Another reason for introducing the roughness is that it can convert the bounded surface wave (nonradiative) to radiative wave for the measurement. The metallic structures then provide a versatile platform for designing the devices for different applications.

The scattering of electromagnetic waves in periodic structures plays an important role in solid state physics or material science such as electron diffraction [23], light in photonic crystals [24, 25] et al. In the absence of nonlinear effects, the scattering light is defined by the shape and permittivity or permeability of the diffracting objects. When the object is larger than the concerned wavelength, then the problem would be classical ray scattering problem which can be solved by classical optics or electromagnetics. When the object is smaller than the wavelength, this is a subject we called "subwavelength optics". In this thesis, we focus on the light scattering by the planar or 3-dimensional metallic subwavelength structures, which have become a subject of intense research driven by the development of modern micro and nano fabrication technique.

As we mentioned before, the research on the metallic structures has begun at the

beginning of last century. Before that time, Babinet's study connected the shape of the objects with the reflected fields, which is called "Babinet's Principle" today [26]. Babinet's principle is also important for the discussion of metallic structures. Focusing on the arrays under normal incident, Wood's observation stimulated the discussion on diffraction of lights in gratings [1, 27, 28]. Rayleigh and Fano then tried to give out the interpretation for Wood's anomaly. Two types of anomalies were identified by Rayleigh and Fano respectively. The first one is called Rayleigh condition which shows that when a diffracted beam is incident to a grating surface, it will become grazing to the plane, which means that it is bounded at grating surface. The Rayleigh condition gives rise to the "bright band" in the structure. Another band called "dark band" is discovered by Fano showing up at the longer wavelength which cannot be excited by the optical signal even on resonance.

By the end of last century, a significant discovery, EOT, stimulated the research on this kind of periodic arrays. In 1998, Ebbesen and his coworkers [17] showed that periodic arrays of subwavelength holes in a metal film can transmit much more light than the expected amount predicted by Bethe in 1944 [29]. According to Bethe's theory, for large wavelength λ compared to the hole radius, the transmission of the incident light is proportional to $(b/\lambda)^4$. Ebbesen tried to explain EOT by using the theory of surface plasmon but this is still a subject of debate. Anyway, in the past decade, many researchers tried to solve this theoretical problem and find out the experimental verifications in different frequencies ranging from visible to far infrared. Most researchers tend to understand that EOT originates from

the interaction of the surface plasmon with the subwavelength holes [30-34]. But some others emphasize the dynamical light diffraction in the structure [35-38]. Some more studies in the longer wavelength, where the metal can be treated as perfect electric conductor (PEC), support the former explanations more in this argument [39-41]. Some more extensive researches focus on how the hole shape or periodicity affect the transmittance of the structures [40, 42]. The periodicity of the holes was thought crucial, but new experiments show that this is not so [43]. Though randomly distributed holes arrays with quasicrystal or approximate quasicrystal structure do. Microscopy theory for the EOT has given out the analytical expression for the transmission spectrum characteristics [44]. All these efforts are motivated by the potential applications of EOT in near-field optical microscopy, photolithography, displays and elsewhere.

When the single layer structures become well-investigated, double-interface and multi-interface structures come into view. The basis of the multi-layer structure is the coupling between the metal-dielectric interfaces. The simplest cases are the metal-insulator-metal (MIM) and insulator-metal-insulator (IMI) structures. The coupling results in the mode-splitting which lead to the symmetric and anti-symmetric modes [45]. Based on these simple models, tremendous amounts of designs were proposed and demonstrated combining with other popular research topics such as metamaterials, negative index materials (MIM) [46]. The localized plasmonic effect plays an important role in the resonant structures which demonstrate the negative refractive index. Among all the designs of negative-index

metamaterials (NIM) is the “fishnet” structure. This kind of structure aroused much interest because of their easy fabrication and convenient designs to achieve optimized properties. The design of fishnet structures has been primarily focused in both microwave and optical regimes. Furthermore, the inductor-capacitor (LC) circuit model which was proposed earlier [47, 48] in the microwave regime has been successfully verified. Even until today, the simple LC model is popularly used to understand the physics and electromagnetic dynamics in basic [49] or complex plasmonic structures. Besides negative refraction, the fishnet structure also finds application in magnetic plasmon polariton (MPP) nanolaser, waveguides, selective switches and etc. The dispersions of the magnetic and electric resonant modes are closely related to the mechanism of the coupling between the two metallic layers. The multiple MPP modes in the optical regime have been analyzed in the last three years [50, 51] and the results show abundant physics in the two-layer coupled system.

In summary, the research in surface plasmon provides versatile stage for the subject of subwavelength optics and metal optics. Many discoveries have provided novel designs for electromagnetic and integrated optical devices in this exploding field. But still there are many unclear issues whose solving may lead to optimal and ultra new devices, no matter in visible range or infrared range.

1.3 Organization of the thesis

The structure of this thesis is shown by the flow chart in Fig. 1-4. The excitation of the surface plasmon is a very important topic in the field of surface plasmon. The

structure can be treated as one method to excite the surface waves though the discussion is much more abundant. Besides the structure, there are a lot of other techniques to excite the surface waves, such as using particles to excite the localized surface plasmons, using prism to excite the propagating surface wave at metal-dielectric interface, highly focused optical beam et al. Our research is mainly performed in the infrared range with long wavelength. In this range, the properties of metal will evolve from lossy metal to perfect electric conductor. A powerful tool, terahertz time domain spectroscopy (THz_TDS) is setup and applied to characterize our samples.

In Chapter 1, a brief introduction to the history and development of surface plasmon is given. A selective review on the progress of surface plasmon in subwavelength structures which is related to our discussion is presented.

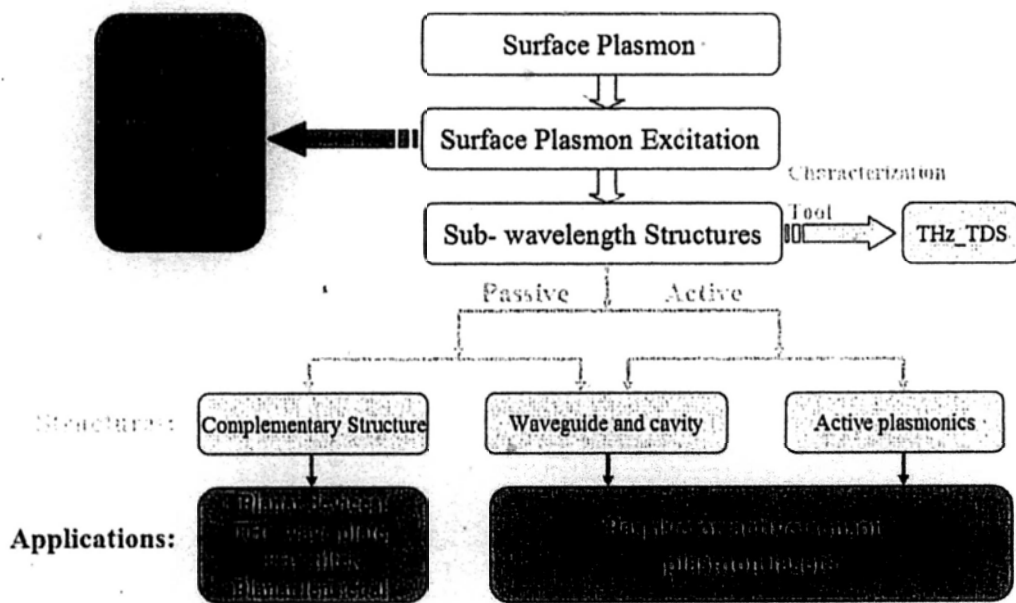


Fig. 1-4 Structure of the thesis shown by flow chart.

In Chapter 2, basic mathematics related to the calculation of surface plasmon is summarized. Drude model is introduced to show the difference in physics for the metal in visible range and infrared range. This difference will be reflected throughout our discussion of surface plasmons ranging from near infrared to far infrared. The dispersion of the metals or metallic structures plays a key role when discussing the mechanism of the propagating of the surface plasmon. Basic calculation about the dispersion relationship will be shown in this part. At the end of this part, terahertz wave will be introduced which is our discussion frequencies. The THz_TDS system will be described and some primary measurements on this system for some extension discussion on the fishnet structure will be performed.

In Chapter 3, we propose and demonstrate a 3-dimensional subwavelength structure with periodic complementary metal patterns operating in terahertz range. The multimode resonance due to the coupling of the two layers in this structure will be discussed. The polarization-dependent coupling is shown in a simplified wire-hole structure. We propose an LC-circuit model to explain the coupling mechanism. Our results suggest that specific electromagnetic response can be achieved by appropriate design of the geometrical patterns on the two metallic layers and a suitable polarization of the incident wave. At the end, the phase response of the complementary structure will be discussed. The 2π -phase-shift due to the coupling of the two layers will make the structure get broad potential

applications as phase modulation planar devices like THz wave plate, THz lens et al.

Plasmonic waveguide is a very important component for the application of surface plasmon, no matter for passive or active devices. In Chapter 4, a fiber-based plasmonic waveguide is presented. The inclusion of a structured pattern of nano-scale metal wires in a silica fiber to form a symmetric plasmonic waveguide is proposed. The surface plasmon polariton modes within the waveguide are studied by varying the wire diameter and wire spacing. Simulation results show that hybridization of the single-wire mode and the gap plasmon mode can yield a hybrid mode with optimum propagation lengths comparable to those reported for other structures but with better light confinement. The fiber can be easily doped with a gain material to offset the loss so that the resultant waveguide will be useful for integration with electronic circuits at nanometer dimensions. The discussion of the waveguide will go straightforward to the cavities. Plasmonic cavity is a very new and fertile field with a lot of unknowns to be explored. A high-Q plasmonic ring cavity with whispering gallery mode (WGM) will be discussed in this part which shows potential biosensor applications.

In Chapter 5, we focus on the gain mediums in the plasmon subwavelength structures. Loss is a very big problem which originates from the intrinsic property of metal and is a very big obstacle for the plasmonic applications. The quantum cascade semiconductor material will be introduced into the plasmonic structures in deep subwavelength. A tradeoff between the propagating group velocity and the loss

will be shown in the structure. The simulation result shows the possibility to obtain a low-threshold plasmon laser in mid infrared or terahertz range. The experimental technique and primary result will be shown.

Chapter 6 gives a summary on the whole work. Potential and current applications of related techniques are introduced, and some important works from other groups are also introduced. Then we propose some future works based on current results.

References

1. R.W. Wood, "On a remarkable case of uneven distribution of light in a diffraction grating spectrum," *Phil. Mag.* **4**, 396 (1902).
2. Paul Drude, "Zur Elektronentheorie der metalle". *Annalen der Physik* **306** (3), 566 (1900).
3. Paul Drude, "Zur Elektronentheorie der Metalle; II. Teil. Galvanomagnetische und thermomagnetische Effecte". *Annalen der Physik* **308** (11): 369 (1900).
4. J.C. Maxwell Garnett, "Colours in metal glasses and in metallic films," *Philos. Trans. R. Soc. London* **203**, 385 (1904).
5. G. Mie, "Beiträge zur Optik trüber Medien, speziell kolloidaler Metallösungen," *Ann. Phys. (Leipzig)* **25**, 377 (1908).
6. D. Pines, "Collective energy losses in solids," *Rev. Mod. Phys.* **28**, 184–198 (1956).
7. U. Fano, "Atomic Theory of electromagnetic interactions in dense materials," *Phys. Rev.* **103**, 1202 (1956).
8. R.H. Ritchie, "Plasma losses by fast electrons in thin films," *Phys. Rev.* **106**, 874 (1957).
9. R.H. Ritchie, E.T. Arakawa, J.J. Cowan, R.N. Hamm, "Surface-plasmon resonance effect in grating diffraction," *Phys. Rev. Lett.* **21**, 1530–1532 (1968).
10. A. Otto, "Excitation of nonradiative surface plasma waves in silver by the method of frustrated total reflection," *Z. Phys.* **216**, 398 (1968),
11. Kretschmann, E. and Raether, H., "Radiative decay of non-radiative surface

- plasmons excited by light," *Z. Naturf.* **23A**, 2135 (1968).
12. U. Kreibig, P. Zacharias, "Surface plasma resonances in small spherical silver and gold particles," *Z. Physik* **231**, 128 (1970).
 13. S.L. Cunningham, A.A. Maradudin, R.F. Wallis, "Effect of a charge layer on the surface-plasmonpolariton dispersion curve," *Phys. Rev. B* **10**, 3342 (1974).
 14. Fleischmann, M., P.J. Hendra, A.J. McQuillan, "Raman spectra of pyridine adsorbed at a silver electrode," *Chem. Phys. Lett.* **26**, 163 (1974).
 15. H. Raether, "Surface Plasmons (ed. Hohler, G.)" (Springer, Berlin, 1988).
 16. J. Takahara, S. Yamagishi, H. Taki, A. Morimoto, T. Kobayashi, "Guiding of a one-dimensional optical beam with nanometer diameter," *Opt. Lett.* **22**, 475–478 (1997)
 17. T.W. Ebbesen, H.J. Lezec, H.F. Ghaemi, T. Thio, P.A. Wolff, "Extraordinary optical transmission through subwavelength hole arrays," *Nature (London)* **391**, 667–669 (1998).
 18. J. Pendry, "Negative refraction makes a perfect lens," *Phys. Rev. Lett.* **85**, 396–3969 (2000).
 19. Nicholas Fang, Hyesog Lee, Cheng Sun, Xiang Zhang, "Sub-Diffraction-Limited Optical Imaging with a Silver Superlens," *Science* **308**, 534 (2005).
 20. Zhaowei Liu, Hyesog Lee, Yi Xiong, Cheng Sun and Xiang Zhang, "Far-Field Optical Hyperlens Magnifying Sub-Diffraction-Limited Objects," *Science* **315**, 1686 (2007).

21. J.B. Pendry et al. "Controlling electromagnetic fields," *Science* **312**, 1780 (2006).
22. D. Schurig et al. "Metamaterial electromagnetic cloak at microwave frequencies," *Science* **314**, 977 (2006).
23. J.B. Pendry, "Low Energy Electron Diffraction," Academic, London (1974).
24. Joannopoulos, J. D., P. R. Villeneuve, and S. H. Fan, "Photonic crystals: putting a new twist on light," *Nature* **386**, 143 (1997).
25. López, C., "Materials aspects of photonic crystals," *Adv. Mater.* **15**, 1679 (2003)
26. M. Babinet, "Memoires d'optique météorologique," *Comptes Rendus de l'Academie des Sciences* **4**, 638-648 (1837).
27. Wood, R. W., 1912, "Diffraction gratings with controlled groove form and abnormal distribution of intensity," *Philos. Mag.* **23**, 310–317.
28. Wood, R. W., 1935, "Anomalous diffraction gratings," *Phys. Rev.* **48**, 928–936.
29. Bethe, H. A., "Theory of diffraction by small holes," *Phys. Rev.* **66**, 163 (1944).
30. Ghaemi, H. F., T. Thio, D. E. Grupp, T. W. Ebbesen, and H. J. Lezec, "Surface plasmons enhance optical transmission through subwavelength holes," *Phys. Rev. B* **58**, 6779 (1998).
31. Popov, E., M. Nevière, S. Enoch, and R. Reinisch, "Theory of light transmission through subwavelength periodic hole arrays," *Phys. Rev. B* **62**, 16100 (2000).
32. Martín-Moreno, L., F. J. García-Vidal, H. J. Lezec, K. M. Pellerin, T. Thio, J. B.

-
- Pendry, and T. W. Ebbesen, "Theory of extraordinary optical transmission through subwavelength hole arrays," *Phys. Rev. Lett.* **86**, 1114 (2001).
33. Salomon, L., F. Grillot, A. V. Zayats, and F. de Fornel, "Near-field distribution of optical transmission of periodic subwavelength holes in a metal film," *Phys. Rev. Lett.* **86**, 1110 (2001).
34. Barnes, W. L., W. A. Murray, J. Dintinger, E. Devaux, and T. W. Ebbesen, "Surface plasmon polaritons and their role in the enhanced transmission of light through periodic arrays of subwavelength holes in a metal film," *Phys. Rev. Lett.* **92**, 107401 (2004).
35. Treacy, M. M. J., "Dynamical diffraction in metallic optical gratings," *Appl. Phys. Lett.* **75**, 606 (1999).
36. Treacy, M. M. J., "Dynamical diffraction explanation of the anomalous transmission of light through metallic gratings," *Phys. Rev. B* **66**, 195105 (2002).
37. Sarrazin, M., J.-P. Vigneron, and J.-M. Vigoureux, "Role of Wood anomalies in optical properties of thin metallic films with a bidimensional array of subwavelength holes," *Phys. Rev. B* **67**, 085415 (2003).
38. Lezec, H. J., and T. Thio, "Diffracted evanescent wave model for enhanced and suppressed optical transmission through subwavelength hole arrays," *Opt. Express* **12**, 3629(2004).
39. Gómez-Rivas, J., C. Schotsch, P. Haring Bolivar, and H. Kurz, "Enhanced transmission of THz radiation through subwavelength holes," *Phys. Rev. B* **68**,

- 201306_R (2003).
40. Cao, H., and A. Nahata, "Resonantly enhanced transmission of terahertz radiation through a periodic array of subwavelength apertures," *Opt. Express* **12**, 1004 (2004).
 41. Miyamaru, F., and M. Hangyo, "Finite size effect of transmission property for metal hole arrays in subterahertz region," *Appl. Phys. Lett.* **84**, 2742 (2004).
 42. J. W. Lee, M. A. Seo, D. J. Park and D. S. Kim, "Shape resonance omnidirectional terahertz filters with near-unity transmittance," *Opt. Express* **14**, 1253 (2006);
 43. Tatsunosuke Matsui, Amit Agrawal, Ajay Nahata & Z. Vally Vardeny, "Transmission resonances through aperiodic arrays of subwavelength apertures," *Nature* **446**, 517 (2007).
 44. Haitao Liu, Philippe Lalanne, "Microscopic theory of the extraordinary optical transmission," *Nature* **452**, 728 (2008).
 45. S.A. Maier, "Plasmonics: fundamentals and applications," Springer (2007).
 46. V.M. Shalaev, "Optical negative-index metamaterials," *Nat. Photonics* **1**, 41 (2007).
 47. N.H. Shen, G. Kennanakis, M. Kafesaki, N. Katsarakis, E.N. Economou, C.M. Soukoulis, "Parametric investigation and analysis of fishnet metamaterials in the microwave regime," *J. Opt. Soc. Am. B* **26**, B61-B67 (2009).
 48. M. Kafesaki, I. Tsiapa, N. Katsarakis, Th. Koschny, C.M. Soukoulis, E.N. Economou, "Left-handed metamaterials: The fishnet structure and its

-
- variations," *Phy. Rev. B* **75**, 235114 (2007).
49. Matteo Staffaroni, Josh Conway, Shantha Vedantam, Japeck Tang, Eli Yablonovitch, "Circuit Analysis in Metal-Optics," arXiv:1006.3126v5 (2010).
50. T. Li, J.Q. Li, F.M. Wang, Q.J. Wang, H. Liu, S.N. Zhu, Y.Y. Zhu, "Exploring magnetic plasmon polaritons in optical transmission through hole arrays perforated in trilayer structures," *Appl. Phys. Lett.* **90**, 251112 (2007).
51. T. Li, S.M. Wang, H. Liu, J.Q. Li, F.M. Wang, S.N. Zhu, X. Zhang, "Dispersion of magnetic plasmon polaritons in perforated trilayer metamaterials," *Appl. Phys. Lett.* **103**, 023104 (2008).

Chapter 2: Surface plasmons in infrared range

2.1 Surface waves at the metal-dielectric interface

The interaction between electromagnetic wave and metal originates from the coupling between the periodic oscillation of the electromagnetic wave and the re-distribution of the charge in metal. This kind of interaction can be firmly understood in classical framework based on Maxwell's equation. The high density of free carriers results in minute spacings of the electron energy levels compared to thermal excitation energy at room temperature. Then in metal optics, quantum mechanics is unnecessary even in nano scale. However, this would not prevent a rich physics in the field of surface plasmon.

2.1.1 Drude model and metal

When the electromagnetic wave is coupled with any materials, the dynamics can be described by macroscopic Maxwell's equation [1, 2]. Four macroscopic parameters can be connected by Maxwell's equation: charge density (ρ), current density (J), electric polarization (P) and magnetization (M). The Maxwell's equation can be written as the following form:

$$\nabla \times E = -\mu_0 \frac{\partial H}{\partial t} - \mu_0 \frac{\partial M}{\partial t}; \quad (2.1a)$$

$$\nabla \cdot E = -\frac{1}{\epsilon_0} \nabla \cdot P + \frac{1}{\epsilon_0} \rho; \quad (2.1b)$$

$$\nabla \times H = \epsilon_0 \frac{\partial E}{\partial t} + \frac{\partial P}{\partial t} + J; \quad (2.1c)$$

$$\nabla \cdot B = 0. \quad (2.1d)$$

Here E and H are the electric field and magnetic field. Due to the polarization and magnetization in the materials, the electric and magnetic field in the materials can be described by electric displacement D and magnetic induction B :

$$D = \varepsilon_0 E + P \equiv \varepsilon_0 \varepsilon E; \quad (2.2a)$$

$$B = \mu_0 (H + M) \equiv \mu_0 \mu H. \quad (2.2b)$$

Here ε and μ denote the permittivity and permeability of the materials. These two constants define the electromagnetic response of the materials to the external fields. Then Maxwell's equation can be simplified:

$$\nabla \times E = -\frac{\partial B}{\partial t}; \quad (2.3a)$$

$$\nabla \cdot D = \rho; \quad (2.3b)$$

$$\nabla \times H = \frac{\partial D}{\partial t} + J; \quad (2.3c)$$

$$\nabla \cdot B = 0. \quad (2.3d)$$

For a system with $\rho=0$ and $J=0$, the electric field and magnetic field can be extracted as the wave equations:

$$\nabla \times (\nabla \times E) = -\frac{1}{c^2} \varepsilon \mu \frac{\partial^2 E}{\partial t^2}; \quad (2.4a)$$

$$\nabla \times (\nabla \times H) = -\frac{1}{c^2} \varepsilon \mu \frac{\partial^2 H}{\partial t^2}; \quad (2.4b)$$

Here $c = (\varepsilon_0 \mu_0)^{-1/2}$ is the light speed in vacuum. Supposed the electromagnetic wave is a harmonic oscillation whose variation with time can be expressed as $\exp[i(k \cdot r - \omega t)]$, we can deduce that the wave vector should satisfy the following equation:

$$k^2 = \frac{\omega^2}{c^2} \varepsilon \mu. \quad (2.5)$$

In metal, there are lots of free electrons and these electrons' behavior when applied

external electric field reflect the electromagnetic properties of metal. Under a driven electric field, the electrons move along the reversed direction of the electric field and then form the current. Consider the metal with electron density N . The electrons can be accelerated to a speed of v under the applied electric field. Then we define the current density as:

$$J = N(-e)v. \quad (2.6)$$

Then the current is:

$$I = J \cdot A. \quad (2.7)$$

where A is the cross-sectional area (shown by Fig. 2-1(a)). In a wide frequency range, the properties of metals can be described by Drude model, which is a simple but effective model assuming the free electrons have no electromagnetic coupling with the ion cores but just follow the Newton's law of motion. When the electrons oscillate in response to the external electromagnetic field, their motion is damped for the collision with the ion cores (shown by Fig. 2-1(b)). We define the damping rate as

$$\gamma = \frac{1}{\tau}. \quad (2.8)$$

where τ is the relaxation time of the free electron gas with typical value of 10^{-14} s. The relaxation time approximately equal to the ratio of mean free path l and Fermi velocity v_F . Considering the force and momentum of each electrons, we have:

$$F(t) = -eE_{ext}; \quad (2.9a)$$

$$p(t) = mv. \quad (2.9b)$$

At the time period of t and $t+dt$, if there is no collision happens at this interval, we

have the momentum $p(t) + F(t)dt$. This event happens with the probability $1 - \frac{dt}{\tau}$. Another case, if collision happens in this interval with a probability $\frac{dt}{\tau}$, the original momentum of the electron will be set to zero in this period. Then the variation of the momentum will be $F(t)dt$. We can obtain the average momentums for all electrons:

$$p(t + dt) = (1 - \frac{dt}{\tau})(p(t) + F(t)dt) + \frac{dt}{\tau} F(t)dt. \quad (2.10)$$

Ignoring the second-order term when dt becomes very small, we obtain:

$$\frac{dp(t)}{dt} = -\frac{1}{\tau} p(t) + F(t). \quad (2.11)$$

(2.11) is the most important equation to describe Drude model.

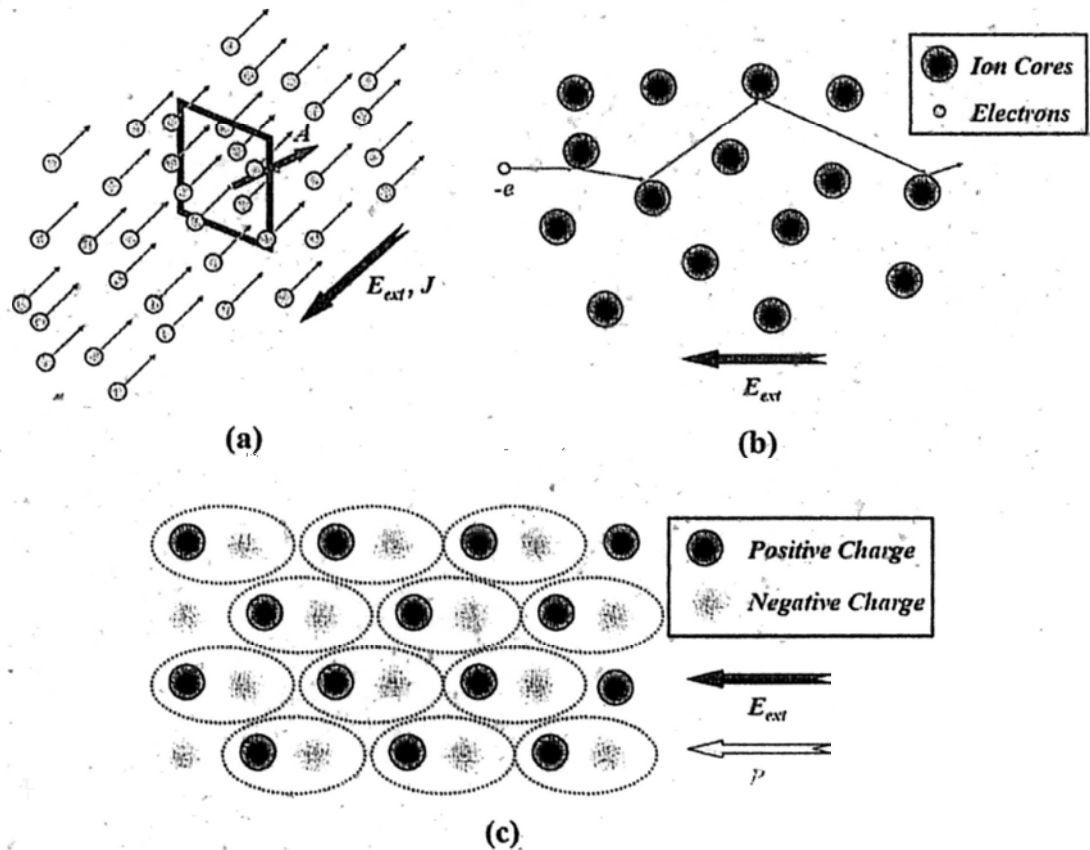


Fig. 2-1 (a) Driven by external electric field, the free electrons in metal form the current density J ; (b) The schematic of the motion for electrons in metal; (c) When

bound electrons in lattice respond to the external electric field, the temporary separation of positive and negative charges forms the polarization.

According to Equation (2.6) and (2.9b), we can modify (2.11) as:

$$\frac{dJ}{dt} + \frac{1}{\tau}J = \frac{Ne^2}{m}E_{ext}. \quad (2.12)$$

When the external field is zero, then according to equation (2.12), the transient current will have the format $J = J_0 e^{-t/\tau}$. This current will decay rapidly with time so it almost would not affect the electromagnetic properties of metal. When the electric field is a constant static field, then $dJ/dt=0$ and according to (2.12), we can obtain:

$$J = \frac{Ne^2\tau}{m}E_{ext}. \quad (2.13)$$

Since $J = \sigma_0 E_{ext}$ according to Ohm's law, then:

$$\sigma_0 = \frac{Ne^2\tau}{m} \quad (2.14)$$

Here σ_0 is static conductivity of metal. For another case when $E_{ext} = E(r)e^{-i\omega t}$, according to equation (2.12), we have:

$$J = \frac{\sigma_0}{1 - i\omega\tau} E_{ext} \equiv \sigma(\omega)E_{ext}. \quad (2.15)$$

where

$$\sigma(\omega) = \frac{\sigma_0}{1 - i\omega\tau}. \quad (2.16)$$

Equation (2.16) means that the conductivity of metal is a frequency-dependent parameter.

Besides free electrons, there are large amount of bound electrons in metal. Their response to the electromagnetic wave is similar to dielectric. The separation of

positive and negative charges in lattice will result in polarization in the materials which is shown by Fig. 2-1(c). Supposed the deviation of negative charge from the center of positive charges is r , the polarization can be expressed as: $P=N_b(-e)r$. Here N_b means the bound electron density. Then we have:

$$\frac{dP}{dt} = N_b(-e) \frac{dr}{dt} = N_b(-e)v_b = J_b. \quad (2.17)$$

In this equation, v_b means velocity of the electrons when oscillating. In another opinion of view, if we treat the current density induced by the free electrons as a time-varied polarization, according to equation (2.15), we can obtain:

$$J = \frac{\sigma(\omega)}{-i\omega} \frac{\partial E_{ext}}{\partial t} = \frac{\partial}{\partial t} \left[\frac{i\sigma(\omega)}{\omega} E_{ext} \right]. \quad (2.18)$$

Combining equation (2.16), (2.17) and (2.18), the polarization due to the free electron can be expressed as:

$$P = \frac{i\sigma(\omega)}{\omega} E_{ext} = -\frac{Ne^2}{m} \frac{1}{(\omega^2 + i\omega\gamma)} E_{ext} \quad (2.19)$$

Here γ in the equation is the damping rate (or collision frequency) of the electrons.

According to equation (2.2a), we have the permittivity of metals:

$$\varepsilon(\omega) = 1 + \frac{i\sigma(\omega)}{\varepsilon_0\omega} = 1 - \frac{\omega_p^2}{\omega^2 + i\omega\gamma}. \quad (2.20)$$

Here $\omega_p \equiv (Ne^2 / m\varepsilon_0)^{1/2}$ is the defined as plasma frequency of metal. Equation (2.20) is a very important conclusion of Drude model. In this equation, the real and imaginary parts can be respectively expressed as:

$$\operatorname{Re}[\varepsilon(\omega)] = 1 - \frac{\omega_p^2}{\omega^2 + \gamma^2}. \quad (2.21a)$$

$$\operatorname{Im}[\varepsilon(\omega)] = \frac{\omega_p^2 \gamma}{\omega(\omega^2 + \gamma^2)}. \quad (2.21b)$$

When the frequency is much larger than the damping rate, $\varepsilon(\omega)$ is dominated by the real part. Then equation (2.20) can be simplified to:

$$\varepsilon(\omega) = 1 - \frac{\omega_p^2}{\omega^2}. \quad (2.22)$$

For general metals such as gold (Au), silver (Ag), copper (Cu), aluminum (Al) et al., plasma frequency ω_p is usually at ultraviolet range.

In the free electron model, $\varepsilon(\omega) \rightarrow 1$ when $\omega \gg \omega_p$. For some noble metals such as gold, silver and copper, an extension to this model is needed in the region of $\omega > \omega_p$ due to the interband transitions. This effect therefore modifies equation (2.20) to be:

$$\varepsilon(\omega) = \varepsilon_\infty - \frac{\omega_p^2}{\omega^2 + i\omega\gamma}. \quad (2.23)$$

The validity of the equation (2.23) is illustrated by Fig. 2-2 [2]. The experimental data of gold is extracted from Ref. [3] and fitted to the equation. It shows that at visible and ultraviolet (UV) range, the applicability of this model breaks down due to the occurrence of interband transitions. For our discussion frequencies from near infrared to far infrared, Drude model can describe the properties of metal pretty good.

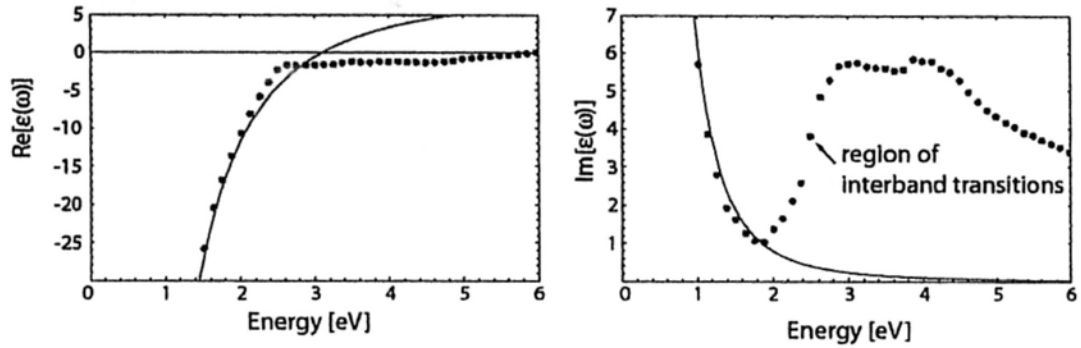


Fig. 2-2 The validity limits of Drude model.

The parameters of Drude model for several noble metals described by equation (2.23) are shown by Table 2-1 [4, 5]. All these four metals satisfy the requirement for plasmonic applications.

Table 2-1 Drude model parameters for metals

	ϵ_{∞}	ω_p (eV)	γ (eV)
Silver	3.7	9.2	0.02
Gold	6.9	8.9	0.07
Copper	6.7	8.7	0.07
Aluminum	0.7	12.7	0.13

The real part and imaginary part of Al, Ag, Au and Cu are plotted in Fig. 2-3. In high frequencies, both the real and imaginary parts of permittivity vary quickly when the frequencies change. In low frequency range, the metals tend to be perfect electric conductor (PEC). Fig. 2-3 (b) and (c) show the zoom view of the curve in low frequencies. In general, the intrinsic plasma frequency of a metal is in the ultraviolet or visible range. The electromagnetic wave becomes highly localized at the metal-dielectric interface when its frequency approaches the plasma frequency.

We will show that according to the dispersion relationship, the confinement breaks down when the propagation constant of the surface wave is reduced at lower frequencies, such as in the terahertz range, where the permittivity of metals described by the Drude Model is much larger than that in the UV and visible range. Hence the terahertz wave will decay very fast in the metal.

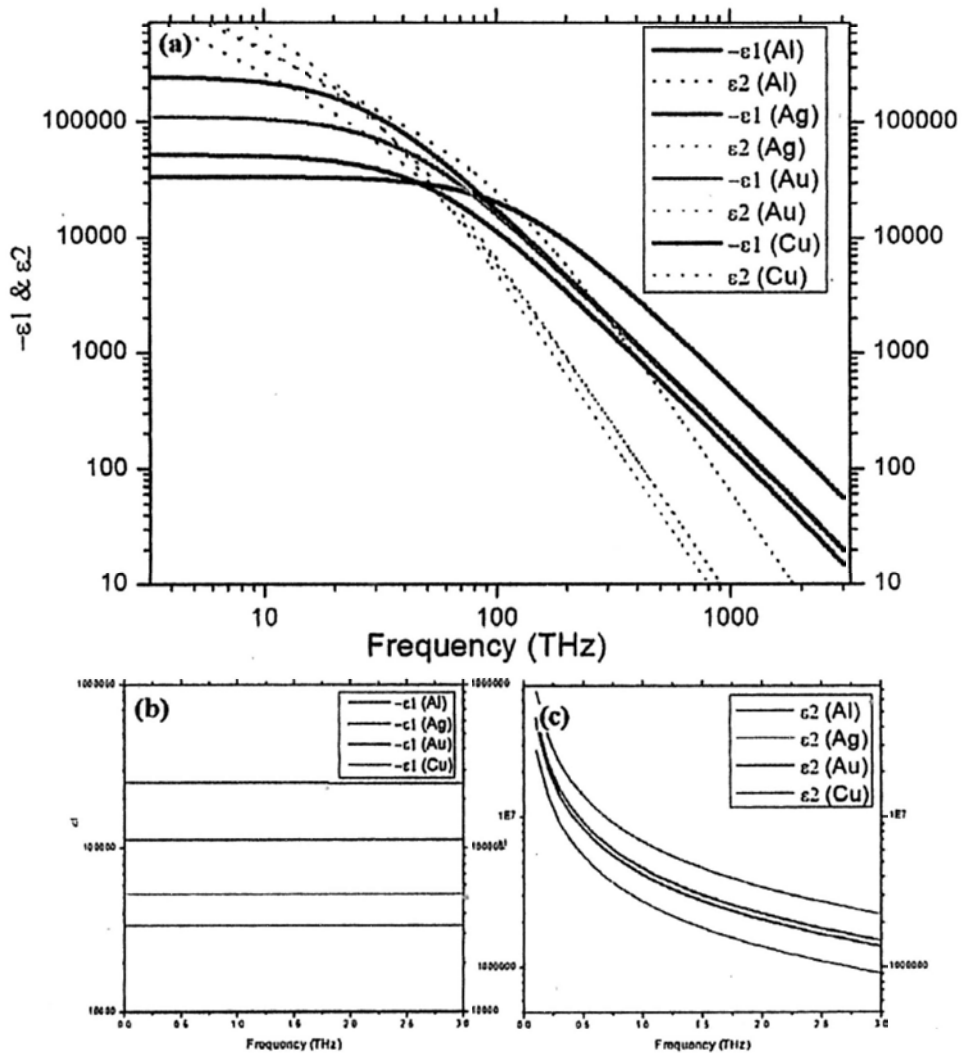


Fig. 2-3 (a) The real and imaginary parts of Al, Ag, Au and Cu in wide frequency range; Zoom view of the curve in low frequency range of the real part (b) and imaginary part (c).

In summary, the properties of metal play a very important role in the discussion of surface plasmon. We mathematically show that the negative sign of permittivity is a necessary condition supporting the excitation and propagation of surface plasmon in next part. The dispersion of permittivity directly defines the dispersion of the surface wave.

2.1.2 Propagation of surface plasmons on metal surface

In the last century, the interaction between the electromagnetic radiation and materials interface has become a popular research area due to the interesting physical phenomenon. And the development of nano fabrication technique provides a possibility to experimentally demonstrate some ideas. Surface plasmon is among this kind of subjects. The theoretical basis has been solved with some very simple mathematics but the physics is fascinating. In this part, we will introduce some basic calculations which is related to the basic properties of surface plasmon, especially for the dispersion of surface wave.

In bulk metal, the oscillation of free electrons is called “volume plasma oscillation”. Its resonant frequency is metal’s intrinsic plasma frequency ω_p . At the metal-dielectric interface, the dynamics is different. When considering an incident electromagnetic wave with transverse magnetic (TM) mode, there is an electric component in z -direction, which is a discontinuous component. This discontinuity results in different electric field intensity between inside metal and outside dielectric, which is shown by Fig. 2-4. Then free electrons will form a periodic distribution of the charge density at surface σ_{surf} , which is proportional

to $\epsilon_0(\epsilon_1 E_{1z} - \epsilon_2 E_{2z})$. The distribution σ_{surf} is a function of the k -vector of the surface wave which can be written as:

$$\sigma_{surf} = \sigma_{surf0} e^{i(k_x x - \omega t)}. \quad (2.24)$$

But for transverse electric (TE) wave, the electric field is paralleled to the interface and there is no electric component in z -direction. In this direction, the electric displacement is continuous. Then there will be no polarized charge accumulated at the interface.

Then we consider the mathematical model for the metal-dielectric interface. All the deduction comes from Maxwell's equation based on classical electromagnetics. We use the same coordinate system shown in Fig. 2-4 with y -axis perpendicular to the x - z plane.

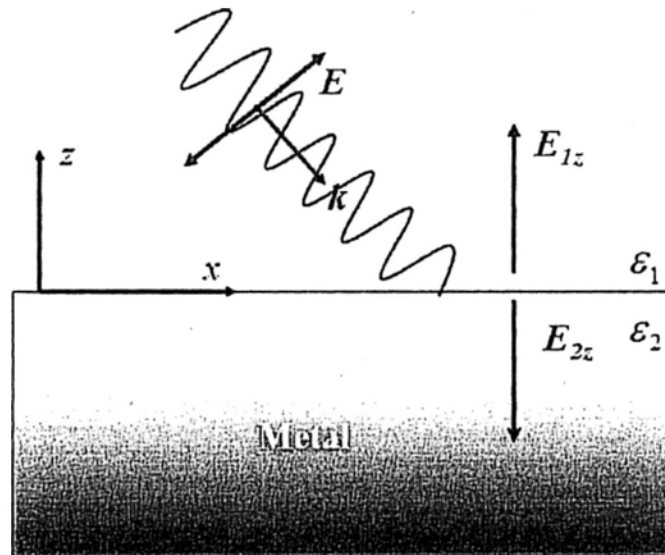


Fig. 2-4 The discontinuity of E_z at the interface between metal and dielectric.

According to equation (2.3a) and (2.3c), we can obtain the following equation in the absence of external charge and current density:

$$\nabla \times \nabla \times E = -\mu_0 \frac{\partial^2 D}{\partial t^2} \quad (2.25)$$

Simplified this equation, equation (2.25) yields the Helmholtz equation:

$$\nabla^2 E + k_0^2 \varepsilon E = 0 \quad (2.26)$$

Applied to the surface problem by assuming the electric field can be described as $E(x, y, z) = E(z)e^{ik_x x}$, we can obtain:

$$\frac{\partial^2 E(z)}{\partial z^2} + (k_0^2 \varepsilon - k_x^2)E(z) = 0 \quad (2.27)$$

A similar equation can be obtained for magnetic field.

Now let's look at the simplest case shown by Fig. 2-4. By solving equation (2.27), we can obtain the solution for TM mode incidence in $z > 0$ regions:

$$H^{(1)} = (0, H_{1y}, 0)e^{ik_{1z}z} e^{i(k_x x - \omega t)} \quad (2.28a)$$

$$E^{(1)} = (E_{1x}, 0, E_{1z})e^{ik_{1z}z} e^{i(k_x x - \omega t)} \quad (2.28b)$$

For $z < 0$ regions, we have:

$$H^{(2)} = (0, H_{2y}, 0)e^{-ik_{2z}z} e^{i(k_x x - \omega t)} \quad (2.29a)$$

$$E^{(2)} = (E_{2x}, 0, E_{2z})e^{-ik_{2z}z} e^{i(k_x x - \omega t)} \quad (2.29b)$$

The evanescent decay length in metal and dielectric is defined as the reciprocal of k -vector in z -direction:

$$\hat{z} = \frac{1}{|k_{iz}|} \quad (i = 1, 2) \quad (2.30)$$

The decay length quantifies the confinement of the surface wave.

Continuity of magnetic field in y -direction and electric displacement in z -direction leads to a relationship:

$$\frac{k_{1z}}{\varepsilon_1} + \frac{k_{2z}}{\varepsilon_2} = 0 \quad (2.31)$$

With our convention of the signs in the exponents in equation (2.28) and (2.29), the real part of permittivity of two materials must be opposite sign. That means the surface wave only exist at the interface with opposite sign of permittivity, such as metal and insulator.

Go back to the wave equation for the magnetic field, we have:

$$k_{iz}^2 = \varepsilon_i \left(\frac{\omega}{c}\right)^2 - k_x^2 \quad (i=1, 2) \quad (2.32)$$

Combining (2.31) and (2.32), we can obtain:

$$k_x = \frac{\omega}{c} \sqrt{\frac{\varepsilon_1 \varepsilon_2}{\varepsilon_1 + \varepsilon_2}} \quad (2.33)$$

This equation combined with equation (2.20) or (2.22) or (2.23) leads to the dispersion configuration of the surface plasmon at single metal-dielectric interface which is shown by Fig. 2-5.

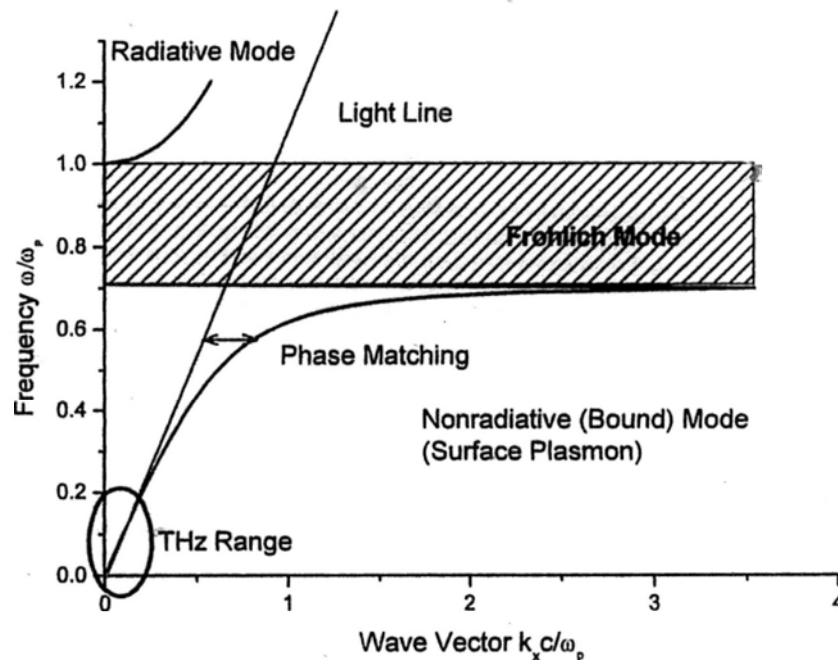


Fig. 2-5 Dispersion configuration of SPs at single metal-dielectric interface.

Fig. 2-5 shows rich physics about surface plasmon at single metal-dielectric interface. Between the surface plasmon (bound mode) and radiative mode, there is a forbidden band which is called Frohlich mode, which is fully discussed in other area especially for localized surface plasmons in nano particles. In this region, the propagating surface plasmon is very lossy. For the surface plasmon, when the wave vector goes to larger, the group velocity of the surface wave goes to zero and the dispersion curve is a asymptote to a certain frequency. We define this frequency as characteristic surface plasmon frequency:

$$\omega_{sp} = \frac{\omega_p}{\sqrt{1 + \epsilon_1}} \quad (2.34)$$

where ϵ_1 is the permittivity of the dielectric.

At low frequencies, the dispersion curve is very close to the light line. According to equation (2.30) and (2.31), the decay length in the metal is very small compared with that in the dielectric. That means the confinement breaks down when the surface plasmon goes to low frequency such as THz frequencies. This point has been experimentally verified by measuring the field distribution in metal wire waveguide in THz range [6]. Then the introduction of roughness on a smooth metal surface provides a way to modify the low-frequency wave behavior at the metal-dielectric interface [7]. This idea has led to the research on the designs of structures which produce “spoof plasmons” [8-10].

2.2 Spoof surface plasmon

Before we discuss spoof surface plasmon, one issue should be highlighted here

to make our discussion clear. Until now, many papers have been published for the surface plasmon in structured surfaces. Among all these investigations, the structure dimension compared to the concerned wavelength should be paid attention to since it directly affect the electromagnetic mechanisms for the structures. A very simple example is the 1D grating. Subwavelength gratings are usually used for excitation of surface waves. But when discussing spoof surface plasmon, grating or groove structures are also commonly used. The physics and mathematics for these two discussions are different. The subwavelength gratings for surface plasmon excitation will follow the momentum conservation:

$$k_x = k_0 \pm mG_x \pm nG_y = \frac{\omega}{c} \sqrt{\frac{\epsilon_1 \epsilon_2}{\epsilon_1 + \epsilon_2}} \quad (2.35)$$

where G_x and G_y are the reciprocal lattice vectors, m and n are integers of SP modes. But for the spoof surface plasmon we are now discussing in this part, the patterned surface is described in long wavelength limit (dimension of the structure is much smaller than wavelength) as effective medium.

We have seen that due to the large permittivity of metals at low frequencies, surface plasmons in this regime are highly delocalized. In the limit of PEC, the field penetrating into the metal is identically zero. Perfect metals thus do not support surface modes. Pendry and his colleagues show that the corrugated surfaces can mimic the SPP by the bound electromagnetic wave [8, 11]. We take the one-dimensional array of grooves as an example for our discussion.

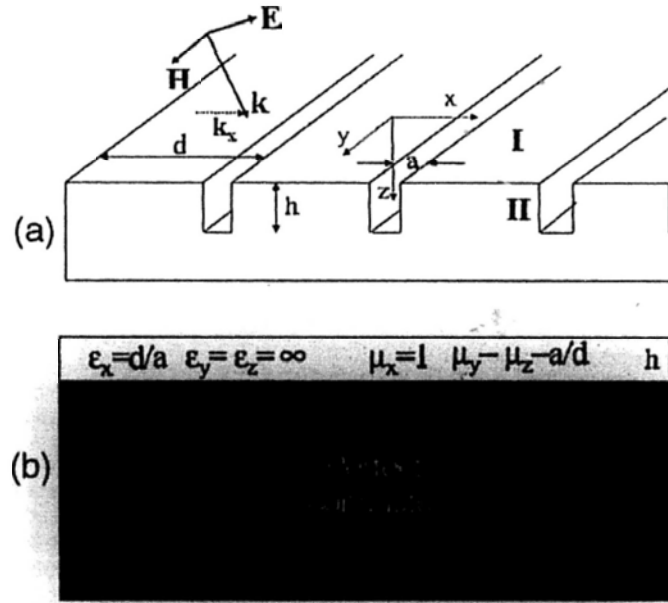


Fig. 2-6 (a) 1-D array of grooves; (b) Effective medium approximation.

If the size and spacing of the textured surface is much smaller than the wavelength, it can be described effective medium dielectric function of the plasma form with plasma frequency determined by the geometry of the structure. This kind of materials with subwavelength structure exhibiting such an effective photonic response is called “metamaterials”. Metamaterial is another popular research area. Here we just take concept “effective medium” for our discussion. Fig. 2-6 (a) shows the geometry of the structure [12]. The array of grooves has the width a and depth h . The lattice constant is d and the material of the structure is supposed to be PEC. The dispersion relation $\omega(k_x)$ of the surface waves propagating along the grooves can be calculated by launching a TM-polarized incident wave and examining the reflectance. Here k_x is the propagating constant of the surface wave. As shown in Fig. 2-6(b), we define the structure’s permittivity as

$$\varepsilon_x = d/a, \varepsilon_y = \varepsilon_z = \infty; \quad (2.36a)$$

$$\mu_x = 1, \mu_y = \mu_z = a/d. \quad (2.36b)$$

The dispersion relation of the surface mode of this anisotropic structure can be expressed as:

$$\frac{\sqrt{k_x^2 - k_0^2}}{k_0} = \frac{a}{d} \tan k_0 h. \quad (2.37)$$

Fig. 2-7 shows the plot of the dispersion relation for $a/d=0.2$ and $h=d$. The dispersion curve is very similar to that in real metal. Here the plasma frequency or characteristic surface plasmon frequency is determined by the geometry:

$$\omega_{sp} \propto \frac{\pi c}{2h}. \quad (2.38)$$

This equation reflects the physical interpretation of the surface mode in PEC grooves. This frequency corresponds to the fundamental cavity waveguide mode inside the groove in the limit $a/d \rightarrow 0$. These resonances arise due to the interference between modes propagating in the forward and backward z -direction. The surface mode is then established due to coupling between cavity modes localized in individual grooves [2].

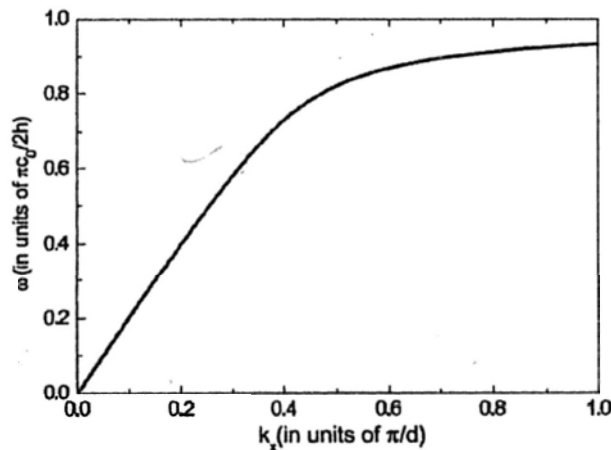


Fig. 2-7 Dispersion relation of the spoof SPs in a groove array.

A direct measurement of the confinement in structured surfaces for THz spoof surface plasmon is described by Ref. [9]. In this measurement, THz time-domain spectroscopy (THz_TDS) system is applied to make it. THz_TDS is a powerful tool to study the materials' electromagnetic dynamics.

2.3 Introduction to THz wave and THz_TDS

2.3.1 THz wave and THz_TDS system

In physics, terahertz radiation refers to electromagnetic waves propagating at frequencies in the terahertz range. Terahertz time-domain spectroscopy (THz_TDS) is a very important and successful research field of THz waves. In physics, THz-TDS is a spectroscopic technique in which the properties of a material are probed with short pulses of terahertz radiation [13, 14]. The generation and detection scheme is sensitive to the sample material's effect on both the amplitude and the phase of the terahertz radiation. In this respect, the technique can provide more information than conventional Fourier-transform spectroscopy, which is only sensitive to the amplitude.

THz radiation has several distinct advantages over other forms of spectroscopy: many materials are transparent to THz, THz radiation is safe for biological tissues because it is non-ionizing (unlike for example X-rays), and images formed with terahertz radiation can have relatively good resolution (less than 1 mm). Also, many interesting materials have unique spectral fingerprints in the terahertz range, which means that terahertz radiation can be used to identify them.

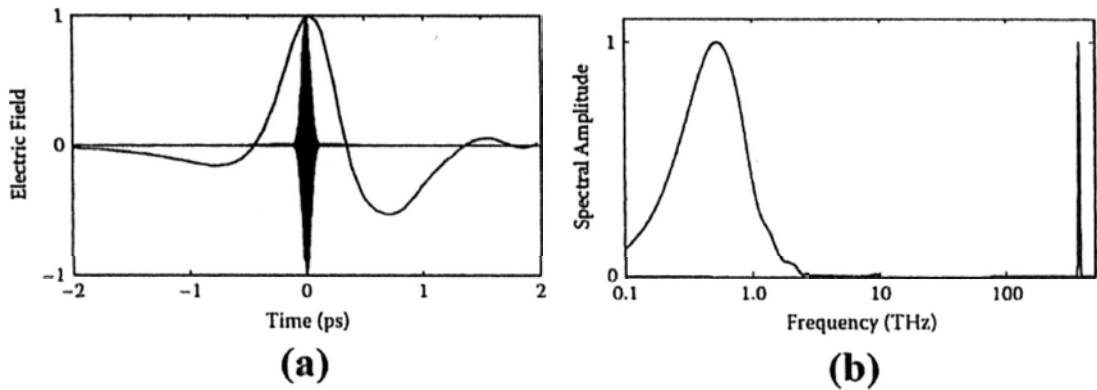


Fig. 2-8 Electric field of a measured THz pulse and the simulated field of the exciting optical pulse are shown in (a), whereas the amplitude spectrum is shown in (b).

The most significant difference between THz pulses and visible, infrared, or ultraviolet light more familiar to most researchers is THz spectroscopy directly measures the electric field of the pulse rather than the intensity. The direct measurement of field is possible simply because of the much slower variation of the field as can be seen in Fig. 2-8. This figure shows the typical electric field of a measured THz pulse and the simulated field of exciting optical pulse in time domain (Fig. 2-8 (a)) and frequency domain (Fig. 2-8 (b)).

Two types of THz_TDS base on two types of generation and detection schemes. The first one is based on the nonlinear crystal such as Zinc Telluride (ZnTe) crystal. The principle of the process is optical rectification (generation) and electro-optical sampling (detection). A typical characteristic of this kind of system is that it works at about 2THz (300 μ m) demonstrated by a simple optical setup. Another type of the THz_TDS is based on photoconductive antennas, on which we will have detailed

discussion in the following chapters.

Until now, THz_TDS has got applications in the field of real time THz imaging, studies of carrier dynamics in semiconductor and conductivity processes in novel electronic materials, optical response of semiconductor nanostructures, biomolecules, Pharmaceutical and Security et al.

A THz_TDS system is a time-resolved spectroscopy system with active THz components. The generation and detection components are photoconductive antennas. In principle, the technique can be extended to any process that leads to a change in properties of a material, which leads to the optical-pump-and-probe technique. With the help of pulsed lasers, it is possible to study processes that occur on very short time scales.

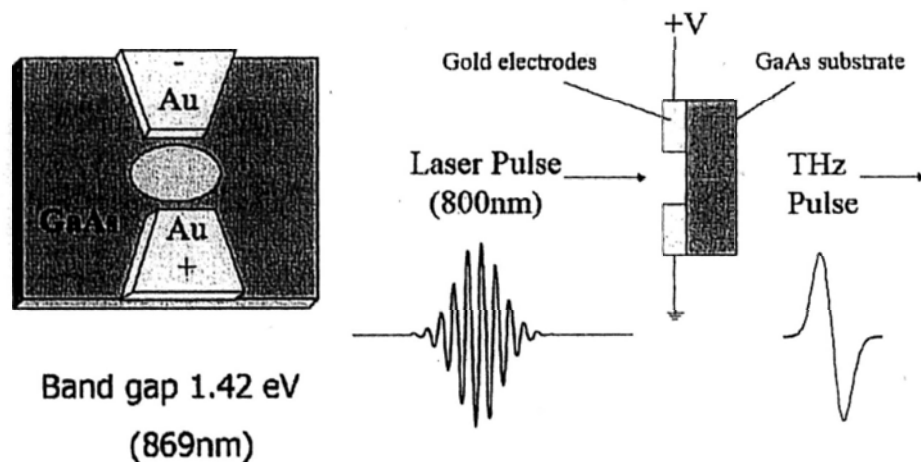


Fig. 2-9 Schematic of bowtie photoconductive antenna (left-hand side) and THz wave generation pumped by a femtosecond laser pulse with 800nm wavelength (right-hand side).

Fig. 2-9 shows the schematic for the bowtie photoconductive antennas as a THz

emitter. When a femtosecond laser pulse is incident on the GaAs semiconductor with bowtie metal patterns, carriers in high-mobility compounds accelerate rapidly, leading to fast rise times. The DC-biased antenna produces the electric field. This capacitive structure stores energy with a capacitance in the order of pF. The bandgap of GaAs is about 1.42 eV and an excitation source with higher energy is necessary for THz generation. Usually, we use the Ti Sapphire fs laser with 800nm wavelength as the excitation source. The electron-hole pairs are formed in the GaAs and driven by the electric field. The time dependence of the carrier dynamics in the GaAs has been written explicitly to illustrate the transient nature of the photoconductivity on subpicosecond time scales. It is the transient current that generates the THz pulse. When the current goes through the simple coplanar stripline structure such as bowtie, spiral, dipole et al., an impulse excitation to the antenna is produced and the radiation pattern and THz pulse are determined both by the response of the semiconductor as well as the antenna.

For the THz detection scheme, we also use a photoconductive antenna as detector. To measure the electric field with high temporal resolution, the semiconductor should have similar response time compared with the picosecond THz pulse. To suppress the additional resistance in semiconductor and to get stronger localized electric field between the antenna gaps, we usually use small-gap (around $5\mu\text{m}\sim 30\mu\text{m}$) antenna as detector. The electric field is provided by the incident ps THz wave and the carrier is excited by the synchronized fs pulse. The fs laser pulse will sample the ps THz pulse controlled by the optical delay line in the

detector.

With feasible THz emitter and detector, we have to couple these two components together in the system. Usually we use silicon ball lens to collimate the THz wave. The silicon ball lens mainly have two functions in the system: 1. collimate or focus THz wave; 2. the interface between the GaAs wafer and air will become GaAs-Silicon interface which will suppress the reflection of THz wave at the interface.

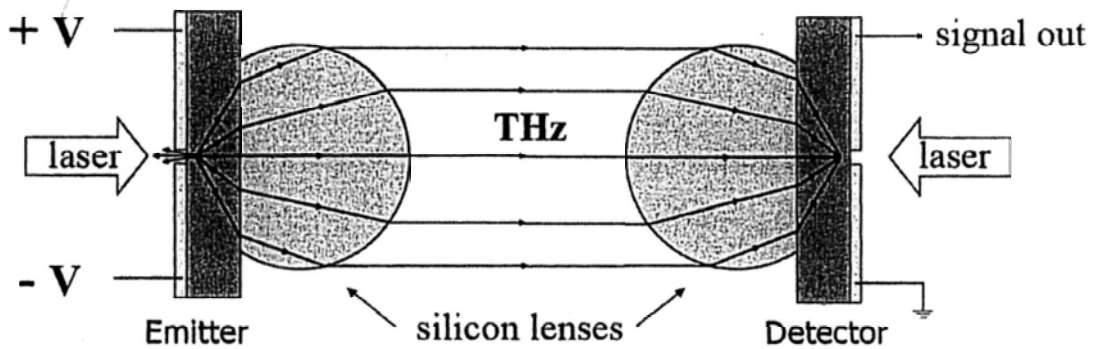


Fig. 2-10 Schematic of the coupling between THz emitter and detector.

Fig. 2-10 shows the schematic of the coupling between the THz emitter and detector in free space. In THz_TDS system, the beam path of pumping laser plus THz wave is equal the beam path of probing laser in length, one of which is tunable to scan the THz pulse in time domain. The sampling process of THz pulse is described by Fig. 2-11. By tuning the spatial difference of the pumping and probing beam path, the amplitude and phase of the THz electric field can be measured. After the Fourier transform, the spectrum information can be retrieved.

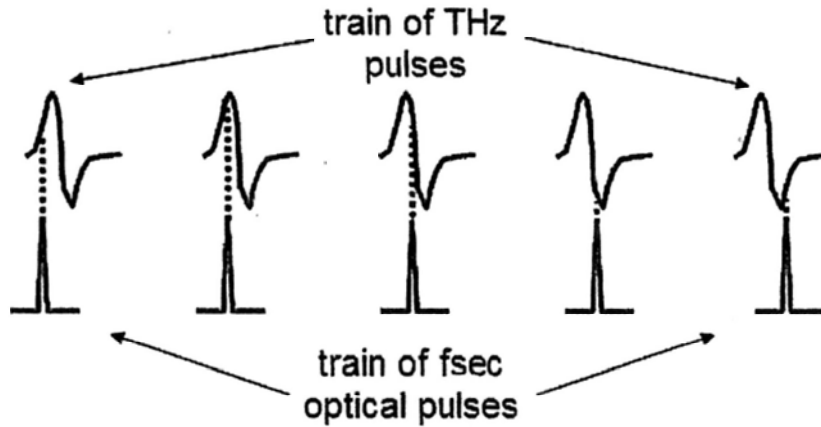


Fig. 2-11 The sampling process of THz pulse by using femtosecond optical pulse.

The schematic of our THz_TDS system is shown by Fig. 2-12. The laser is a mode-locked Ti: Sapphire femtosecond with 800nm wavelength, 30~50fs pulse width and ~82MHz repetition rate. Some parameters of the laser will be shown below. The laser beam goes through a beam splitter (BS) and was split into pumping beam and probing beam. M1~M5 are mirrors with HR coating for the light wave with 800nm wavelength. L1 and L2 are the objective lens focusing the optical beam on the photoconductive antennas. Antenna1 and Antenna2 are emitter and detector for THz wave with silicon ball lens. Four parabolic golden mirrors (P1~P4) are used in this system to form the 8-F confocal setup for THz wave. The samples to be measured are placed at the middle of the THz beam path. The beam waist of THz wave at the focusing point is about 4~5mm, which is simply measured by knife-edge method. A very important component in this system is the optical delay, which consist of a Newport miniature linear stage and a Newport broadband hollow retroreflector.

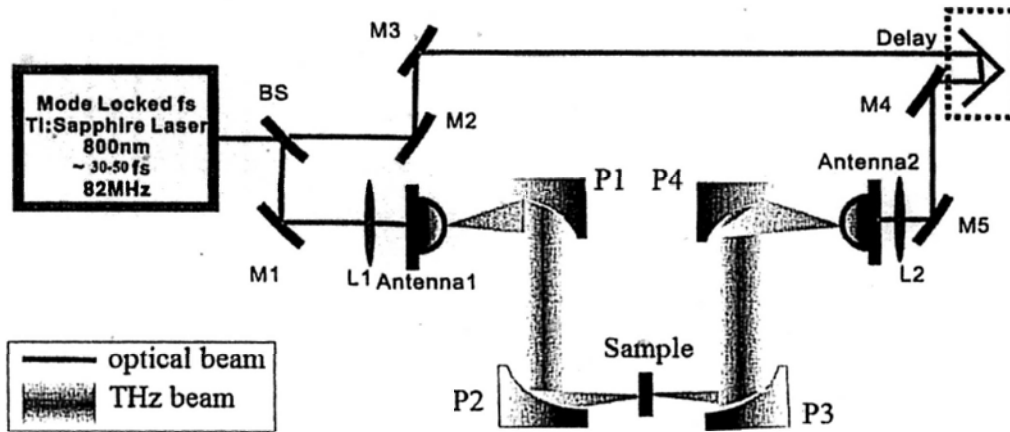


Fig. 2-12 Schematic of THz_TDS setup.

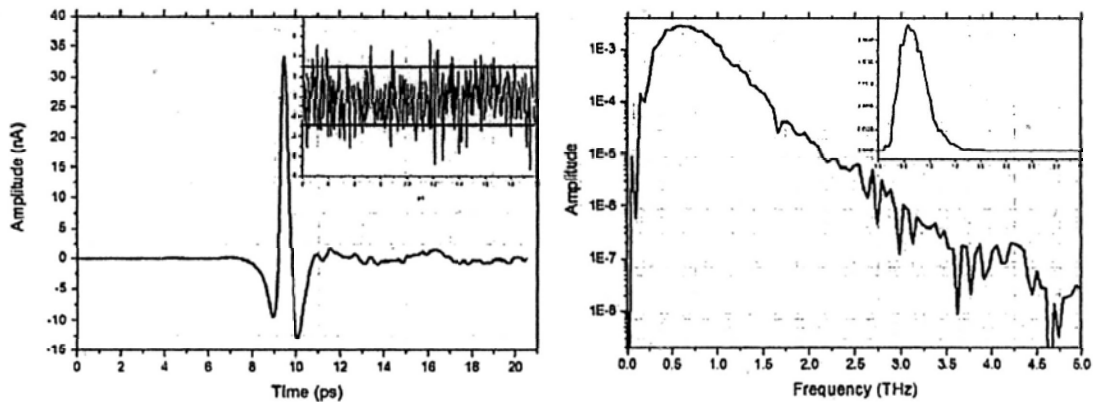


Fig. 2-13 Typical output of THz_TDS setup.

A typical output of the system is shown by Fig. 2-13. The figure on the left-hand side shows the time-domain THz pulse. The inset figure shows the noise level with optical pumping but no THz is generated by photoconductive antenna. The noise level is at about $-3 \sim +3$ pA and the signal magnitude is about 33 nA. The figure on the right-hand side shows the spectrum in frequency domain under single measurement in log scale. The inset figure shows the spectrum in linear scale.

2.3.2 Applications of THz-TDS on spoof surface plasmon

As we mentioned before, THz-TDS is a powerful tool to study the

electromagnetic dynamics of the materials of devices. A typical application on spoof surface plasmon is the transmission study for planar 2D plasmonic structures. We take a popular metamaterials design, fishnet structure, as an example to give a brief introduction to the THz-TDS's transmission measurement.

Recently metamaterials have attracted much attention as artificially engineered materials with subwavelength structures. They exhibit fascinating properties, such as negative refraction [15], can effectively alter the propagation of the electromagnetic wave in a pre-designed manner [16] and make applications such as superlens possible [17]. In particular, metamaterials with fishnet structures aroused much interest because of their easy fabrication and convenient designs to achieve optimized properties.

The design of fishnet structures has been primarily focused in both microwave and optical regimes. Furthermore, the inductor-capacitor (LC) circuit model which was proposed earlier [18, 19] in the microwave regime has been successfully verified. This study focuses on the isotropic fishnet structure, which is polarization-independent by its isotropic nature, in the terahertz range. Samples with a dual-layer structure were fabricated and measured in a terahertz time-domain spectroscopy (THz-TDS) system to characterize their transmittance. Simulations were also conducted to determine the variation of the resonant frequencies of such structures under different geometrical dimensions.

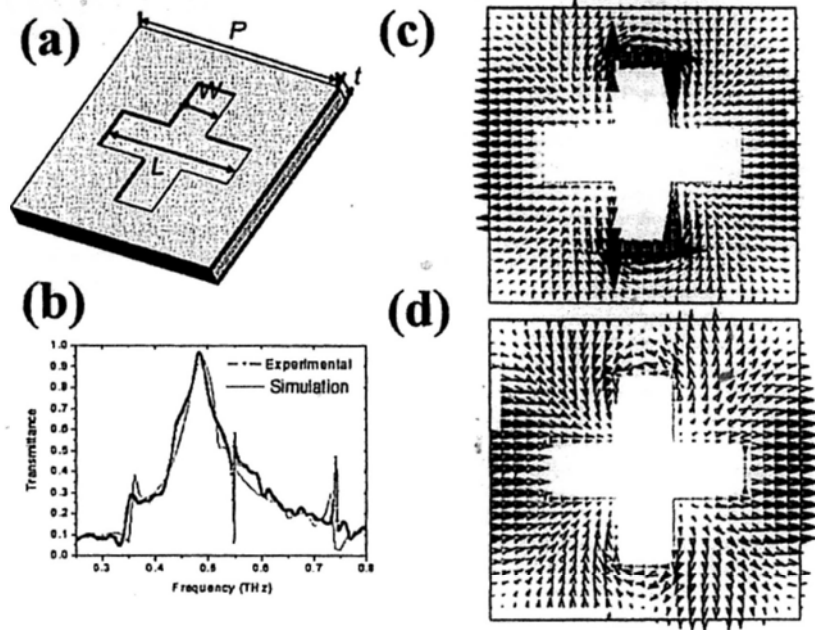


Fig. 2-14. (a) Schematic of the structure; (b) Experimental result from THz-TDS and the simulation result; (c) and (d) the surface current distributions of the two metal layers at 0.36THz.

Magnetization waves have been observed in negative-index metamaterials with fishnet structure [20] in the optical range. Hence the structure is expected to exhibit both magnetic resonance (antisymmetric mode) and electric resonance (symmetric mode) in the terahertz range as well. Fig. 2-14(a) shows a schematic of the fabricated device. The structure can be described by P (period), L (cross member length), W (cross member width) and t (spacing between the two layers). The dielectric layer sandwiched between the metal layers is polyimide. The transmittance of the device measured by THz-TDS is shown in Fig. 2-14(b). The sharp peaks at 0.55THz and 0.74THz are caused by water vapor absorption. Simulation was performed using HFSS (High Frequency Structure Simulator). It is observed that there is a good match between the simulation and experimental results.

At around 0.35 THz, a peak is clearly seen in both curves. According to the theory on fishnet structure, this peak and the main peak correspond to the magnetic resonance and electric resonance respectively. To verify this point, we plot the simulated surface current distributions on the two metal layers in Fig. 2-14(c) and (d) corresponding to the peak at 0.36THz. The result verifies the antisymmetric mode pattern which should correspond to a magnetic resonance. A symmetric mode pattern was observed for the main peak at 0.49THz but is not shown here.

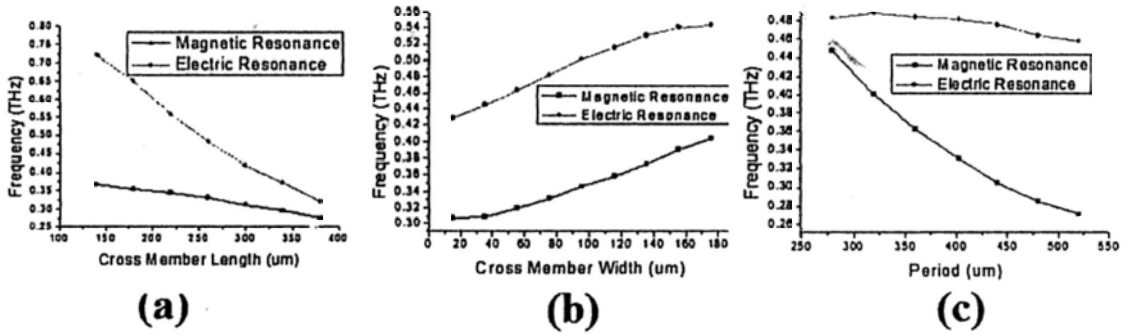


Fig. 2-15 Magnetic and electric resonant frequencies versus (a) L at $W=76\mu\text{m}$, $P=402\mu\text{m}$; (b) W at $L=260\mu\text{m}$, $P=402\mu\text{m}$; and (c) P at $L=260\mu\text{m}$, $W=76\mu\text{m}$.

In Refs. [18] and [19], the relation between the geometrical dimensions of the structure and the resonant frequencies is presented in the microwave regime. In this study, their circuit model is adapted here to derive the relationship between the magnetic resonant frequency and the geometrical parameters in the following equation:

$$\omega_m \sim \frac{1}{P-W} \sqrt{\frac{P-L}{W}} + C \quad (2.39)$$

where C is a constant. Fig. 2-15 shows the simulated magnetic and electric resonant frequencies versus the geometrical parameters L , W and P at a constant spacing

layer $t=25\mu\text{m}$, respectively. The change of the magnetic resonant frequency shown in the figure can be qualitatively explained by equation (2.39). Hence equations deduced from the circuit *LC*-model can provide a simple guidance to help design the resonant modes in the structure. An example would be to widen the separation between the magnetic and the electric resonant modes so as to obtain an optimized polarization-independent left-handed band in the isotropic fishnet structure. Our investigation thus provides a useful background for further theoretical and experimental studies of fishnet devices in the terahertz regime, particularly for understanding left-handed resonant modes.

Besides negative refraction, the fishnet structure also finds application in magnetic plasmon polariton (MPP) nanolaser, waveguides, selective switches and etc. The basic fishnet structure is the metal-insulator-metal (MIM) structure which can be magnetically excited and described by the *LC*-resonance model. The dispersions of the magnetic and electric resonant modes are closely related to the mechanism of the coupling between the two metallic layers. The multiple MPP modes in the optical regime have been analyzed in the last three years [21, 22] and the results show abundant physics in the two-layer coupled system.

Our investigation described in below tries to understand the behavior of the transmission spectra of the dual-layer fishnet structure by changing the incident angle of the THz wave and the thickness of the dielectric layer separating the two metallic films. The dispersion of the 3 major modes measured in this structure can be inferred from such behavior qualitatively. Simulation studies will be carried

out to analyze and confirm the nature of these modes.

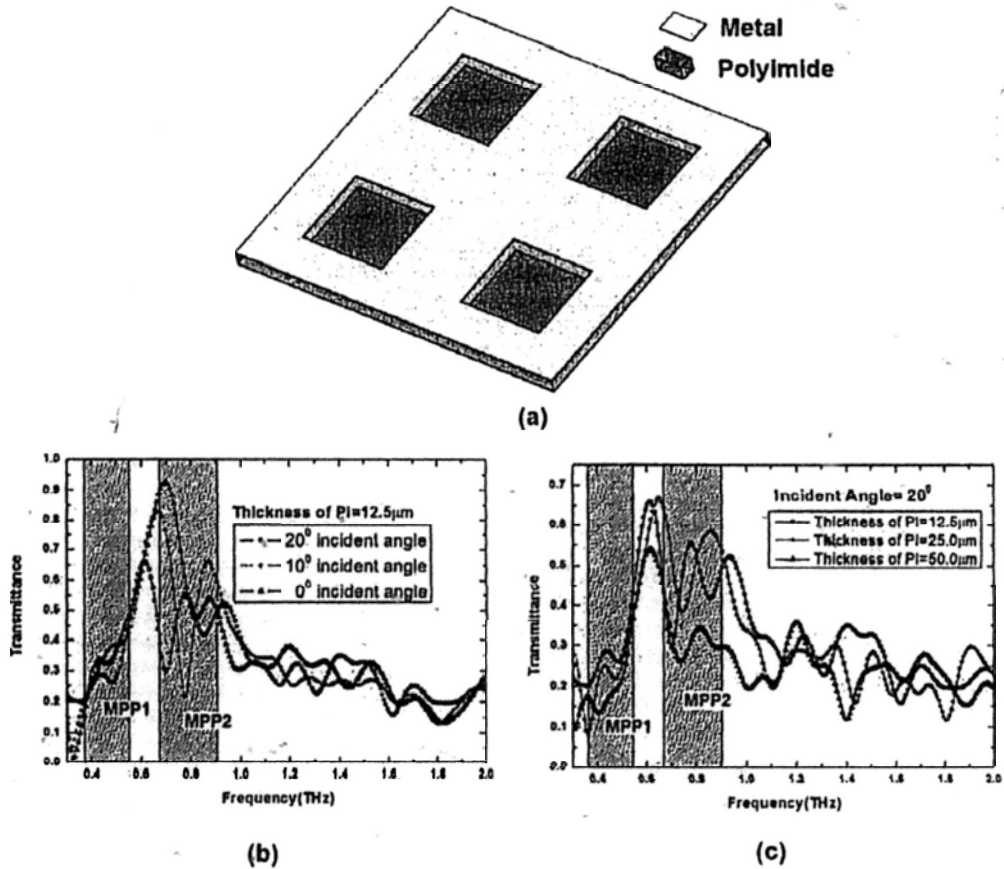


Fig. 2-16 (a) The schematic of the fishnet structure. (b) The measured transmittance of the sample with thickness of PI = 12.5 μm under different incident angles. (c) The measured transmittance of the samples with different thickness of PI under the 20° incident angle. The dips in the grey regions are the two MPP modes and the main peak corresponds to the electric resonant mode

We conducted a detailed study on both the electric and magnetic resonances of the MIM fishnet structure at THz frequencies. A flexible dual-layer symmetric fishnet structure on the two sides of a polyimide (PI) dielectric thin film with different thicknesses was fabricated by conventional photolithography. The structure is shown in Fig. 2-16(a). The parameters of p , l , d denote the period of the unit cell, the length of the hole and the thickness of the dielectric layer, respectively.

In this study, the cell period and hole length are fixed at $300 \mu\text{m}$ and $150 \mu\text{m}$, respectively. The entire structure is free-standing by itself without the need to be put on some substrate.

The transmittance of the structure was measured by THz-TDS. The emitter and detector are both broadband photoconductive antennas driven by femtosecond laser with 800nm wavelength. Fig. 2-16(b) and (c) show the experimental transmission of the samples with different PI thicknesses and at different incident angles. By comparing our results with those reported in the literature, two MPP modes are identified [MPP1 and MPP2] as shown in Fig. 2-16. The large peak between the two MPP modes is the main electric resonant mode. From Fig. 2-16(b), one can see that the MPP1 mode has a weak dependence on either the incident angle or the dielectric layer thickness. This represents a mode with weak dispersion. On the contrary, the MPP2 mode exhibits a strong dependence on the incident angle as well as the dielectric layer thickness. For example, when the terahertz wave is at normal incidence and $d=12.5 \mu\text{m}$, the dip at around 0.8THz is quite weak. But when the incident angle is increased to 10 degrees, the dip becomes deep. When the angle is further increased to 20 degrees, the dip is split into two. If the dispersion curve for the MPP2 mode were drawn, one may actually observe this mode splitting due to the change in the coupling of the two layers arising from the change of the incident angle. From another point of view, when the incident angle of the terahertz wave is fixed at 20 degrees and the thickness of the dielectric layer is varied from $50 \mu\text{m}$ to $12.5 \mu\text{m}$, the dip also experiences a change from a shallow dip to a sharp dip and

then split into two dips as shown in Fig. 2-16(c). This mode then represents a mode with a large dispersion. According the theory of MPP, the MPP modes with $G_{0,z1}$ and $G_{z1,z1}$ [corresponding to the MPP1 and MPP2 modes shown Fig. 2-16, respectively] are clearly observed in our samples. The main electric resonant mode shows little dependence on the dielectric layer thickness but is a strong function of the incident angle. This behavior is typical of an electric resonant mode that is hardly affected by the coupling between two metallic films. The dispersion of these MPP modes is shown by Fig. 2-17.

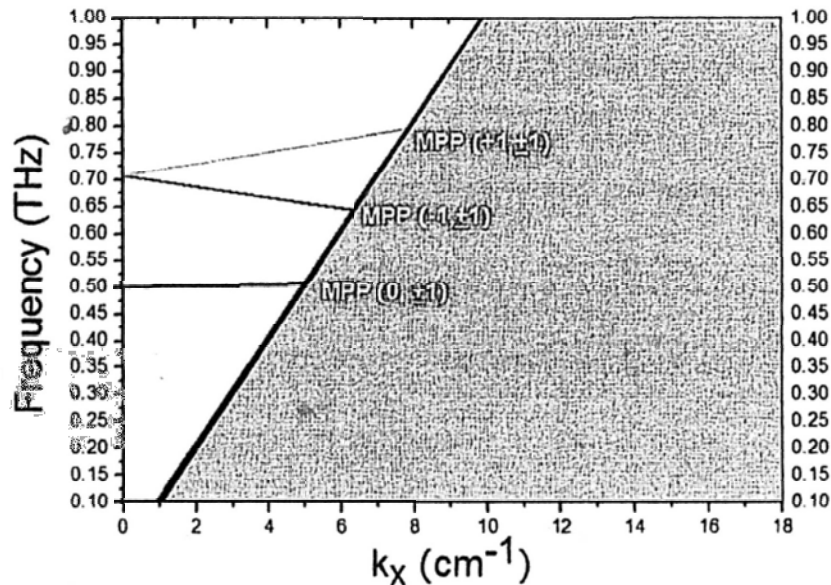


Fig. 2-17 Dispersion of the MPP modes.

Our experimental results reflect that the coupling between the two metallic layers greatly affect the dispersive MPP $G_{z1,z1}$ mode. An analogy of the coupling effect can be drawn by describing the structure by an LC -circuit model. In this dual-layer structure, each layer itself can form an LC -circuit and becomes resonant at a certain frequency. Since the two layers are coupled through the magnetic field

in the dielectric, it forms a capacitor whose capacitance will change when the thickness of the PI varies. Hence the entire structure will be described by a variable capacitor coupling the two *LC*-circuits that represent the two metallic layers. The coupling mechanism will be studied in detail by numerical simulations of this *LC*-circuit model.

2.4 Summary

The metal-dielectric interfaces support the propagation of surface plasmons. The permittivity of metal greatly affects the electromagnetic properties of the surface wave. At lower frequency ranging from infrared to far infrared, the confinement of the surface wave breaks down at the interface. Structured surfaces provide an efficient method to tailor the dispersion of the surface wave and make the effective medium perform as real metal. In far infrared regime, THz-TDS system provides a powerful tool to measure the response of plasmonic materials or devices.

References

1. N.W. Ashcroft, N.D. Mermin, "Solid state Physics," (Harcourt).
2. S.A. Maier, "Plasmonics: fundamentals and applications," Springer (2007).
3. P.B. Johnson, and R.W. Christy, "Optical constants of the noble metals," *Phys. Rev. B*, **6(12)**, 4370 (1972).
4. Paul R. West, Satoshi Ishii 1, Gururaj V. Naik1 et al., "Searching for better plasmonic materials," *Laser Photonics Rev.* **4**, 795 (2010).
5. M. A. Ordal, L. L. Long, R. J. Bell et al., "Optical properties of the metals Al, Co, Cu, Au, Fe, Pb, Ni, Pd, Pt, Ag, Ti, and W in the infrared and far infrared," *Applied Optics* **22**, 1099 (1983).
6. K. Wang et al., "Metal wires for terahertz wave guiding," *Nature* **432**, 376 (2005).
7. H. Raether, "Surface Plasmons on Smooth and Rough Surfaces and on Gratings," (Springer-Verlag, Berlin, Heidelberg, New York, London, Paris, Tokyo, 1986).
8. J.B. Pendry, L. Martin-Moreno, F.J. Garcia-Vidal, "Mimicking surface plasmons with structured surfaces," *Science* **305**, 847 (2004).
9. C.R. Williams, S.R. Andrews, S.A. Maier, A.I. Fernandez-Dominguez, L. Martin-Moreno, F.J. Garcia-Vidal, "Highly confined guiding of terahertz surface plasmon polaritons on structured metal surfaces," *Nature Photonics* **2**, 175 (2008).
10. S.A. Maier, S.R. Andrews, "Terahertz pulse propagation using

- plasmon-polariton-like surface modes on structured conductive surfaces,” *Appl. Phys. Lett.* **88**, 251120 (2006).
11. Alastair P. Hibbins, Benjamin R. Evans, J. Roy Sambles, “Experimental Verification of Designer Surface Plasmons,” *Science* **308**, 670 (2004).
 12. F J Garcia-Vidal, L Mart’ın-Moreno and J B Pendry, “Surfaces with holes in them: new plasmonic metamaterials,” *J. Opt. A: Pure Appl. Opt.* **7**, S97 (2005).
 13. S. L. Dexheimer, “Terahertz Spectroscopy: Principles and Applications,” CRC Press (2008).
 14. http://en.wikipedia.org/wiki/Terahertz_time-domain_spectroscopy.
 15. R.A. Shelby, D.R. Smith, and S. Schultz, “Experimental verification of a negative index of refraction,” *Nature* **292**, 77-79 (1997).
 16. J.B. Pendry, D. Schurig, D.R. Smith, “Controlling electromagnetic fields,” *Science* **312**, 1780-1782 (2006).
 17. J.B. Pendry, “Negative refraction makes a perfect lens,” *Phys. Rev. Lett.* **85**, 3966-3999 (2000).
 18. N.H. Shen, G. Kennanakis, M. Kafesaki, N. Katsarakis, E.N. Economou, C.M. Soukoulis, “Parametric investigation and analysis of fishnet metamaterials in the microwave regime,” *J. Opt. Soc. Am. B* **26**, B61-B67 (2009).
 19. M. Kafesaki, I. Tsiapa, N. Katsarakis, Th. Koschny, C.M. Soukoulis, E.N. Economou, “Left-handed metamaterials: The fishnet structure and its variations,” *Phy. Rev. B* **75**, 235114 (2007).
 20. G. Dolling, M. Wegener, A. Schadle, S. Burger, S. Linden, “Observation of

-
- magnetization in negative-index photonic metamaterials,” *Appl. Phys. Lett.* **89**, 231118 (2006).
21. T. Li, J.Q. Li, F.M. Wang, Q.J. Wang, H. Liu, S.N. Zhu, Y.Y. Zhu, “Exploring magnetic plasmon polaritons in optical transmission through hole arrays perforated in trilayer structures,” *Appl. Phys. Lett.* **90**, 251112 (2007).
22. T. Li, S.M. Wang, H. Liu, J.Q. Li, F.M. Wang, S.N. Zhu, X. Zhang, “Dispersion of magnetic plasmon polaritons in perforated trilayer metamaterials,” *Appl. Phys. Lett.* **103**, 023104 (2008).

Chapter 3: THz transmission in plasmonic structure

3.1 Introduction

Periodic metal structure with unit cell dimension less than the wavelength has been extensively investigated. The research on SPR has stimulated intense studies on micro- and nano-structures for a wide range of applications [1]. Many fascinating features were found in metal optics, such as extraordinary optical transmission (EOT) [2], negative refractive index [3] and etc. Although the physics of plasmons has been extensively discussed for a long time [4, 5], there is still a lack of systematic study of how the geometric features of the structures, such as hole-shape or periodicity, affect the electromagnetic properties of the devices [6, 7]. In certain simple single-layer designs, some basic theory such as Babinet principle [8] and Wood's anomaly [9] have been employed to understand their experimental results. An introduction of surface roughness or artificial structures to these devices provides a convenient way to modify their electromagnetic response. In the terahertz (THz) range, the properties of metals are different from those in the optical range. Plasmons in the THz range are called "spoof plasmons" to indicate their distinct features, such as poor confinement on the metal-dielectric interface [10, 11]. Recently, microscopic coupling in sub-wavelength structures has attracted much attention for its interesting macroscopic behavior [12]. To explore more exotic devices, a deep-insight understanding toward single layer case is necessary.

As we mentioned in Chapter 2, the dispersion of the surface wave in the periodic structure can be given out by momentum conservation relation described by equation (2.35). In terahertz range, due to the less dispersion and PEC-like property of metal, some equations in optical range can be simplified. Suppose k -vector is a complex number with real and imaginary part:

$$k_x = \frac{\omega}{c} \left(\frac{\varepsilon_1 \varepsilon_2}{\varepsilon_1 + \varepsilon_2} \right)^{\frac{1}{2}} = k' + ik'' \quad (3.1)$$

Here $\varepsilon_1 = \varepsilon_1' + i\varepsilon_1''$ is the permittivity of metal and ε_2 is that of dielectric. In terahertz frequencies, we have:

$$\varepsilon_2 \ll \varepsilon_1, \varepsilon_1'' > |\varepsilon_1'| \quad (3.2)$$

This relation results in a simplified relation:

$$k' = \frac{\omega}{c} \sqrt{\varepsilon_2} \quad (3.3a)$$

$$k'' = \frac{\omega}{c} \frac{\varepsilon_2^{3/2}}{2\varepsilon_1''} \quad (3.3b)$$

This equation shows that in different dielectric interface, the resonant frequency for the surface wave depends on the permittivity of the medium. Fig. 3-1 shows a typical result of the transmittance for a free-standing THz bandpass filter. The structure is formed by single-layer metal with array of cross holes. The dimension of the unit cell is $(G, K, J) = (413.75, 280, 87.5)$ μm . G , K and J are shown in the inset figure. The simulation was performed in Ansoft High Frequency Structure Simulator (HFSS). The resonant peaks for $(m, n) = (1, 0)$ and $(1, 1)$ mode for the air-metal interface are marked in the curve. According to Babinet's Principle, the band-stop structure can be obtained by the array of cross particles. A detailed

review on these two types of structure is given by Ref. [13]. But still there is a lack of discussion on the interaction between these two types of structures.

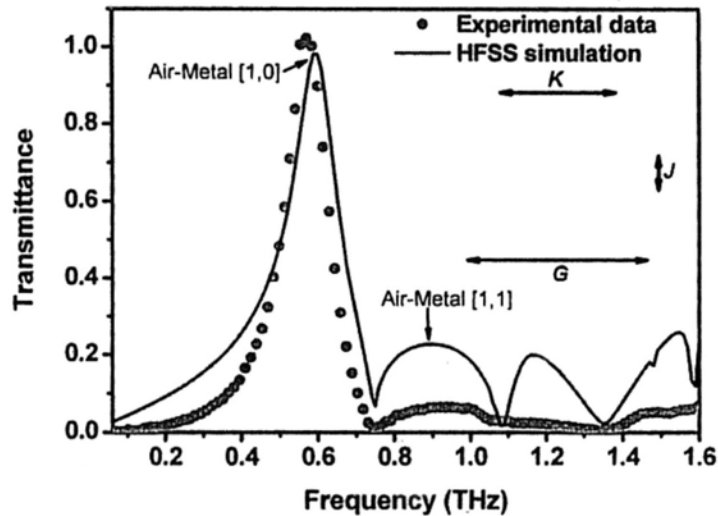


Fig. 3-1 Free Standing Terahertz Bandpass Filter (Measurement Result and Simulation Result).

3.2 Multimode transmission in complementary plasmonic structure

In this part, we discuss a 3-dimensional (3D) structure composed of two metallic layers of complementary cross patterns sandwiching a polyimide dielectric. Three transmission peaks in the terahertz range are clearly observed experimentally for devices with different dimensions of the same structure. These resonant peaks agree very well with those obtained from simulation. The results will be presented in detail and the origins of the resonances will be discussed later in this part. The multi-peak spectra may help the design of multi-mode THz filters, THz waveguide

and potentially benefit future biosensing and communication applications.

3.2.1 Mode splitting due to the coupling

The schematic of our structure is shown in Fig. 3-2(a), where G is the periodicity of the unit cell, K is the cross member length and J is the cross member width. The dielectric layer between the two metal layers has been omitted for clarity. The cross pattern is selected here as the unit cell because it has been studied widely as terahertz bandpass filters with a multi-layer structure and negative refractive index [14, 15]. The upper metal layer is made of an array of periodic crosses while the lower layer is a piece of metal film with periodic cross-holes exactly aligned with the metal crosses above them. The thickness of the middle layer, H , is very important as it greatly affects the multi-mode properties to be discussed in below.

The samples are fabricated by conventional photolithography technique and the middle layer is polyimide with variable thicknesses. In this letter, two samples, whose (G, K, J) values are (301, 195, 29) μm and (402, 260, 76) μm , are studied. The metal films are deposited by sputtering 1.5 μm -thick copper layers on the polyimide thin film. Measurements are conducted in a broadband terahertz time-domain spectroscopy (THz-TDS) system configured with a standard 8-F confocal setup. The emitter and the detector of the system are two bowtie photoconductive antennas. At the point where the sample is placed, the THz beam waist is about 5.5mm. The simulated and experimental transmission characteristics of two samples with dimensions (301, 195, 29) μm on 25 μm polyimide (Sample A) and (402, 260, 76) μm on 50 μm polyimide (Sample B) are shown in Figs. 3-2(b)

and (c), respectively. The simulation has been carried out by FIT-based (Finite Integration Technique) software CST Micro Wave Studio (CST-MWS). The metal layers are modeled as a perfect electric conductor and the experimental transmittance has been normalized with respect to that of the polyimide.

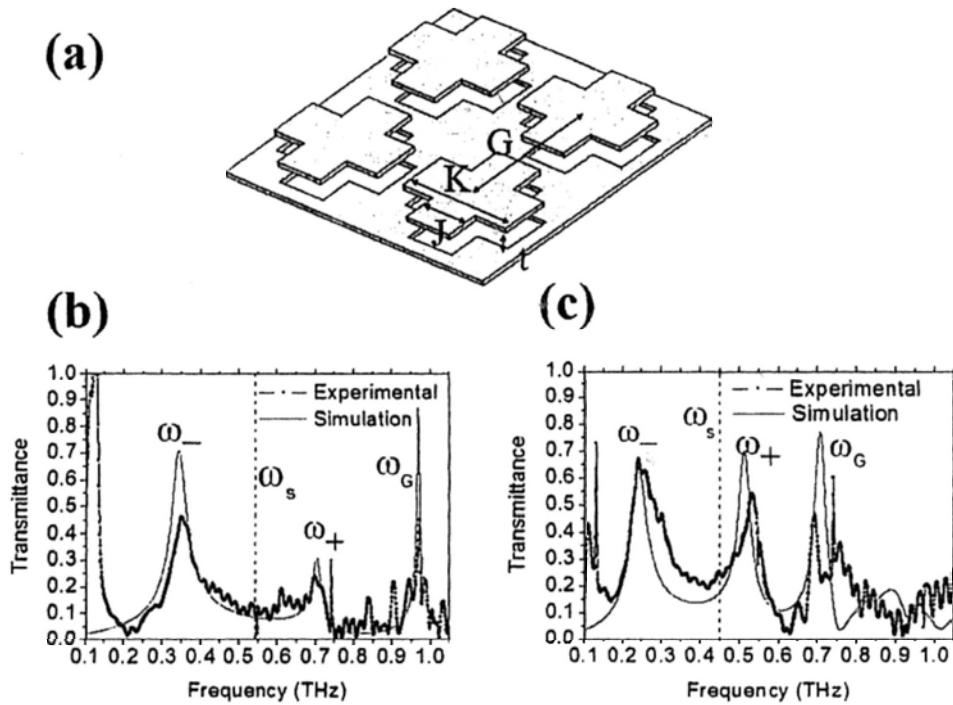


Fig. 3-2 (a) Schematic of the complementary structure. G , K and J denote the period of the structure, the member length and the member width of the cross, respectively. Measured and simulated transmittance through the structure for samples with $(G, K, J) = (301, 195, 29) \mu\text{m}$ (b) and $(402, 260, 76) \mu\text{m}$ (c). The dashed lines show the resonant frequency for the single layer case. Wood's anomaly is indicated by \star .

Three peaks can be clearly observed in both samples and they match well with those obtained by simulation. The sharp dip at around 0.55THz and the spike at

0.74THz are caused by the absorption of water vapor [16]. Because the samples are free-standing, which helps to eliminate the effects arising from an additional substrate, the curvature of the sample surface may generate some slight shifts in the peak positions. The dashed line in each figure shows the experimental and simulated resonant frequency, ω_s , of an identical structure fabricated similarly but without the upper metal layer. These devices with a single metal layer patterned with cross-holes are labeled as Sample A_s and Sample B_s, corresponding respectively to the otherwise identical Samples A and B. The relationship between ω_s and the first two peaks in each figure will be discussed in the following analysis.

A deeper insight into the nature of the three resonant modes, labeled as ω_- , ω_+ , and ω_G from low to high frequencies as shown in Fig. 3-2, can be obtained by comparing their corresponding current distributions on the metal surface. The current distributions are also calculated by CST-MWS. Fig. 3-3(a) shows the current distributions corresponding to the ω_- mode in Sample A. The solid arrow shows the direction of the current on the upper layer and the two dashed arrows show those on the lower complementary layer. The polarization of the incident wave is given as shown. Similarly, Fig. 3-3(b) shows the corresponding surface current distributions of the ω_+ mode on the same sample. The major difference between the two modes is that the directions of the currents on the upper layer are opposite to each other, which results in an entirely different coupling between the fields surrounding the upper and lower metal layers. Similar current distributions are also obtained for Sample B.

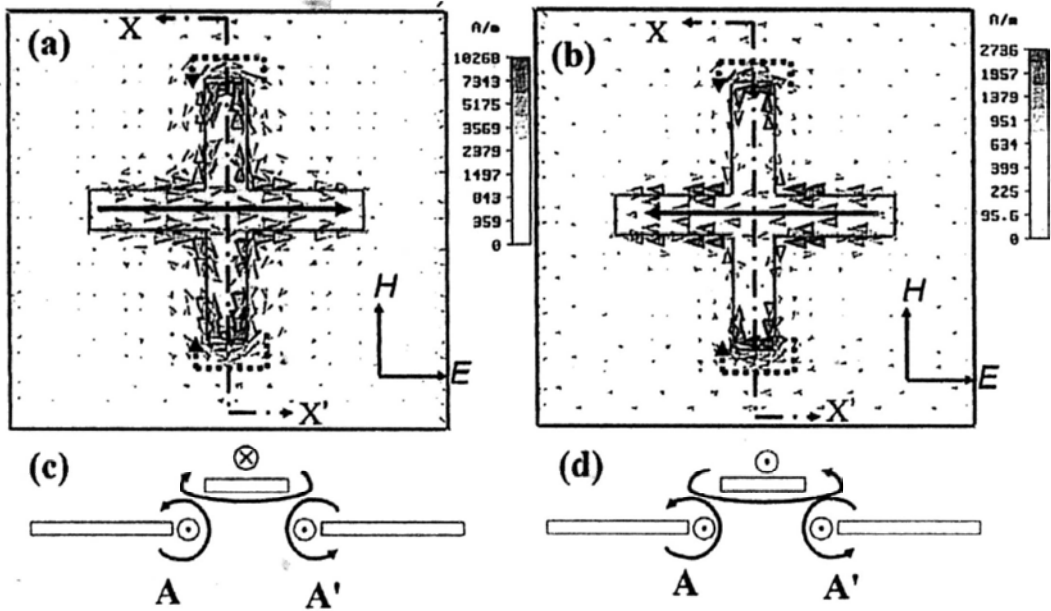


Fig. 3-3 (a) and (b): The simulated current distributions calculated by CST Micro Wave Studio for the ω^- and ω^+ modes, respectively; (c) and (d): a pictorial pattern of the magnetic field corresponding to the ω^- and ω^+ modes, respectively, in the cross-section plane XX' .

Fig. 3-3(c) shows a pictorial pattern of the magnetic field corresponding to the ω^- mode in the cross-section plane along $X-X'$ when viewed along the direction of the electric field vector. It is clear that in the regions around A and A', the magnetic field due to the upper layer is in the same direction as those due to the lower layer. If one views magnetic coupling as the occurrence of mutual inductance, then the net inductance responsible for resonance in this scenario will be increased by virtue of the additional parallel field over that of the single layer device, such as Sample A_s, thereby leading to a resonant frequency, ω^- , which is lower than ω_s of Sample A_s as shown in Fig. 3-2(b). On the other hand, Fig. 3-3(d) shows the corresponding magnetic field pattern for the ω^+ mode, where the fields are anti-parallel around A

and A' . By the same argument, the net inductance will be reduced by the coupling effect, which should result in a resonant frequency, ω_+ , that is higher than ω_S . Hence the ω_- and ω_+ modes in this complementary structure can be considered to arise from the field-coupling between one patterned metal layer and its complementary counterpart. Furthermore, Figs. 3-2(b) and (c) show that both the experimental and simulated relative strength ratios between the ω_+ and ω_- modes increase with the spacing between the two metal layers [25 μm in Fig. 3-2(b) and 50 μm in Fig. 3-2(c)].

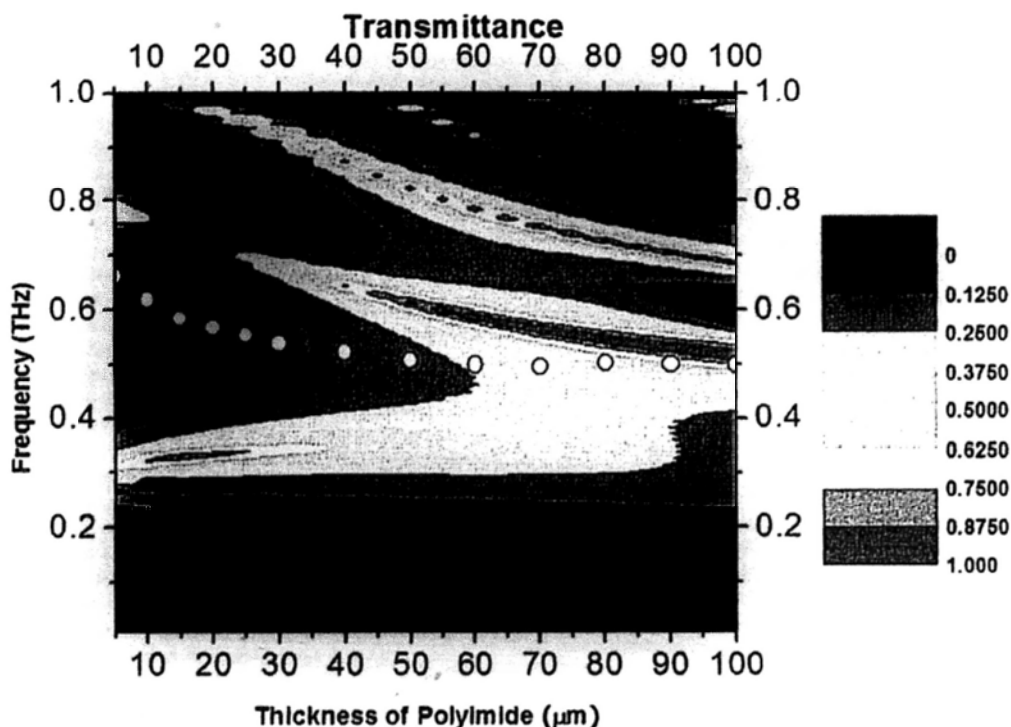


Fig. 3-4 Simulated transmission characteristics of Sample A as a function of dielectric thickness H . The circles indicate the resonant frequencies of Sample A_S .

As mentioned above, the thickness H of the middle dielectric layer greatly

affects the resonant modes in the structure by changing the field interaction between the two metal layers. Intuitively, a large H implies very little interaction and a small H will enhance the field coupling. Therefore simulations have been performed on the structure represented by Sample A to obtain its transmission characteristics at various dielectric thicknesses. The simulation results are shown in Fig. 3-4, where the transmitted intensity is color-coded in order to show its dependence on both frequency and polyimide layer thickness simultaneously. For comparison, the resonant frequency, ω_S , of Sample A_s is also shown as a function of the polyimide layer thickness (circle). It is very obvious that as H increases, the ω_- and ω_+ modes tend to merge together to become one mode whose resonant frequency is identical to ω_S of Sample A_s with the same polyimide thickness. The current distributions of the ω_- and ω_+ mode on the lower (cross-hole) metal layer in Sample A are observed to mimic those of Sample A_s when H reaches $100 \mu\text{m}$ and that may explain why ω_+ tends to merge with ω_S . Simultaneously, the current distributions on the upper (solid cross) metal layer of Sample A become very weak, which also reflects the lack of a distinct peak at ω_- . The effects of varying the coupling between two stacked layers of periodic split-ring resonators (SRRs) have also been analyzed by an equivalent LC circuit model with a mutual inductance derived from the coupling of the SRRs [12], although in that case the coupling is varied by changing the relative orientation between the upper and lower SRRs instead of the spacing between them. Figure 4 also clearly echoes our earlier claim that the ω_- mode gradually loses its strength relative to the ω_+ mode as H increases. Lastly, it is also observed that the ω_G mode

tends to shift to a lower frequency at large H . This happens because the effective refractive index becomes larger, thereby increasing the wavelength of the surface wave propagating along the patterned surface.

3.2.2 Bloch state in periodic structures

Regarding the third mode represented by ω_G , it is believed to arise from the excitation of the Bloch state in periodic structures. (The dip at around the lattice period is due to Wood's Anomaly [9].) One evidence can be obtained by comparing this mode in both Samples A and B, where the resonant frequencies are approximately equal to the velocity of light divided by the respective periodicity of the cross patterns. An indirect verification of this collective effect is obtained by measuring Sample A in another ZnTe-crystal-based THz-TDS system where the beam waist is just 0.8mm, which is much smaller than the 5.5mm in the previous setup. The transmission curve is given in Fig. 3-5(a), which shows that the ω_G mode representing the collective effect of periodic unit cells becomes unobservable here because the excitation area is too small (just covering a few cells). This is in sharp contrast to the ω_- and ω_+ modes which are still quite significant. Fig. 3-5(b) shows the simulated surface current distributions in Sample A for this mode (Sample B shows very similar distributions), which are very different from those for the other two modes. Here the currents are dispersed throughout the whole surface of the unit cell instead of being primarily concentrated around the cross region. This reaffirms the global aspect of the present mode versus the localized effect in the other two modes. To assess the effect of unit cell periodicity on the ω_G mode, simulations

have been performed by varying the periodicity of Sample A but keeping its cross-pattern shape and size unchanged. The transmission characteristics obtained from the simulations are shown in Fig. 3-5(c). It is clearly observed that the frequency of the ω_G mode varies distinctly with the periodicity of the structure whereas the frequencies of the ω_- and ω_+ modes remain almost unchanged. Consequently, all of these results corroborate the hypothesis that the ω_G mode originates from the collective effect of the unit cells and is critically dependent on the periodicity of the structure.

In conclusion, we have investigated the multi-mode transmission properties of a complementary dual-metal-layer structure. The two lower frequency modes are due to localized coupling of fields between the two layers. The highest frequency mode is the propagating mode of the spoof surface plasmons and is therefore related to the period of the structure. Our device differs from those with identical periodic patterns on both metal layers, such as the fishnet device, in that the incident wave can 'see' the entire area of the device here whereas only the metallic portion of the device can be 'seen' by the wave in the fishnet structure. Hence very high transmission efficiency at the resonant modes can be achieved. In addition, the relative amplitudes of the three transmission modes can be tuned by changing the geometrical design of the structure. Lastly, the free-standing nature of our device eliminates all substrate effects and results in a good agreement between simulation and experimental results.

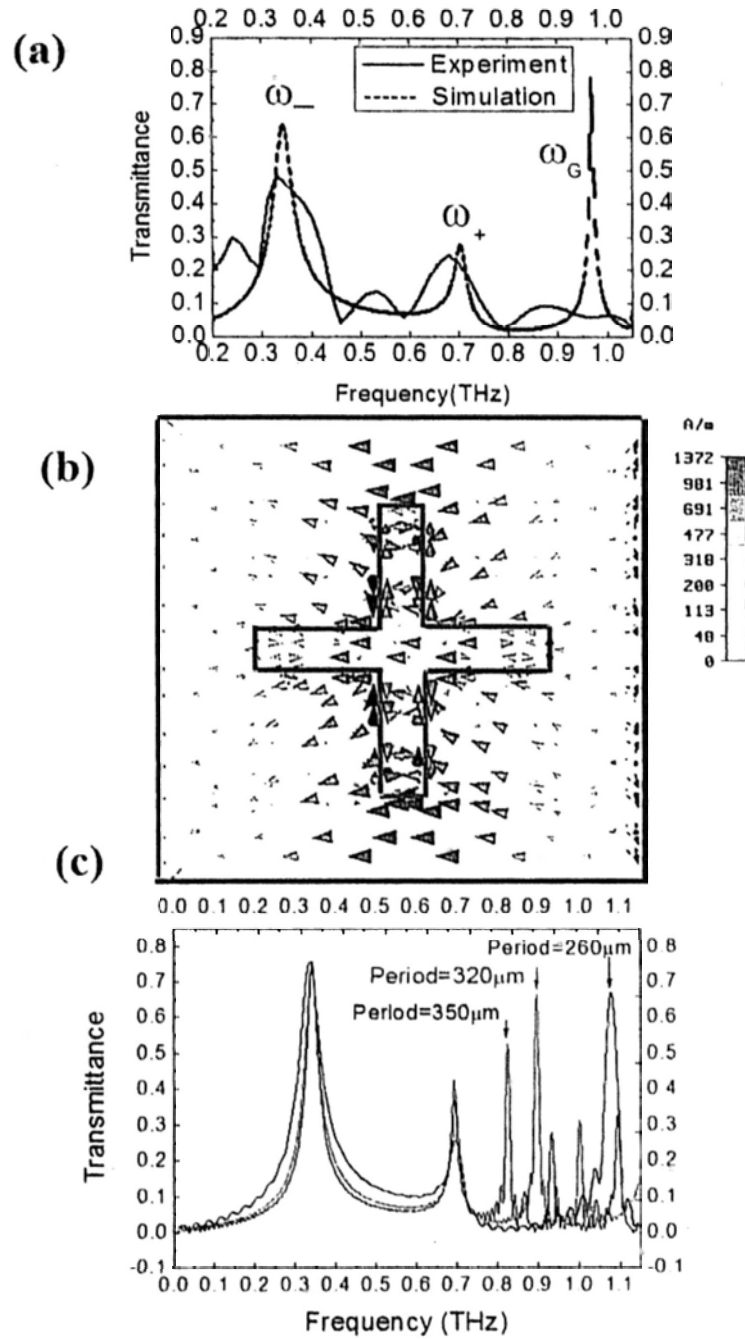


Fig. 3-5 (a) Transmission curve measured in a THz-TDS system with beam waist around 0.8mm; (b) The simulated current distributions for the ω_G mode; (c) Simulated transmission curves for samples with different unit cell periods but the same patterned shape and size as Sample A.

3.3 Polarization-dependent plasmonic coupling in dual-layer structure

As a continuous work of the previous part, dual-layer metallic wire-hole structures were fabricated and their terahertz transmission properties were measured. They exhibit polarization-dependent transmittance with large extinction ratios. Simulation and experimental results on structures with different wire-to-hole orientations provide strong evidence that the resonance peaks are caused by plasmonic coupling between the two metallic layers. A simplified *LC*-circuit model is proposed to explain the coupling mechanism and to estimate the peak frequencies. Our results suggest that specific electromagnetic response can be achieved by appropriate design of the geometrical patterns on the two metallic layers and a suitable polarization of the incident wave.

3.3.1 Polarization-sensitive transmission

Complementary plasmonic structures have been proposed and demonstrated in the THz range [17] and optical range [18, 19]. They provide a simple but useful platform for studies on the 3-dimensional couplings between two patterned metallic layers separated by a dielectric.

In this chapter, the interaction between two patterned metallic layers in the THz range is reported. Our simulation and experimental results show that when excited by a certain polarized wave, the wire-and-hole structure proposed here can achieve the same transmittance response as the complementary cross structure reported earlier [17]. The numerical results demonstrate that the electric or magnetic fields of

the incident wave can be modulated by the wire array or hole array, respectively, on either of the two metallic patterns.

The proposed structure is composed of one layer of metal wire array (WL) and one layer of metal hole array (HL) separated by a layer of polyimide of thickness d . The schematic of the structure is shown in Fig. 3-6. The parameters l , w , and p define the wire/hole length, wire/hole width and period of the unit cell respectively. The angle between the long side of the holes and the y -axis, β , can be adjusted between 0° and 90° as shown in Fig. 3-6(b). A cross section view cut through the holes shown in Fig. 3-6(a) is given in Fig. 3-6(c).

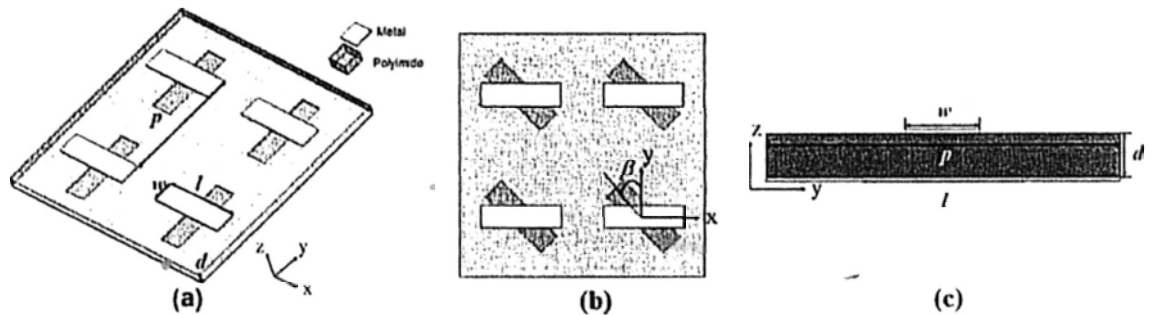


Fig.3-6 Schematic of the wire-hole structure. (a) 3-dimensional view; (b) x-y plane view; and (c) y-z plane view.

The patterns were written by conventional photolithography on both sides of the polyimide film. The 2- μm -thick copper layers were deposited by sputtering followed by liftoff. Samples with different β values but identical p , l , w and d values of 402, 260, 76 and 50 μm , respectively, were fabricated in this study. The measurement was conducted in a standard 8-F confocal THz time domain spectroscopy (THz-TDS) system. The THz emitter and detector in the THz beam

waist is around 5mm. The system works in an environment of dry compressed air with negligible water absorption. Our simulations were carried out by CST Micro Wave Studio (CST-MWS). The copper layer was modeled as a perfect electric conductor (PEC) and the permittivity of polyimide was taken as 3.9. The experimental transmittance of the structures was normalized by that of a single polyimide layer. Fig. 2 compares the experimental transmittance (red line with circles) with the simulation results (black line with squares). Fig. 3-7(a) and (d) show the transmittance of the sample with $\beta=0^\circ$. The inset shows the polarization directions of the incident wave. In Fig. 3-7(a), the electric field is parallel to the wire and both the WL and HL are in resonance at the three major plasmonic peaks shown. These plasmonic peaks are exactly the same as those obtained from the complementary cross structure with cross dimensions identical to those formed by the wire and hole in the present structure [17]. This result implies that the complementary (complicated) structure can be replaced by the present (simple) wire-hole structure to achieve the same transmittance. Fig. 3-7(d) shows that when the electric field is perpendicular to the wire, the transmittance of the structure is much smaller. In this case, both the WL and HL are non-resonant with the incident wave over the measured range of frequencies, with the WL exhibiting almost unity transmission and the HL showing little transmission. Despite the nearly opaque behavior of the HL, the WL-HL coupling produces some enhancements in the transmittance at some frequencies. But the overall transmittance of the structure is low. The physics of the coupling mechanism will be analyzed in below by

introducing the *LC*-model. Similarly, Fig. 3-7(b) and (e) show the transmission spectra with $\beta=60^\circ$ while Fig. 3-7(c) and (f) are for $\beta=90^\circ$. All of the results show a fairly good match between simulation and experiment. They demonstrate that β affects the response of the device according to the polarization direction of the excitation wave. In fact this polarization selection property with large extinction ratios has indeed been observed in complementary structures in the optical range [18].

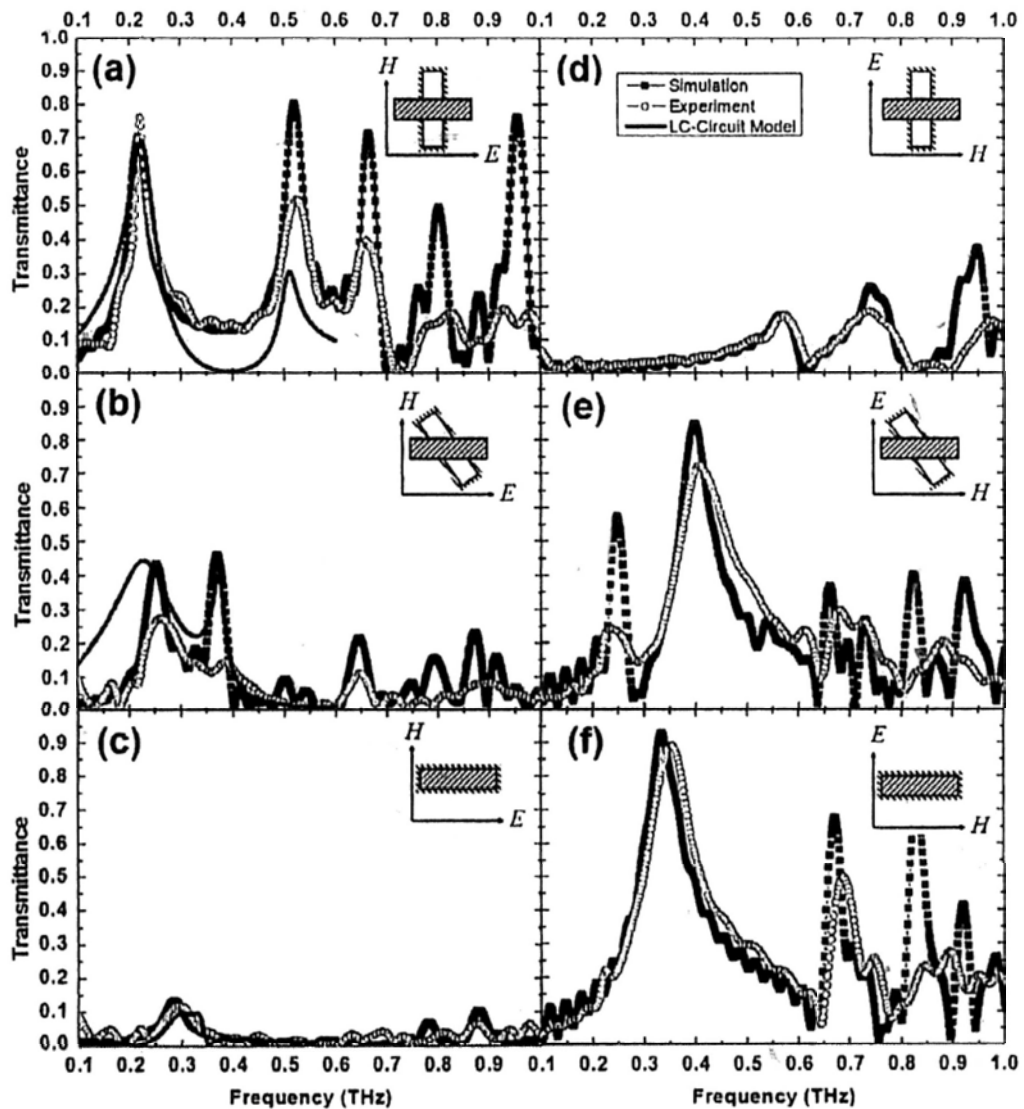


Fig. 3-7 Experimental and simulation result for (a) $\beta = 0^\circ$, $E//\text{wire}$; (b) $\beta = 60^\circ$, $E//\text{wire}$; (c) $\beta = 90^\circ$, $E//\text{wire}$; (d) $\beta = 0^\circ$, $E \perp \text{wire}$; (e) $\beta = 60^\circ$, $E \perp \text{wire}$; and (f) $\beta = 90^\circ$, $E \perp \text{wire}$. The blue curves in (a)-(c) show the transmittance obtained by using LC -circuit model.

3.3.2 LC circuit model

As the single layer structure can be described by an LC -circuit model, whether it be WL (capacitive and corresponding to a series resonant circuit) or HL (inductive and corresponding to a parallel resonant circuit), here we represent our dual-layer structure by two LC -circuits coupled by a mutual inductance M as shown in Fig.3-8 (a). In this circuit, C_1 , C_2 and L_1 , L_2 denote the respective native capacitance and inductance of the HL and WL, with Z_0 and Z_d representing the impedance of air and dielectric, respectively. The mutual inductance, L_1 and L_2 have been redistributed as 3 inductances L_1-M , L_2-M and M and connected as shown in the figure. The parallel circuit should behave like an open circuit whereas the series circuit should behave like a short circuit at resonance. Hence Fig. 3-8(b) or (c) is the equivalent circuit at resonance, differing only in the sign of the inductive coupling. In order to obtain a simplified equation of mode hybridization or splitting due to the coupling effect, two approximations are assumed: (1) The resonant frequencies of the single WL and HL are the same, i.e. $\omega_{01} = \omega_{02} = \omega_0 = 1/\sqrt{L_i C_i}$ ($i = 1, 2$). This condition implies that the Babinet principle is obeyed in this case. In reality, ω_{01} and ω_{02} will differ slightly owing to the substrate effect. (2) Resistive dissipation is neglected so that the equivalent circuit does not contain any resistor. Then two differential equations can be obtained:

$$L_1\ddot{q}_1 - M\ddot{q}_2 + q_1/C_1 = 0 \quad (3.4a)$$

$$L_2\ddot{q}_2 - M\ddot{q}_1 + q_2/C_2 = 0 \quad (3.4b)$$

where q_1 and q_2 denote the accumulated charges in the capacitors C_1 and C_2 respectively. The resulting hybridized resonant frequencies can be written as:

$$\omega_{\mp} = \frac{\omega_0}{\sqrt{1 \pm M / \sqrt{L_1 * L_2}}} \quad (3.5)$$

Frequency ω_- results from additive magnetic field coupling while ω_+ results from subtractive magnetic field coupling, as indicated by the additive induction currents in Fig. 3-8(b) or by the subtractive induction currents in Fig. 3-8(c). The magnetic field intensity in the structure is calculated to verify this mode hybridization. Fig. 3-8(d) and (e) show the simulated magnetic field distributions in the structure at the resonant frequencies of 0.21THz and 0.52THz, respectively, given in Fig. 3-7(a). They show clearly the additive and subtractive field effects as expected. A pictorial description of the magnetic field vectors caused by conducting currents is given by the white arrows. The surface currents, indicated by \otimes and \odot , flow in opposite directions on WL and HL for additive magnetic field coupling but along the same direction for subtractive field coupling.

To get a deeper insight into the relationship between the parameters of the LC-circuit to the coupling effect, the circuit shown in Fig. 3(a) was studied by Advanced Design System (ADS). The inductance and capacitance values in the LC-circuit are difficult to estimate without knowing the transmission loss of the

structure, although some empirical calculations of resonant frequencies and transmittance of mesh structures have been reported [20, 21]. From the resonant frequency and 3dB-bandwidth, the parameters in the LC -circuit of dual-layer structure can be estimated. Table 3.1 lists the parameters which are used to calculate the blue curves shown in Fig. 3-6(a)-(c). The parameters C_1 , C_2 , L_1 and L_2 were estimated from the single layer case and mutual inductance M was deduced from equation (3.5). It is clear that our simple LC -circuit model can reproduce approximately the same frequency response as obtained by electromagnetic simulation.

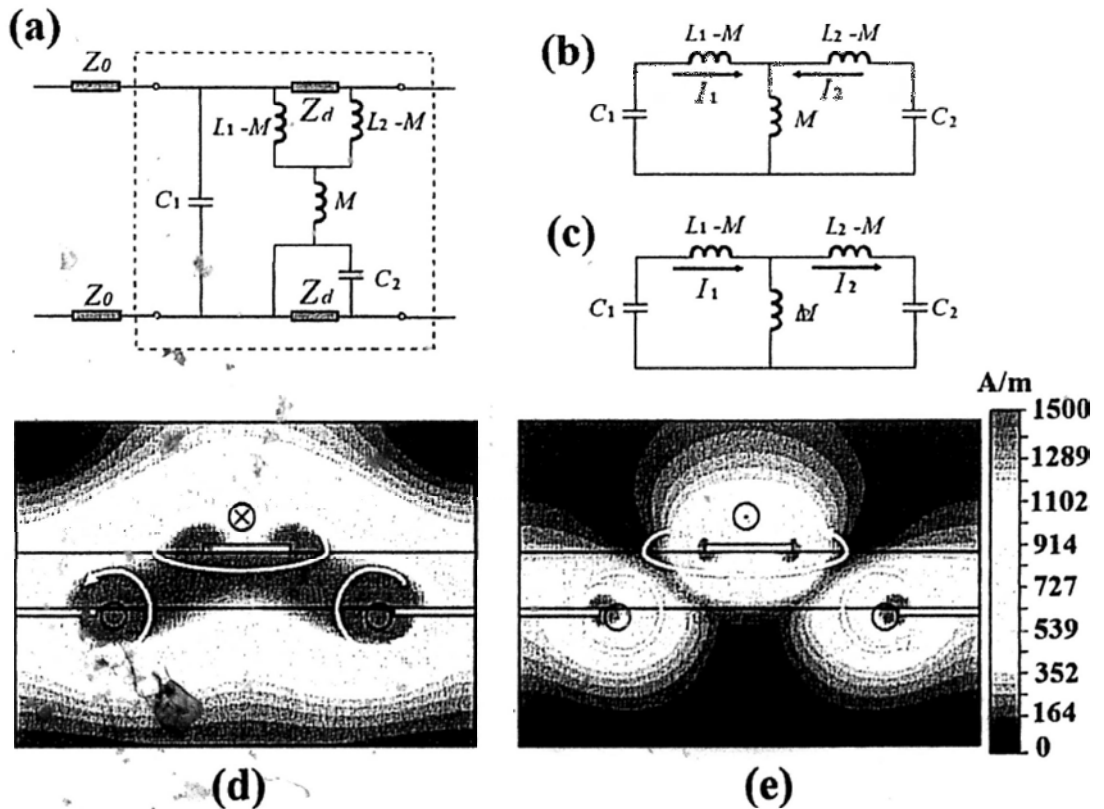


Fig. 3-8 (a) Inductively coupled LC -circuit for the structure; (b) Equivalent circuit with additive magnetic coupling; (c) Equivalent circuit with subtractive magnetic coupling; (d) Magnetic field distribution for (b); and (e) Magnetic field distribution for (c).

Table 3-1 Parameters in LC-circuit Model

β	L_1 (pH)	C_1 (fF)	L_2 (pH)	C_2 (fF)	M (pH)
0°	11.577	61.5	250	0.7463	43.578
60°	2.387	13.1	250	0.7463	8.549
90°	0.419	3.6	250	0.7463	-0

In order to demonstrate the effect of variable coupling between the two metal layers without changing their spacing, the transmittance of the structure was simulated while rotating the hole counterclockwise by 90°, i.e. changing the angle β from 0° to 90°, for two orthogonal polarizations and the results are shown in Fig. 3-9. For the single WL or single HL, each has two special states: the incident electric (for WL) or magnetic (for HL) field is either parallel or perpendicular to its long edge, labeled respectively as $WL_{//}$, WL_{\perp} , $HL_{//}$ and HL_{\perp} . The properties of the single layer structures are quite well understood. For the $WL_{//}$, it exhibits a band-stop response where the electric field is strongly modulated at the resonant frequency. When the wire is rotated by 90° as in WL_{\perp} , broadband unity transmittance without resonance is obtained because of the large capacitive reactance in the structure. According to the Babinet principle, the case of $HL_{//}$ and HL_{\perp} can be inferred as: $HL_{//}$ exhibits a bandpass resonance whereas HL_{\perp} stops all the energy in a broadband range. When these two layers are coupled together, mode hybridization is produced and has been explained in above. When the two layers are both at resonance ($WL_{//}$, $HL_{//}$), which is the initial state of Fig. 3-9(a), mode hybridization is especially conspicuous and multi-mode transmission is experimentally confirmed as shown in Fig. 3-7(a). When the initial state changes

from $(WL_{//}, HL_{//})$ to $(WL_{//}, HL_{\perp})$, the HL_{\perp} layer will stop most of the transmitted energy and the two hybridized modes tend to merge together because of the weakened coupling resulting from a significantly reduced mutual inductance M in Fig. 3-7(a). Likewise, Fig. 3-9(b) shows the case when (WL_{\perp}, HL_{\perp}) changes to $(WL_{\perp}, HL_{//})$ where the WL_{\perp} layer is non-resonant throughout while the HL layer varies from non-resonant state to resonant state, finally resulting in a bandpass response which is also experimentally observed as shown in Fig. 3-7(f). Intermediate values of β will produce intermediate response, such as that observed experimentally for $\beta = 60^{\circ}$ [Fig. 3-7(b) and (e)]. Rotation of the wire will produce similar results and not be discussed here. Figure 3-9 clearly shows that the dual-layer structure can selectively modulate the electromagnetic wave as desired according to how the coupling is varied. In this investigation, the wire and hole of the same dimension have been chosen for modulating the electromagnetic wave. Other geometric patterns with different dimensions and symmetry properties can be employed to explore different modulations of the electromagnetic wave.

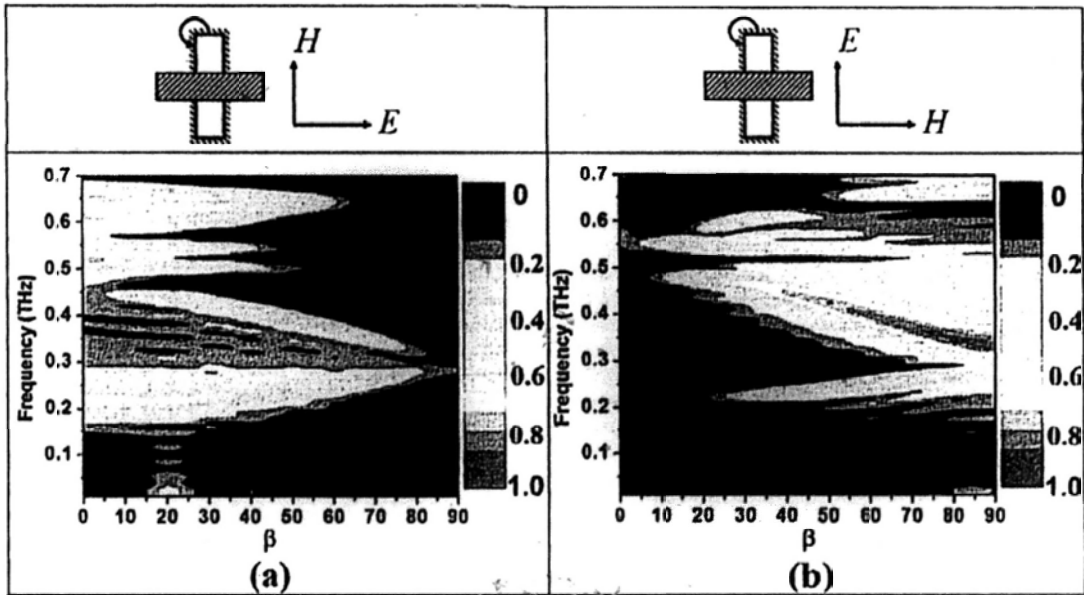


Fig. 3-9 State transition by changing ρ for (a) $E //$ wire and (b) $E \perp$ wire.

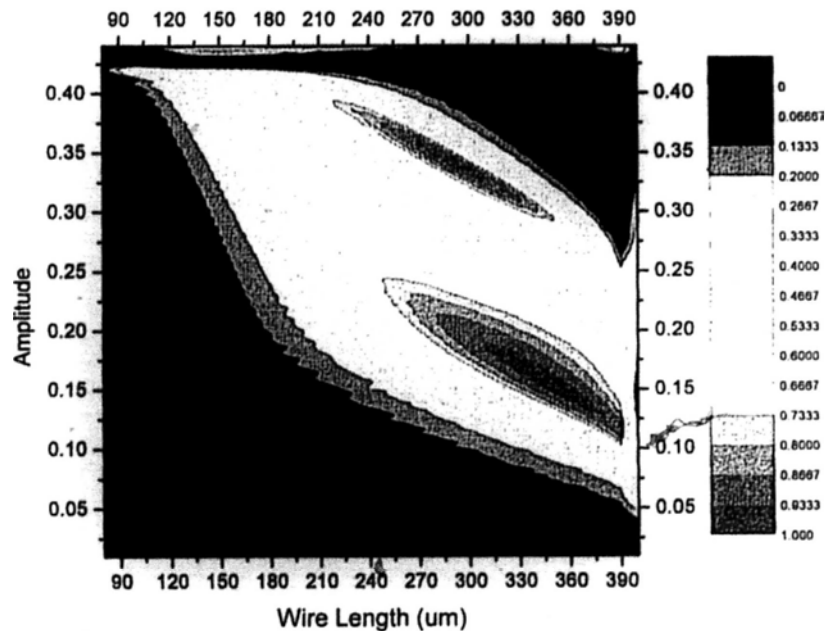
In conclusion, we have demonstrated a dual-layer wire-hole structure and analyzed its polarization dependent properties in detail and approximately reproduced its frequency response by an LC-circuit model. When the wire and hole structures are resonantly coupled, mode hybridization will lead to multi-mode transmission. By varying the angle between the wire and the hole and their orientation with respect to the polarization of the incident wave, one can tune the resonant states and the coupling strength in the dual-layer structure. Hence such structures and their variations should provide a versatile platform to custom-design specific electromagnetic response for useful applications.

3.4 Phase response of dual-layer structure

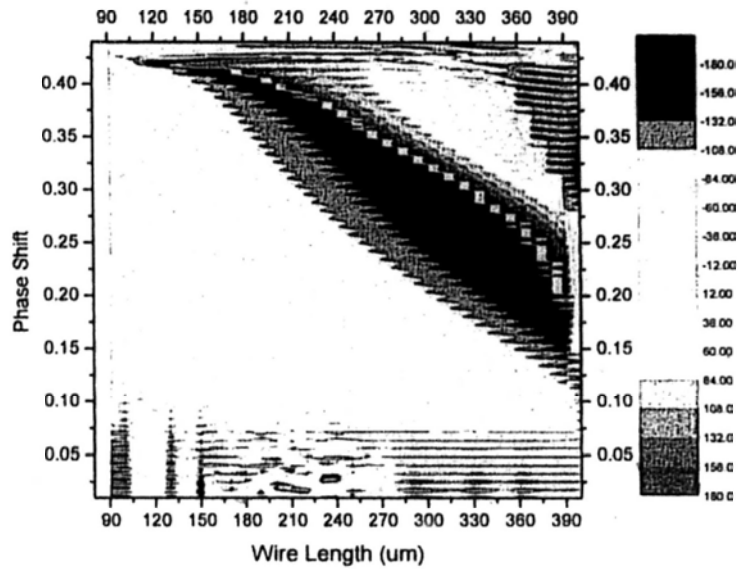
In many discussions, we usually pay much of our attention to the amplitude response of a device but ignore the phase. Actually, examination of phase response in the devices may get more physics and results in more potential applications.

3.4.1 0-to- 2π -phase-shift due to the coupling

As a continuous of our previous discussion, we choose the identical dimension structure for the discussion. The period of the structure is $G=402\mu\text{m}$, and cross width $J=78\mu\text{m}$. The length of the cross is a variable ranged from 80 to 400 μm . We examine the different amplitudes and phases during this variation process. The simulation result is shown by Fig. 3-10. In Fig. 3-10(a), the two red spots correspond to the coupled two modes. Look at the phase in Fig. 3-10(b). We can find that at the region of these two modes, the phase shift has a stable variation compared with other frequencies. When the wire width in the cross varies from 80 μm to 400 μm , the phase experiences a 2π shift. This is impossible for a single dipole resonance.



(a)



(b)

Fig. 3-10 (a) Amplitude and (b) phase response of the complementary structure with substrate.

The deeper investigation is needed for the mechanism of these two coupled modes. But with the knowledge of our previous discussion, the 2π -phase-shift is obviously due to the coupling of the two layers: each mode provides a π -phase-shift. When the geometry of the structure varies, it is possible to make these two modes resonant at the same frequency; then they can be spatially coupled. This point can be reflected by the equivalent circuit shown in Fig. 3-8(b) and (c).

3.4.2 Planar phase engineering devices

Making use of the phase “map” depending on the geometry can lead to many devices in the THz range similar to the optical range. A proof-of-concept simulation is performed to show how the unit cell with different phase response is tuned by the

geometry is spatially coupled.

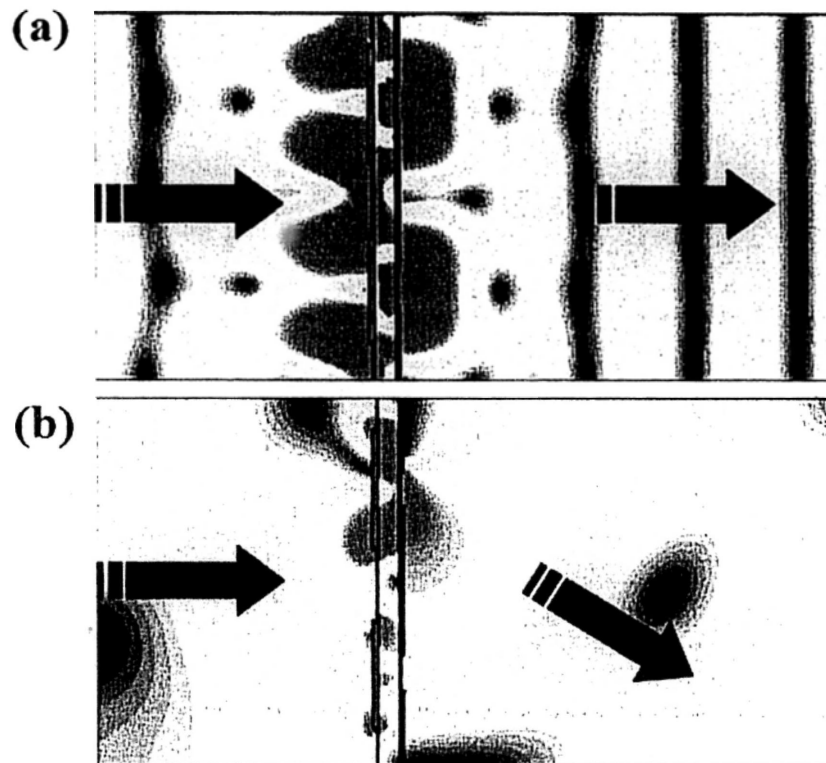
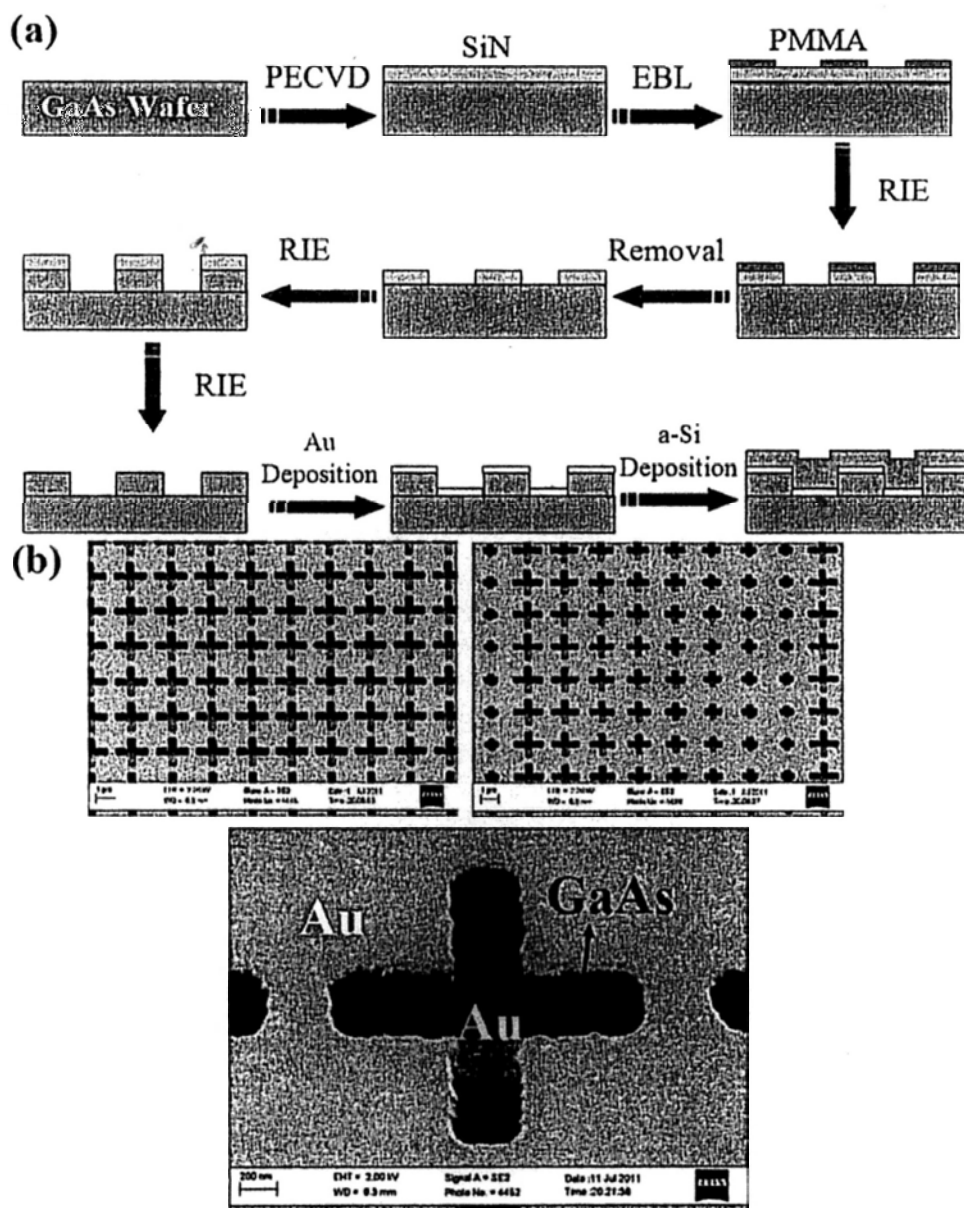


Fig. 3-11 Electric field in the structure for complementary structure (a) at the frequency without phase shift; (b) at the frequency with phase shift.

Fig. 3-11(a) shows the response of two unit cells with the same dimension. The same phase front can be observed for these two unit cells. But for the second one shown by Fig. 3-11(b), the dimension of the two unit cells is different. The wire length of the left unit cell is 260 μm and the right one is 230 μm . The pitch and wire width are both the same. The phase difference when passing through the sample is obviously different then the beam is bent to the right-hand side.

One batch of the complementary antennas in mid-IR range is fabricated and the process is shown by Fig. 3-12 (a). The patterns are written by electron beam lithography (EBL). With the mask of PMMA, we transfer the patterns to a SiN hard

mask and then to a GaAs wafer by Reactive Ion Etching (RIE). After the deposition of metal, the complementary dual-layer structure is created on the GaAs substrate. To match the impedance of the upper and lower layers, we deposit a layer of amorphous silicon on the structure using PECVD.



Then we use the FTIR microscope setup in the Capasso lab to characterize the

spectral response of the samples. The microscope allows both transmission and reflection measurement. Fig. 3-13 shows the primary result for the reflection measurement. We will compare the measurement results with the simulation results to help understand the underlying physics of the structures.

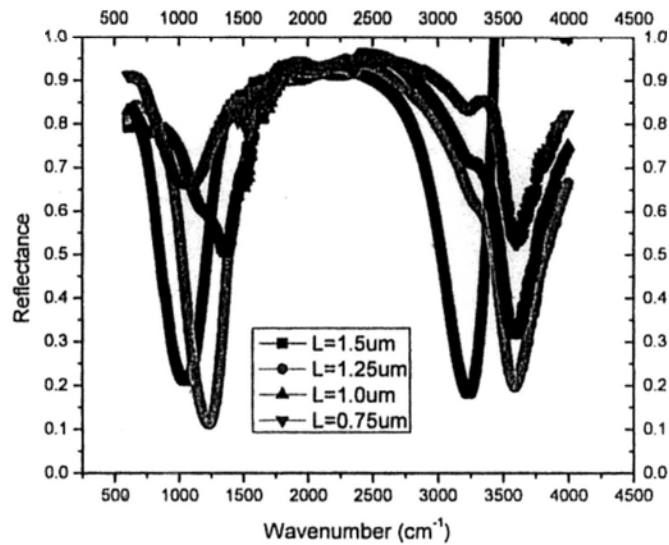


Fig. 3-13 Reflection spectra for cross width $W=250\text{nm}$ with different cross length L .

3.5 Summary

In this chapter, a 3-dimensional sub-wavelength structure with periodic complementary metal patterns operating in the terahertz range has been proposed and fabricated. The device clearly exhibits three transmission modes under normal incidence, where experimental results obtained by terahertz time domain spectroscopy and simulated results agree very well with each other. The multi-mode transmission characteristics are found to arise from both localized coupling of fields

between the interacting layers and propagating surface waves due to Bloch excitations on the surface of the periodic structure.

Based on the study of complementary structure, dual-layer metallic wire-hole structures were fabricated and their terahertz transmission properties were measured. They exhibit polarization-dependent transmittance with large extinction ratios. Simulation and experimental results on structures with different wire-to-hole orientations provide strong evidence that the resonance peaks are caused by plasmonic coupling between the two metallic layers. A simplified LC-circuit model is proposed to explain the coupling mechanism and to estimate the peak frequencies. Our results suggest that specific electromagnetic response can be achieved by appropriate design of the geometrical patterns on the two metallic layers and a suitable polarization of the incident wave.

After the full discussion on the amplitude response of the structure, we pay our attention to the phase response of the structure at the end of this chapter. The coupled two modes result in a 2π phase shift. Further experimental and theoretical investigation is needed for a deeper insight into the mechanism. Our future effort will be to fabricate more samples with various 2D phase patterns for different applications. The collected data is now being analyzed and further optimization of the samples is needed.

References

1. C. Genet and T. W. Ebbesen, "Light in tiny holes," *Nature* **445**, 39-46 (2007).
2. T. W. Ebbesen, H. J. Lezec, H. F. Ghaemi, T. Thio, and P. A. Wolff, "Extraordinary optical transmission through sub-wavelength hole arrays," *Nature* **391**, 667-669 (1998).
3. Vladimir M. Shalaev, "Optical negative-index metamaterials," *Nature Photonics* **1**, 41-48 (2007)..
4. S. A. Maier, *Plasmonics: Fundamentals and Applications*, (Springer, New York, 2007).
5. H. Raether, *Surface Plasmons on Smooth and Rough Surfaces and on Gratings*, (Springer-Verlag, Berlin, Heidelberg, New York, London, Paris, Tokyo, 1986).
6. Tatsunosuke Matsui, Amit Agrawal, Ajay Nahata, and Z. Valy Vardeny, "Transmission resonances through aperiodic arrays of subwavelength apertures," *Nature* **446**, 517-521 (2007).
7. K. J. Klein Koerkamp, S. Enoch, F. B. Segerink, N. F. van Hulst, and L. Kuipers, "Strong Influence of Hole Shape on Extraordinary Transmission through Periodic Arrays of Subwavelength Holes," *Phys. Rev. Lett.* **92**, 183901 (2004).
8. M. Babinet, "Memoires d'optique météorologique," *Comptes Rendus de l'Academie des Sciences* **4**, 638-648 (1837).
9. R. W. Wood, "Anomalous Diffraction Gratings," *Phys. Rev.* **48**, 928-936 (1935).

10. J. B. Pendry, L. Martin-Moreno, and F. J. Garcia-Vidal, "Mimicking Surface Plasmons with Structured Surfaces," *Science* **305**, 847-848 (2004).
11. C. R. Williams, S. R. Andrews, S. A. Maier, A. I. Fernandez-Dominguez, L. Martin-Moreno, and F. J. Garcia-Vidal, "Highly confined guiding of terahertz surface plasmon polaritons on structured metal surfaces," *Nature Photonics* **2**, 175 (2008).
12. N. Liu, H. Liu, S. Zhu, and H. Giessen, "Stereometamaterials," *Nature Photonics* **3**, 157-162 (2009).
13. F.J. Gracia de Abajo, "Light scattering by particle and hole arrays," *Rev. of Mod. Phys.* **79**, 1267 (2007).
14. D.W. Porterfield, J.L. Hesler, R. Densing, E.R. Mueller, T.W. Crowe, R.M. Weikle, "Resonant metal-mesh bandpass filters for the far infrared," *Appl. Opt.* **33**, 6046 (1994).
15. Paul, C. Imhof, B. Reinhard, R. Zengele and R. Beigang, "Negative index bulk metamaterial at terahertz frequencies," *Opt. Express* **16**, 6736 (2008).
16. S.L. Dexheimer, *Terahertz spectroscopy: Principles and Applications*, (CRC Press, Boca Raton, London, New York), p.319 (2007).
17. Zhongxiang Zhang, Kam Tai Chan, Yanxia Cui, Sailing He, Changlei Wang, Qirong Xing, and Qingyue Wang, "Multimode transmission in complementary plasmonic structures at terahertz frequencies," *Appl. Phys. Lett.* **96**, 073506 (2010).
18. Masanobu Iwanaga, "Polarization-selective transmission in stacked

-
- two-dimensional complementary plasmonic crystal slabs," *Appl. Phys. Lett.* **96**, 083106 (2010).
19. Masanobu Iwanaga, "Subwavelength electromagnetic dynamics in stacked complementary plasmonic crystal slabs," *Opt. Express* **18**, 15389-15398 (2010).
20. Lewis B. Whitbourn and Richard C. Compton, "Equivalent-circuit formulas for metal grid reflectors at a dielectric boundary," *Appl. Opt.* **24**, 217-220 (1985).
21. Karl D. Moller, Oren Sternberg, Haim Grebel, and Kenneth P. Stewart, "Inductive cross-shaped metal meshes and dielectrics," *Appl. Opt.* **19**, 3919-3926 (2002).

Chapter 4: Plasmon waveguide and cavity

4.1 Introduction to plasmon waveguide

In chapter two, we have discussed the basics of surface plasmon and in chapter three, planar devices based on surface plasmons have been proposed and demonstrated. The motivation for this kind of study is to control the propagation of the electromagnetic wave. Based on this purpose and motivated by integration of photonics and electronics, we continue the discussion to control the propagation of the surface wave in the context of waveguiding structure. Based on the waveguide designs, plasmon cavity is investigated.

There are three basic models which are shown by Fig. 4-1 for plasmon waveguide: metal-dielectric interface supporting SPP (Fig. 4-1(a)), insulator-metal-insulator (IMI) structure supporting long-ranged SPP (Fig. 4-1(b)) and metal-insulator-metal (MIM) structure supporting gap plasmon (Fig. 4-1(c)). For the first case, we have detailed discussion in chapter two. In this chapter, we will focus in the waveguiding related to MIM and IMI structures.

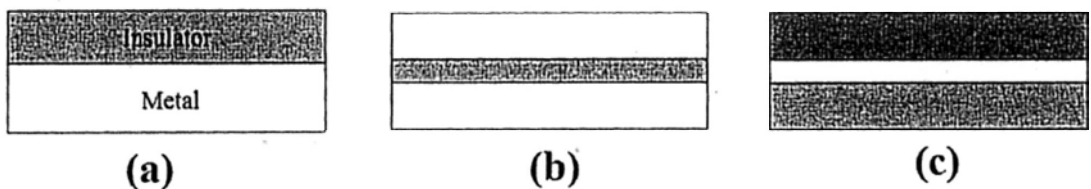


Fig. 4-1 Basic surface plasmon models: (a) metal-insulator interface; (b) MIM structure; (c) IMI structure.

In order to achieve that goal of integration of photonic and electronics, plasmonic waveguides are indispensable. Initial studies of SPPs on metal films [1,

2] have stimulated the search for methods of transmitting SPPs in tiny waveguides such as metallic nanowires [3], SPP band gap structures [4] and nano-particle chain arrays [5]. The most common plasmonic waveguide is the metal stripe waveguide, an appropriate design of which can yield a long-range SPP (LRSPP) waveguide whose loss is as low as 6-8dB/cm [6]. Unfortunately, the LRSPP waveguide has poor confinement just like the dielectric waveguide at a similar dimension. To produce better confinement, a hybrid plasmonic waveguide consisting of a dielectric wire placed close to a metal surface was demonstrated [7]. The hybrid waveguide has been further developed into a plasmon nanolaser [8].

Plasmonic waveguiding actually is achieved by modifying the dispersion in the structure to get a good confinement or low-loss propagation. In section 4.2, the dispersion of gap plasmon and nano wire will be discussed. And in section 4.3, the dispersion of MIM structure will be presented combined with the construction of surface plasmon cavity to demonstrate fascinating applications such as biosensors.

4.2 Plasmonic waveguiding in a hexagonally ordered metal wire array

In the fiber regime, the research on photonic crystal fiber (PCF) has been extensively investigated in the past two decades [9]. The technique of fabricating variable fibers with different cross-section structure has been well developed. Fig. 4-2 shows the schematic of fiber drawing in high-temperature furnace. A stack of glass tubes and rods is constructed as the any required photonic crystal arrangements. This stack-and-draw procedure proved highly versatile, allowing

complex lattices to be assembled from individual stackable units of the correct size and shape. Solid, empty, or doped glass regions could easily be incorporated.

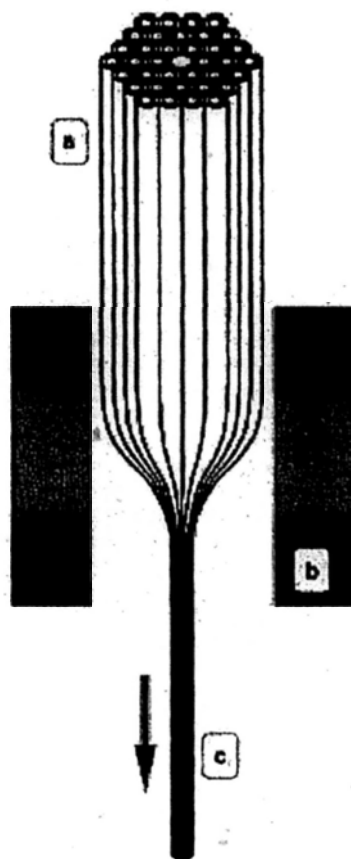


Fig. 4-2 A stack of glass tubes and rods (a) is constructed as a macroscopic “preform” with the required photonic crystal structure. It is then fused together and drawn down to fiber (c) in two stages using a standard fiber drawing tower.

To soften the silica glass, the furnace (b) runs at 1800° to 2000°C [9].

When the holes in photonic crystal fibers (PCFs) are replaced by metal wires, metallic mode confinement [10] and highly polarization- and wavelength-dependent transmission [11] are obtained. Furthermore, tapering PCFs [12] and direct fiber drawing [13] can result in nano-scale structured fibers. Here we propose such a nano-scale fiber with embedded metal wires and show by

simulation that a hybridization of the gap plasmon mode and the single-wire SPP mode can produce a low-loss plasmonic waveguide mode. Our approach demonstrates how complex plasmonic structures can be realized by versatile fiber technology to achieve a good balance between confinement and loss.

4.2.1 Metal wire array in fiber

The proposed nano-scale PCF is shown in Fig. 4-3 which can be fabricated by mature fiber processing technology. Fig. 4-3(a) and (b) show the 3-dimensional and 2-dimensional schematic of our proposed waveguide, respectively. Six metallic wires are embedded into the silica fiber and arranged in a hexagonal pattern. The parameter s is the separation of two adjacent metal wires and d is the diameter of each individual metal wire.

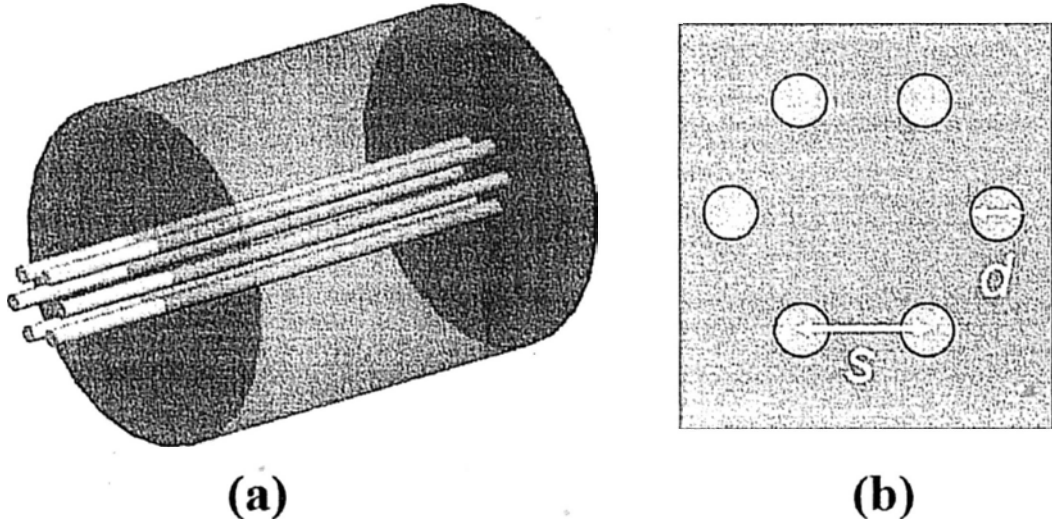


Fig. 4-3 (a) 3-dimensional schematic of the metal wire array in fiber; (b) Cross section of the hexagonally ordered wires.

The hybrid-wave modal profiles in the metallic waveguide are computed by the finite element method (FEM) assuming eigen modes at our selected wavelength and

the result is shown by Fig. 4-4. We select gold as the metal in our fiber, whose permittivity is $-104+3.68i$ according to Drude model [14] at the standard 1550nm telecommunication wavelength and the refractive index of silica is 1.467. The diameter of the fiber is fixed at $2\mu\text{m}$ and the separation s of adjacent wires is set at 200nm unless otherwise stated.

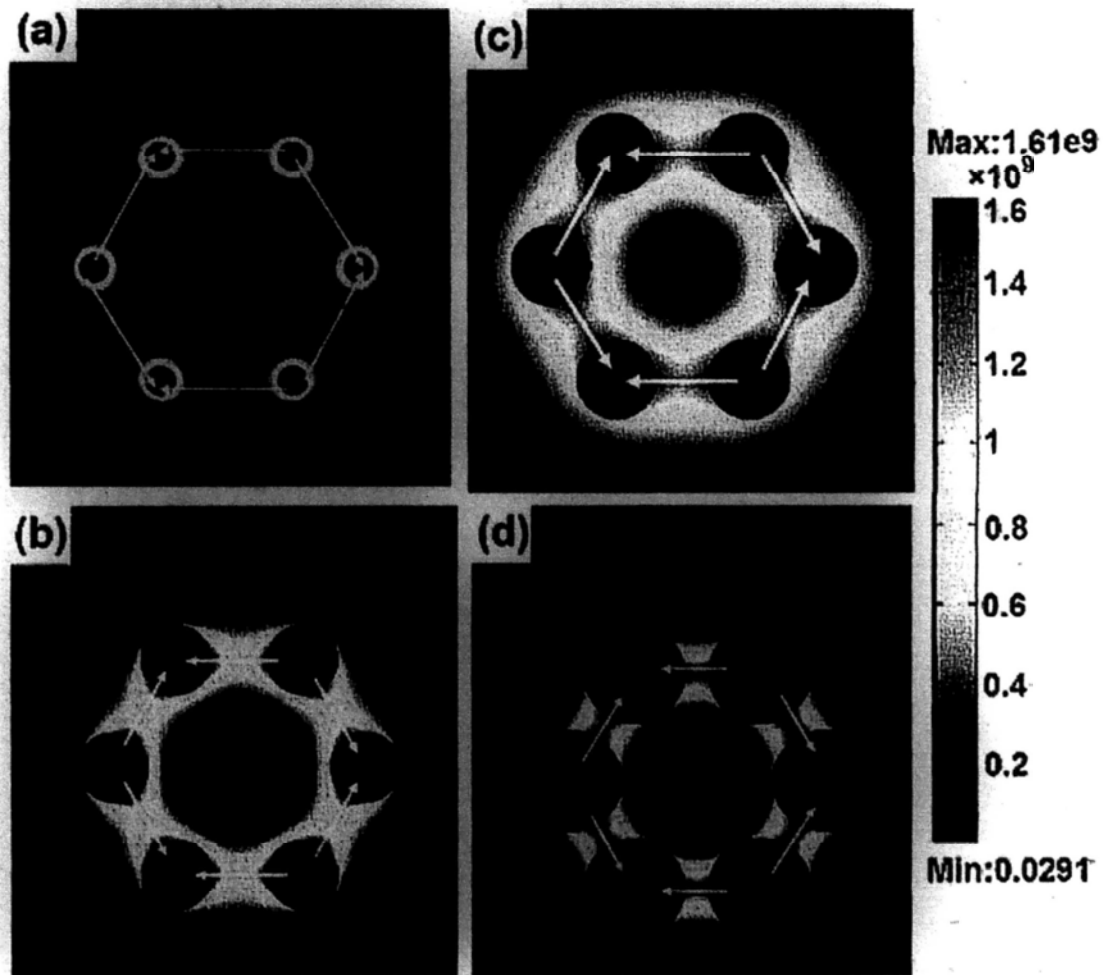


Fig. 4-4 Calculated modal profiles are shown for: (a) $d=40\text{nm}$; (b) $d=110\text{nm}$; (c) $d=130\text{nm}$; (d) $d=160\text{nm}$. And $s=200\text{nm}$. The white arrows in (a)-(d) represent the orientation of the electric field.

Fig. 4-4 shows the absolute intensity distribution and direction of the electric field of the lowest-order eigen mode in the structure under different values of d while keeping s constant. When $d=40\text{nm}$, as shown in Fig. 4-4(a), the metal wires are separated far away from one another and a mode very similar to the single-wire mode dominates the field distribution because the interaction between the wires is very weak. When d is increased to 110nm and 130nm , as shown in Fig. 4-4(b) and (c), the electric field in the region between the wires becomes larger while the field pertaining to the single-wire mode also exists. As such, the electric field distribution tends to form a continuous ring. When d reaches 160nm [Fig. 4-4(d)], where the gap between the metal wires is only 40nm , the electric field becomes strongly confined in the dielectric between adjacent wires, thereby forming a predominantly metal-insulator-metal (MIM) waveguide mode called “gap plasmon” in each gap between adjacent wires. The modes described in Fig. 4-4 are a result of the different degrees of hybridization between the single-wire mode and the gap plasmon mode, and they are sensitive to the symmetry of the structure. In fact, such hybridization has been clearly observed in nanowire arrays [15] and the symmetry properties and energy splitting associated have been addressed [16].

4.2.2 Propagation and dispersion

The surface plasmon polariton modes within the waveguide has been studied by varying the wire diameter and wire spacing. In this section, simulation results show that hybridization of the single-wire mode and the gap plasmon mode can yield a hybrid mode with optimum propagation lengths comparable to those

reported for other structures but with better light confinement.

Fig. 4-5(a) shows the real and imaginary parts of the effective mode index versus the diameter of the metallic wire. The real part of the effective mode index is defined as

$$\text{Re}[n_{eff}] = \beta / k_0 \quad (4.1)$$

where β is the in-plane wave vector of the SPP and k_0 is the free space wave vector. The imaginary part of the effective mode index defines the propagation length, L , of the SPP mode by

$$\text{Im}(n_{eff}) = \lambda / [4\pi L] \quad (4.2)$$

From Fig. 4-5(a), it is observed that when the diameter increases, both the real part and imaginary part of the effective mode index follow a U-shaped curve. The longest propagation length is obtained around $d=130\text{nm}$.

When the diameter of the wire is large, the gap plasmon mode dominates. When the gap plasmon mode dominates, the dispersion of the waveguide follows the dispersion curve of gap plasmons. From the MIM model, the dispersion relation is described by [17, 18]

$$\tanh[k_2(200\text{nm} - d)/2] = -\frac{k_1\epsilon_2}{k_2\epsilon_1} \quad (4.3a)$$

$$\tanh[k_2(200\text{nm} - d)/2] = -\frac{k_2\epsilon_1}{k_1\epsilon_2} \quad (4.3b)$$

where equation (4.3a) refers to the odd mode and (4.3b) refers to the even mode.

Here k_i ($i=1,2$) is the propagation constant inside ($i=1$) and outside ($i=2$) the metal with the relationship

$$k_i^2 = \beta^2 - k_0^2 \varepsilon_i, \quad (i = 1, 2) \quad (4.4)$$

where ε_1 and ε_2 are the permittivity of the metal and dielectric, respectively. In our proposed design, multiple modes are supported because of the interaction of the wire array. But for each mode at a given frequency, the propagating constant β is inversely proportional to the gap width. The behavior of the real part of the mode index in the region of $d > 130\text{nm}$ in Fig. 4-5(a) does reflect this relationship. For small wire diameters, the interaction between the wires becomes weak so that the dispersion relation of the waveguide follows that of the single wire. For a single wire, the dispersion relation is given by [19]

$$\frac{k_2 I_1(k_1 d / 2) K_0(k_2 d / 2)}{k_1 I_0(k_1 d / 2) K_1(k_2 d / 2)} = -\frac{\varepsilon_2}{\varepsilon_1} \quad (4.5)$$

where I_i, K_i are the i th-order modified Bessel functions and d is the diameter of the wire. Here we do not have an analytical expression between the wire diameter and the effective mode index. But numerical computation (not shown here) shows that the effective mode index decreases with an increase of the wire diameter, which is also reflected in the same figure when d is less than about 80nm. Regarding the imaginary part of the mode index, which is directly proportional to the loss, Fig. 4-5(a) shows that the loss is high when the gap distance is very narrow. This can be explained by the tight confinement of the electric field between the metal wires, which increases the relative field intensity inside the metal on both sides of the gap, thus causing a huge metal loss. On the other hand, when the wire diameter is so small that there is negligible interaction between adjacent wires, the loss is also high

because of the intrinsic lossy nature of very small single-wire waveguides. For intermediate values of d around 100nm, where a significant part of the electric field is in the dielectric and the field intensity on the metal surface is smaller than those in the previous two cases, the loss becomes much smaller. To characterize the waveguide, a figure of merit (FOM), F , which is defined as the ratio between the real and imaginary parts of the effective mode index, is computed and shown in the inset. A larger FOM means that the waveguide possesses a higher Q-factor, which is desirable for resonator applications. A maximum F value of 192 is achieved when $d=140\text{nm}$.

To help optimize the design of less lossy waveguides, the variation of propagation length versus the wire diameter at different wire separations is computed and shown in Fig. 4-5(b). For comparison, the propagation length of the single-wire waveguide is also calculated and shown. One obvious conclusion is that the introduction of wire interaction always causes an additional loss. Maximum propagation lengths of $12.1\mu\text{m}$, $19.8\mu\text{m}$ and $27.2\mu\text{m}$ are obtained when $s=200\text{nm}$, 300nm and 400nm , respectively. These values are comparable to those of some stripe waveguides or dielectric-loaded waveguides [20]. Despite their shorter propagation lengths when compared with the single-wire waveguide of the same wire diameter, our proposed waveguides exhibit better light confinement because a significant part of the electric field resides in the dielectric between adjacent wires. Therefore this structure may be more realistic than the single-wire waveguide, especially when gain is inserted into the dielectric.

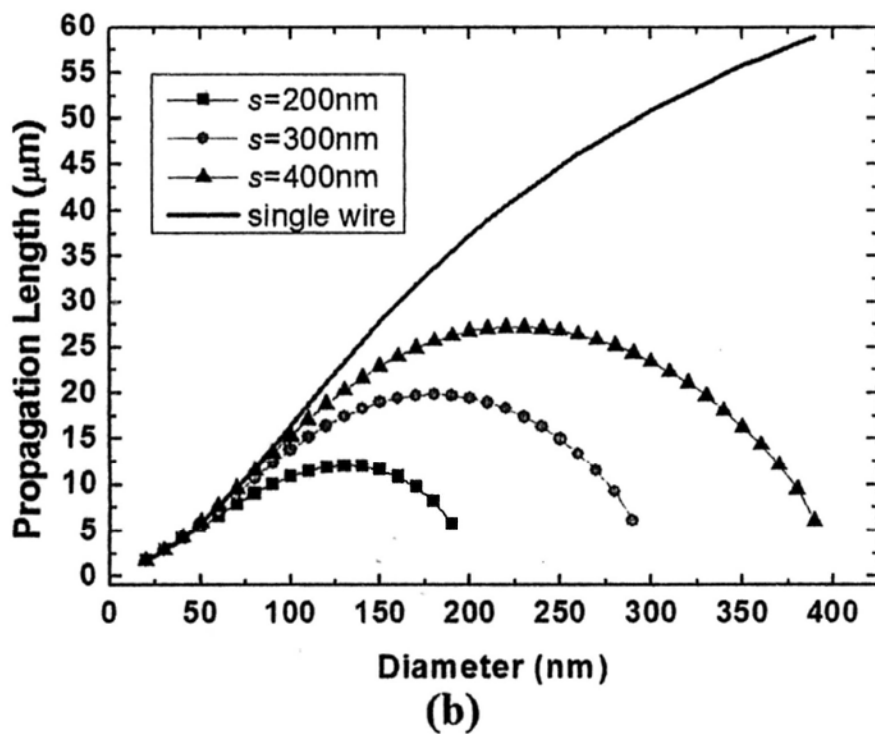
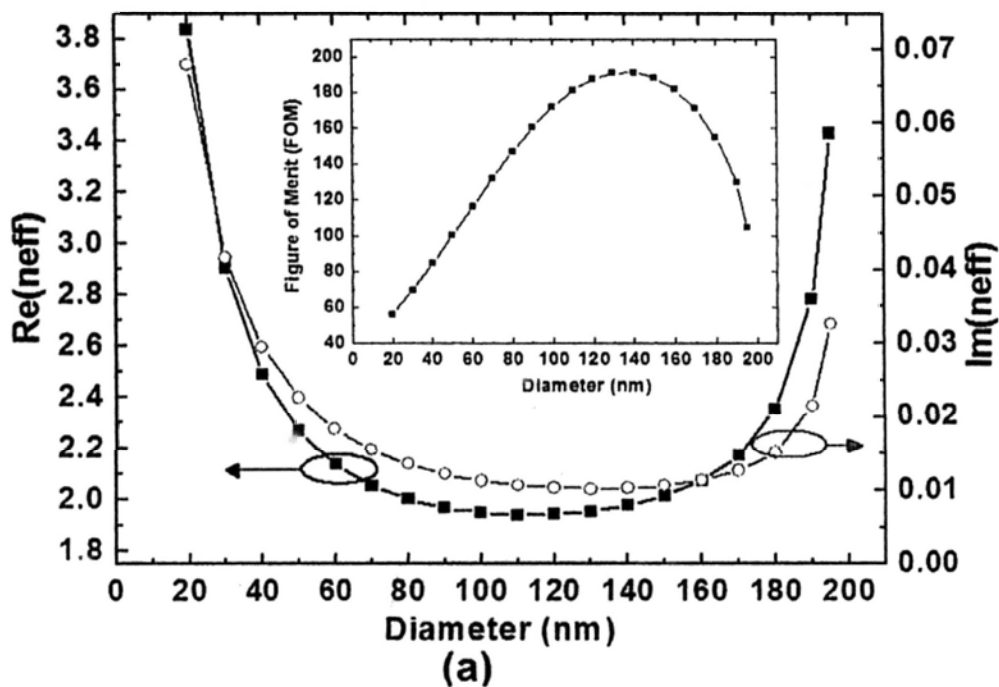


Fig. 4-5 (a) The real and imaginary parts of the effective mode index versus the diameter of the metallic wire. Inset: FOM versus the diameter d . (b) Calculated propagation length versus the diameter of the metal wire for the separation $s=200\text{nm}$, 300nm , 400nm and the single wire.

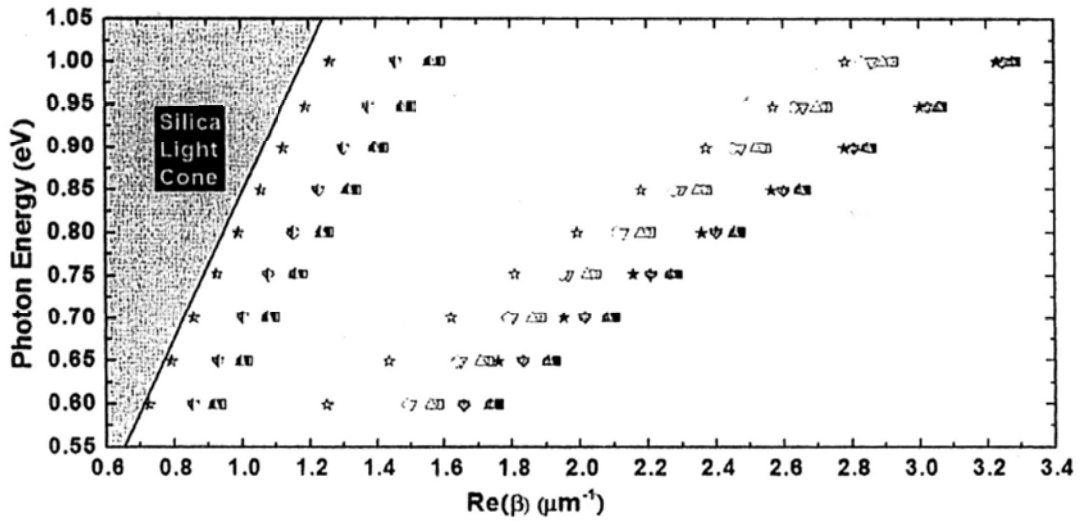


Fig. 4-6. The dispersion relations of the waveguide modes for $d = 20\text{nm}$ (wire modes $\blacksquare \bullet \blacktriangle \blacklozenge \star$), 130nm (hybrid modes $\blacksquare \bullet \blacktriangle \blacklozenge \star$) and 195nm (gap modes $\square \circ \triangle \nabla \diamond \star$). The grey region is the silica light cone.

The dispersion relations of the first six modes of the waveguide are next computed and shown in Fig. 4-6 for $d=20\text{nm}$, 130nm and 195nm . Some modes are degenerate in all of the three cases. Clearly, the k -vectors for the wire modes and gap modes are large, confirming their dominant SPP nature. But the k -vectors for the hybrid modes at $d=130\text{nm}$ are smaller. In fact, their curves are quite close to the light line of silica, thereby further illustrating their larger composition of dielectric guiding.

The modal polarization is actually an important issue in complex structures as the reviewer rightly mentioned. For the fundamental mode shown in Fig. 4-4, we have marked the direction of the electric field to make the modal profiles clearer. Fig. 4-7 shows the directions of the electric field for 4 other modes with different effective mode indices. Here we would like to emphasize the hybridization of the

single-wire mode and the gap plasmon mode and the loss of this hybridized mode.

We shall investigate more fully the polarization effect in our further studies.

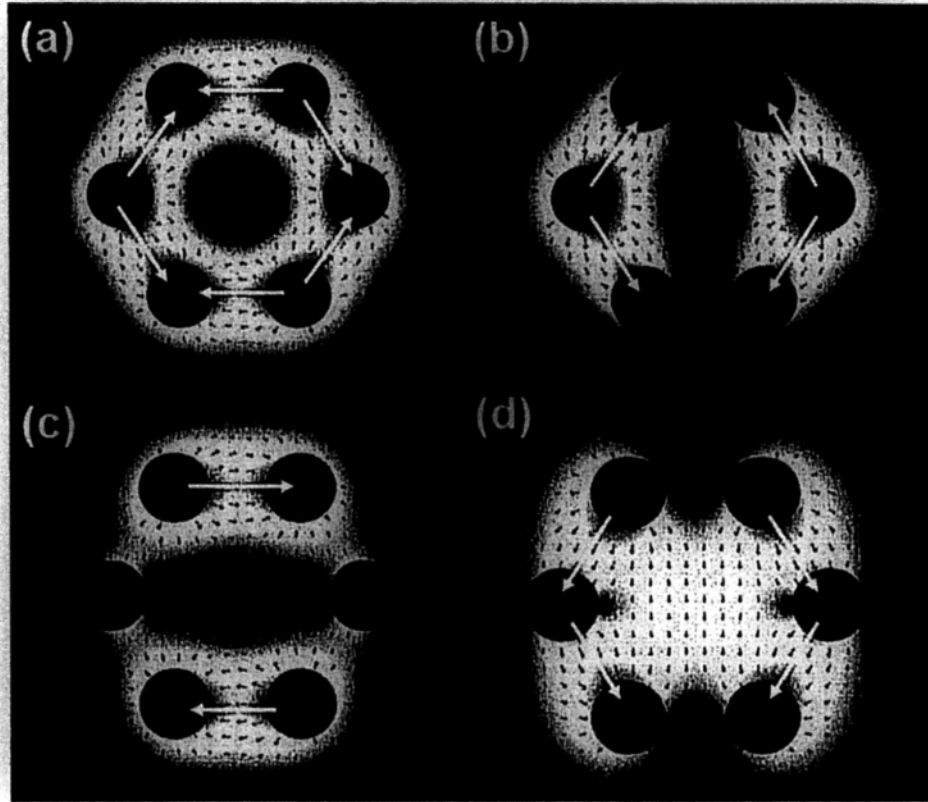


Fig. 4-7 Higher order modal profiles for $d=130\text{nm}$ and $s=200\text{nm}$ with different mode index.

To show whether the modal response in our cases where the wires are closely packed is the effect of the coupling of modes on the individual wires or the response of the entire nanowire structure due to the symmetries inherent in a hexagonal distribution, a study on the broken of the symmetry is necessary. The symmetry issue has been studied in our proposed structure. We found that both the structure symmetry and hybridization between individual single-wire modes and gap plasmon modes are necessary to produce the results shown in Fig. 4-4 of the revised manuscript. If the wires are randomly distributed, only the smallest gap

may show a mode owing to the coupling between the two wires as shown in Fig. 4-8(a) in below. When the 6-fold rotational symmetry is broken by taking out the wires one by one, the resulting modes will be quite different from what is shown in Fig. 4-4 as shown in Fig. 4-8(b) to (f) in below. The simulation shows that the hybridization property happens for single pair of nano wires and the cross-talk effect do not greatly affect the modal profile.

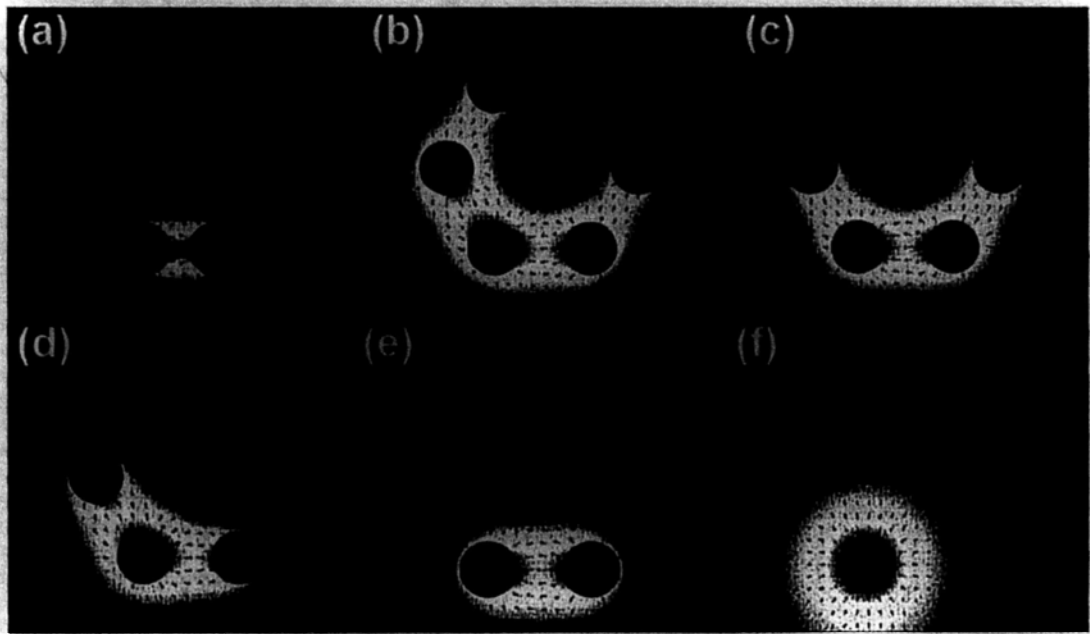


Fig. 4-8 Broken of symmetry. (a) Random distributed nano wires; (b-f) 6-fold rotational symmetry is broken by taking out the wires one by one.

In summary, we have proposed a nano-scaled symmetric fiber plasmonic waveguide incorporating metal nanowires. Various propagation modes are analyzed and the hybrid modes are found to exhibit the longest propagation length. The proposed waveguide should make integration with nano-scale integrated circuits easier to implement. Although the propagation length of this waveguide is limited, its better light confinement property than the single-wire plasmonic waveguide

makes it more practicable to use, especially when the dielectric is doped with a gain material, such as erbium, to enhance the light propagation distance or to turn it into a nanolaser.

4.3 Plasmonic cavity

The study on microcavity has become a distinct subject of research in the past two decades. The physical demonstration and actual devices have been well investigated. Some designs have been commercialize such as vertical cavity surface emitting lasers (VCSEL). The basic structures include Fabry-Perot cavity, whispering gallery cavity and photonic crystal cavity et al. The ultra high Q factor up to $\sim 10^9$ has been obtained in whispering gallery cavity. Fig. 4-9 shows different types of cavities and the corresponding Q factor and mode volume [21].



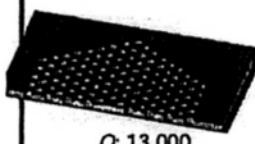
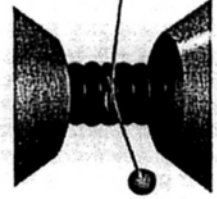
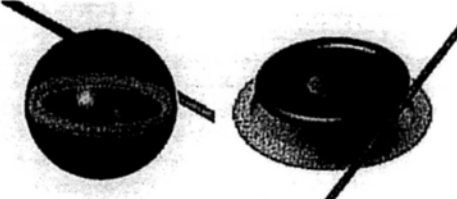
	Fabry-Perot	Whispering gallery	Photonic crystal
High Q	 <p>Q: 2,000 V: $5 (\lambda/n)^3$</p>	 <p>Q: 12,000 V: $6 (\lambda/n)^3$</p> <p>Q_{III-V}: 7,000 Q_{Poly}: 1.3×10^5</p>	 <p>Q: 13,000 V: $1.2 (\lambda/n)^3$</p>
Ultra-high Q	 <p>F: 4.8×10^5 V: $1,690 \mu\text{m}^3$</p>	 <p>Q: 8×10^9 V: $3,000 \mu\text{m}^3$</p> <p>Q: 10^8</p>	

Fig. 4-9 Different optical microcavities with different Qs and Vs, depending on the confinement methods.

With the ultrahigh Q-factor, the samples are sampled many times compared to

the one-time sampling in the optical waveguide sensors. For example, for a Fabry-Perot cavity with mirror reflectivity of R , then the effective number of passes equals to $1/(1-R)$. An effective pathlength of nearly 100km has been realized with a physical cell only 1m in length using a diode laser coupled into a cavity formed by mirrors with a reflectivity of 99.999% [22]. Building on the high sensitivity that cavities bring to the biosensors, optical waveguides can take advantage of evanescent wave to sample complex mixtures with minimal background contributions.

4.3.1 Plasmonic ring cavity based on long-ranged plasmon waveguide

Based on the plasmon waveguides, plasmonic cavity would be an attractive for its low-dissipation, fast modulation speed. Recently, research on plasmonic cavity has become popular [23-25]. But still, the properties of the resonant modes in plasmonic cavity are still a very hot topic for research and lots of exciting unknown are to be discovered. Fig. 4-10 give out an example of whispering gallery mode (WGM) in the microtoroid.

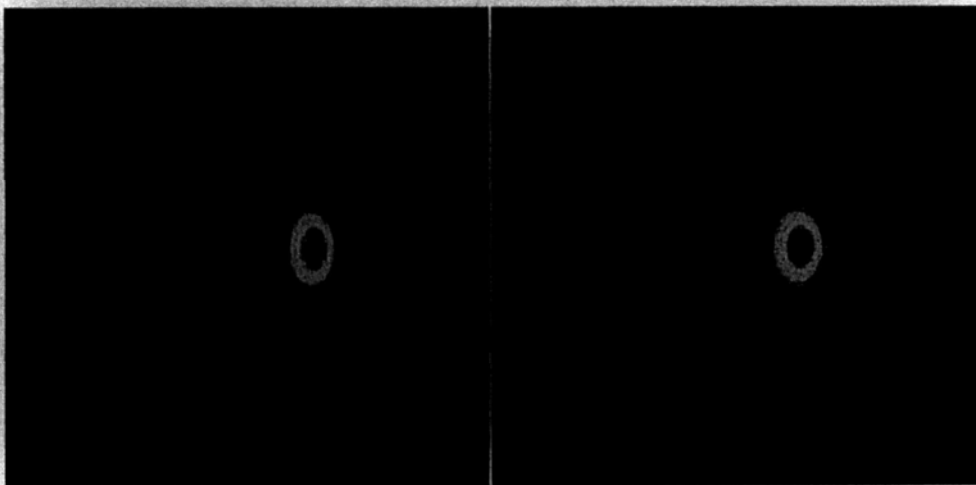


Fig. 4-10 WGM in microtoroid dielectric cavity.

To have a proof-of-concept examination of the plasmonic cavity, we do a simulation at infrared range selecting 1.5 μm as the observation wavelength. Fig. 4-11 shows two modes at this wavelength. The left one has higher mode index but also higher loss than the right one in Fig. 4-11. The mode on left-hand size is just the antisymmetric mode in long-ranged SPP waveguide. For some applications, for example plasmonic biosensor, we prefer the mode on right-hand size with higher Q factor.

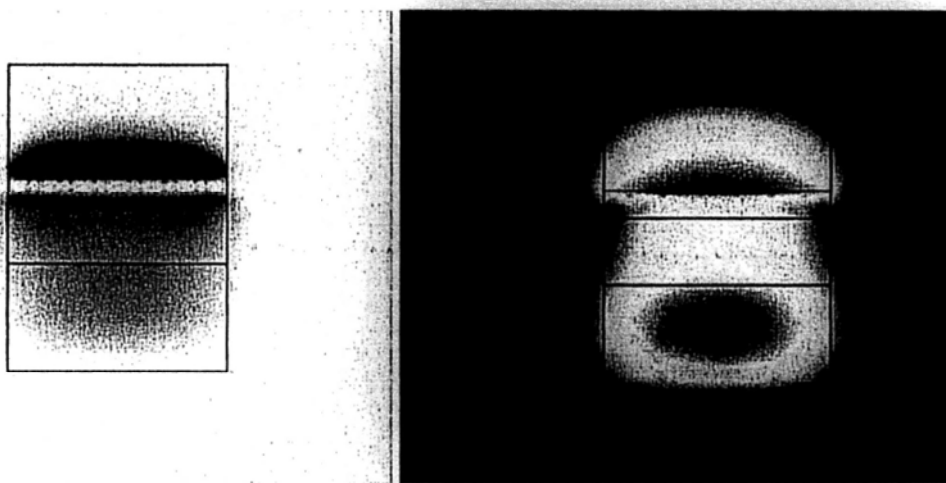


Fig. 4-11 Photonic and plasmonic coupled modes in plasmonic WGM cavity.

4.3.2 Biosensor based on plasmonic cavity

At present, lots of optical methods have been developed to create biosensors, including evanescent wave fiber optic biosensor, planar waveguide biosensor, flow immunosensors, SPR biosensors, plasmonic surface-enhanced Raman scattering (SERS) biosensors and so on. Each of them has advantage and limitations. For the recent SPR biosensors, it exhibits similar fundamental advantages and limitations with other kinds of thin film refractometry-based sensors such as the grating coupler [26], integrated optical interferometer [27]. All of them measure the refractive

index changes produced by the biomolecular interactions occurring at the surface of the sensor. One advantage of the approach is the ability to detect the molecular interactions in “real time”, which means that no radioactive or fluorescent labels are needed. Another advantage for the approach is that it provides a versatile platform for the detection of different types of analytes or interactions since it do not have to observe the fluorescence or absorption and scattering spectrum. In the field of biophysical analysis of biomolecular interactions, SPR sensor allow for monitoring of both weak and strong interactions (equilibrium constant K_D ranging from 1mM to 1pM) and typically require less material and have higher throughput. The main challenge for the SPR sensor is in the specificity of detection. It based on the ability of biomolecular recognition coating to recognize and capture target analyte molecules. Any changes in the refractive index of the samples will cause a false response. This problem would be serious when the SPR sensors are used to analyze crude samples in the out-of-lab environments [28].

To solve the problems and improve the performance of SPR biosensor, several methods have been proposed and demonstrated. One is the SPR phase measurement [29], which measures the change of phase instead of amplitude. The phase-modulated SPR sensors lead to high-sensitivity biosensors but it requires a rather bulky and complex instrument requiring and sophisticated data processing. Another interesting technique which has been developed to enhance the sensitivity and resolution of SPR biosensor is based on the exploitation of long-range surface plasmon (LRSP) [30, 31], which exhibit lower dispersion than classical surface

plasmon wave. Besides yielding enhanced sensitivity, LRSP produces very narrow angular or spectral dips more than 10-fold narrower than those produced by conventional surface plasmons, which lower the sensor resolution down to the low 10^{-8} RIU (refractive index unit). Referencing approaches are being investigated for improving the robustness and specificity of SPR biosensors. The compensation was demonstrated by combining an SPR sensor with angular modulation with a critical angle refractometer [32] or by multiple-surface-plasmon spectroscopy [33].

Advances in the development of new SPR biosensor hardware is driven by the needs of the applications. Thus, in this proposal, we plan to take our effort to demonstrate a conceptual new and practical approach to improve the performance of SPR biosensors. Our approach based on the micro- or nano-fabrication technique to form the surface plasmon resonator and the devices can be large-scale integrated. At the same time, most of the improvement techniques in traditional SPR biosensors such as phase measurement, LRSP and referencing channel, can be easily applied to our design by traditional on-chip integral devices.

SPR biosensors are optical devices that exploit the sensitivity of the propagation constant of the surface plasmons to the refractive index to measure changes in the refractive index or changes in other quantities that can produce changes in the refractive index [34]. Generally, two schemes can be applied to excite the surface waves in SPR sensors. One is Kretschmann configuration and another one is Otto configuration, shown by Fig. 4-12(a) and (b), respectively. Both surface waves in these two configurations are excited by the total internal reflection method. The

evanescent waves penetrating the metal (Kretschmann configuration) or dielectric (Otto configuration) are generated when the light wave pass the prism with total internal reflection.

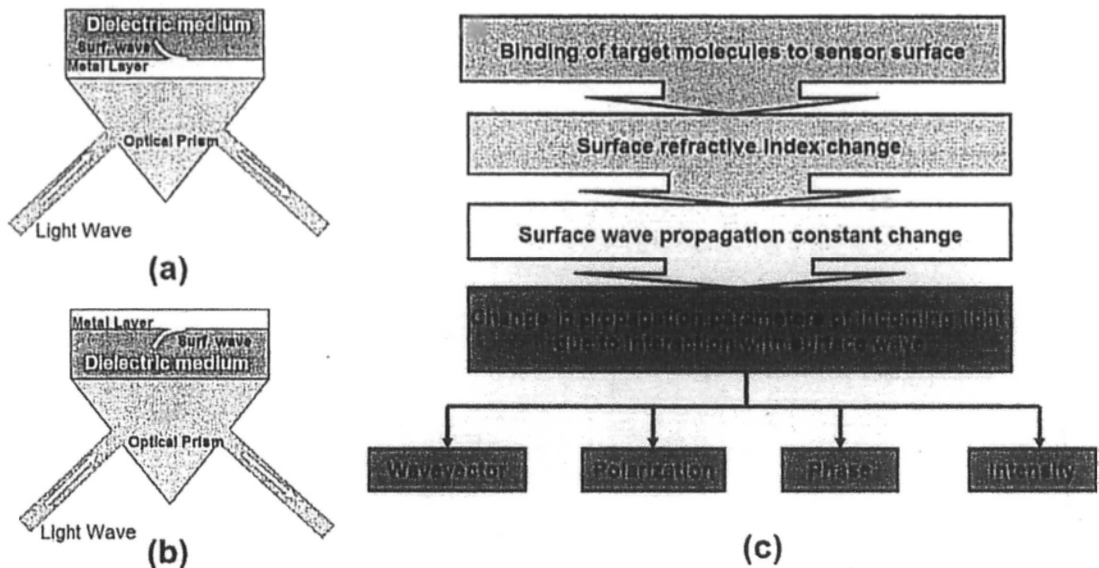


Fig. 4-12 Excitation of surface plasmon on smooth metal surfaces by (a) Kretschmann configuration and (b) Otto configuration. (c) Surface plasmon resonance biosensor: principle of operation.

Until now, most SPR biosensors can get the refractive index resolution in low 10^{-7} RIU range, which is sufficient for a wide range of analytes. The principle of operation for the SPR biosensor is shown by Fig. 4-12(c) as a flow chart. Any phenomenon that gives rise to a change in the refractive index at the surface of the metal can be observed and quantified by the means of an SPR sensor. SPR biosensors are sensing devices that incorporate biomolecules, which recognize and are able to interact with selected analytes. These biomolecular recognition elements are immobilized on the SPR sensor surface. When a solution containing analyte

molecules is brought into contact with the SPR sensor, analyte molecules in solution bind to the recognition elements on the sensor surface, producing an increase in the refractive index at the surface. This change results in a change in the propagation constant of the surface wave and is determined by measuring the change in the characteristics of the reflected wave including the wavevector, phase, intensity or polarization. Each of them corresponds to some type of sensing scheme.

Sum those above, we could develop a new method using the plasmonic cavities to demonstrate biosensors with high performance. The integrated cavity and waveguide can make the sensor compact and most of the improvements of the biosensor in free-space setup can be introduced in our design by integrated components in our devices. Fig. 4-13 shows the proposed plasmonic cavity device and the schematic of the experimental system. The proposed biosensor consists of traditional waveguide with a dielectric cavity for light coupling, the plasmonic cavity and the microfluidic channels (not shown in the figure). The light source can be a broadband light source or a laser, depending on the design of the device we finally select. An embedded waveguide couple the light wave into the device and then couple to a dielectric ring cavity. On this dielectric cavity, a thin metal film with ring pattern is deposited. The film is thin then the metallic ring is actually a plasmonic cavity formed by long-range plasmon waveguide which has an Insulator-Metal-Insulator (IMI) structure. As our expectation, the LRSP waveguide is suitable for our application for its long propagation length and have good

performance as refractive index sensor [35, 36] Both waveguide modes (red arrows in Fig. 4-13(a)) and surface plasmon modes (blue arrow in Fig. 4-13(a)) propagate in the ring cavity. Optimal design can suppress the waveguide mode in the cavity and enhance the surface plasmon modes. To reach this goal, we still have lots of job to do. When the gain medium such as Erbium doped silicon dioxide, some other kinds of waveguides to demonstrate the resonance are possible.

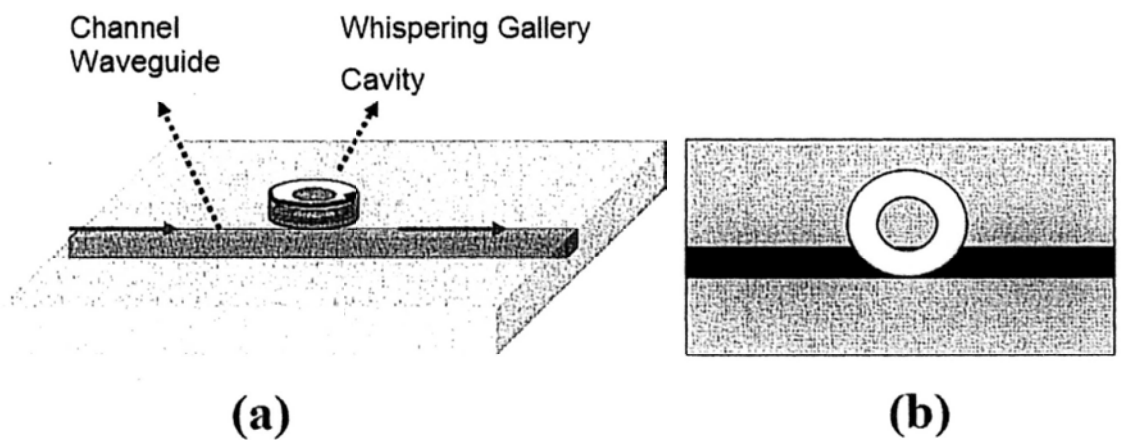


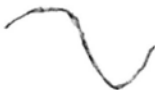
Fig. 4-13 (a) 3-D and (b) top view of the SPR sensor element.

4.4 Summary

The inclusion of a structured pattern of nano-scale metal wires in a silica fiber to form a symmetric plasmonic waveguide is proposed. The surface plasmon polariton modes within the waveguide are studied by varying the wire diameter and wire spacing. Simulation results show that hybridization of the single-wire mode and the gap plasmon mode can yield a hybrid mode with optimum propagation lengths comparable to those reported for other structures but with better light confinement. The fiber can be easily doped with a gain material to offset the loss so that the resultant waveguide will be useful for integration with electronic circuits at

nanometer dimensions.

Based on the study of plasmonic waveguide and some proof-of-concept simulation results, we propose a WGM-cavity-based biosensor scheme. We plan to study how to rightly select a plasmon waveguide and optimize the coupling mechanism between the target molecule and the optical field to make the biosensor sensitivity and robust. Here we propose a method by using the plasmon waveguide and plasmonic cavity which might pave a new way to get a good label-free biosensor. The proposed method maintains advantages of SPR biosensor and potentially highly improve the sensitivity, integration and robustness than lead to an optimal solution for the SPR biosensor.



References

1. H. Raether, "Surface Plasmons on Smooth and Rough Surfaces and on Gratings," (Springer-Verlag, 1986).
2. H. Raether, "Solid state excitations by electrons Plasma oscillations and single electron transitions," Tracts in modern physics (Springer-Verlag, Berlin) **38**, 84-157 (1965).
3. J.C. Weeber, A. Dereux, C. Girard, J.R. Krenn and J.P. Goudonnet, "Plasmon polaritons of metallic nanowires for controlling submicron propagation of light," Phys. Rev. B **60**, 9061-9068 (1999).
4. C. Marquart, S.I. Bozhevolnyi and K. Leosson, "Near-field imaging of surface plasmon-polariton guiding in band gap structures at telecom wavelengths," Opt. Express **13**, 3303-3309 (2005).
5. M.L. Brongersma, J.W. Hartman and H.A. Atwater, "Electromagnetic energy transfer and switching in nanoparticle chain arrays below the diffraction limit," Phys. Rev. B **62**, R16356-R16359 (2000).
6. T. Nikolajsen, K. Leosson, I. Salakhutdinov and S.I. Bozhevolnyi, "Polymer-based surface-plasmon-polariton stripe waveguides at telecommunication wavelengths," Appl. Phys. Lett. **82**, 668-670 (2003).
7. R.F. Oulton, V.J. Sorger, D.A. Genov, D.F.P. Pile and X. Zhang, "A hybrid plasmonic waveguide for subwavelength confinement and long-range propagation," Nature Photonics **2**, 496-500 (2008).
8. R.F. Oulton, V.J. Sorger, T. Zentgraf, R.M. Ma, C. Gladden, L. Dai, G. Bartal

- and X. Zhang, "Plasmon lasers at deep subwavelength scale," *Nature* **461**, 629-632 (2009).
9. Philip Russel, "Photonic crystal fibers," *Science* **299**, 358 (2003).
 10. J. Hou, D. Bird, A. George, S. Maier, B.T. Kuhlmeiy and J.C. Knight, "Metallic mode confinement in microstructured fibres," *Opt. Express* **16**, 5983-5990 (2008).
 11. H.W. Lee, M.A. Schmidt, H.K. Tyagi, L.P. Sempere and P.S.J. Russell, "Polarization-dependent coupling to plasmon modes on submicron gold wire in photonic crystal fiber," *Appl. Phys. Lett.* **93**, 111102 (2008).
 12. E.C. Magi, P. Steinvurzel and B.J. Eggleton, "Tapered photonic crystal fibers," *Opt. Express* **12**, 776-784 (2004).
 13. H.K. Tyagi, H.W. Lee, P. Uebel, M.A. Schmidt, N. Joly, M. Scharrer, and P. St.J. Russell, "Plasmon resonances on gold nanowires directly drawn in a step-index fiber," *Opt. Lett.* **35**, 2573-2575 (2010).
 14. M.A. Ordal, L.L. Long, R.J. Bell, S.E. Bell, R.R. Bell, R.W. Alexander, and C.A. Ward, "Optical properties of the metals Al, Co, Cu, Au, Fe, Pb, Ni, Pd, Pt, Ag, Ti, and W in the infrared and far infrared," *Appl. Opt.* **22**, 1099-1120 (1983).
 15. A. Manjavacas and F.J.G. Abajo, "Robust plasmon waveguides in strongly interacting nanowire arrays," *Nano Lett.* **9**, 1285-1289 (2009).
 16. A. Manjavacas and F.J.G. Abajo, "Coupling of gap plasmons in multi-wire waveguides," *Opt. Express* **17**, 19401-19413 (2009).

17. S.A. Maier, "Plasmonic: Fundamentals and Applications," Springer (New York) (2007).
18. B. Prade, J.Y. Vinet and A. Mysyrowicz, "Guided optical waves in planar heterostructures with negative dielectric constant," *Phys. Rev. B* **44**, 13556-13572 (1991).
19. J. Takahara, S. Yamagishi, H. Taki, A. Morimoto and T. Kobayashi, "Guiding of a one-dimensional optical beam with nanometer diameter," *Opt. Lett.* **22**, 475-477 (1997).
20. Alexey V. Krasavin and Anatoly V. Zayats, "Numerical analysis of long-range surface plasmon polariton modes in nanoscale plasmonic waveguides," *Opt. Lett.* **35**, 2118-2120 (2010).
21. Kerry J. Vahala, "optical microcavities," *Nature* **224**, 839 (2003).
22. John B. Dudek, Peter B. Tarsa, Armando Velasquez, Mark Wladyslawski, Paul Rabinowitz, and Kevin K. Lehmann, "Trace Moisture Detection Using Continuous-Wave Cavity Ring-Down Spectroscopy," *Anal. Chem.* **75**, 4599 (2003).
23. Bumki Min, Eric Ostby, Volker Sorger et al., "High-Q surface-plasmon-polariton whispering-gallery microcavity," *Nature* **457**, 455(2009).
24. Yun-Feng Xiao, Chang-Ling Zou, Bei-Bei Li et al., "High-Q exterior whispering gallery modes in a metal-coated microresonator," *Phy. Rev. Lett.* **105**, 153902 (2010).

25. Yannic Sonnefraud, Niels Verellen, Heidar Sobhani et al., "Experimental realization of subradiant, superradiant, and Fano resonances in ring/disk plasmonic nanocavities," *ACSNano* **4**, 1664 (2010).
26. P.M. Nellen, W. Lukosz, "Integrated optical input grating couplers as chemo- and immunosensors," *Sens. Actuators B* **1**, 592 (1990).
27. R.G. Heideman, R.P.H. Kooyman, J. Greve, "Performance of a highly sensitive optical waveguide Mach-Zehnder interferometer immunosensor," *Sens. Actuators B* **10**, 209 (1993).
28. Raimund J. Ober, E. Sally Ward, "The Choice of Reference Cell in the Analysis of Kinetic Data Using BIAcore," *Anal. Biochem.* **271**, 70 (1999).
29. S. G. Nelson, K. S. Johnston, S. S. Yee, "High sensitivity surface plasmon resonance sensor based on phase detection," *Sens. Actuators B* **35**, 187 (1996).
30. G.G. Nenninger, P. Tobiška, J. Homola, S.S. Yee, "Long-range surface plasmons for high-resolution surface plasmon resonance sensors," *Sens. Actuators B* **74**, 145 (2001).
31. Radan Slavik, Jiri Homola, "Ultra-high resolution long range surface plasmon-based sensor," *Sen. Actuators B* **123**, 10 (2007).
32. Timothy M. Chinowsky, Anita A. Strong and Dwight U. Bartholomew et al., "Improving surface plasmon resonance sensor performance using critical-angle compensation," *Proc. SPIE* **3857**, 104 (1999).
33. Pavel Adam, Jakub Dostálek, Jiří Homola, "Multiple surface plasmon spectroscopy for study of biomolecular systems," *Sen. Actuators B* **113**, 774

(2006).

34. Frances S. Ligler, Chris Rowe Taitt, "Optical biosensors: Today and tomorrow," (2nd) Elsevier B.V. (2008).
35. Ouellet, E., C. Lausted, et al., "Parallel microfluidic surface plasmon resonance imaging arrays." *Lab on a Chip* **10**, 581 (2010).
36. Qiao Min, Chengkun Chen, Pierre Berini, and Reuven Gordon, "Long range surface plasmons on asymmetric suspended thin film structures for biosensing applications," *Opt. Express* **18**, 19009-19019 (2010).

Chapter 5: Active plasmonics

5.1 Introduction

Surface plasmon polariton (SPP) in different structures can be an emerging type of information carrier. To demonstrate more information processing technique, active control of surface plasmon is necessary to get more functional devices. These functional active devices include the active modulator or switch [1], plasmon detector [2], plasmon laser [3-6], plasmon amplifier [7], optical gates and memory elements [8, 9] et al. For active control, it can be demonstrated by utilizing the phase transition of the materials. For example, the phase transition between metal and dielectric of VO_2 with the temperature can be used as the switch component. Some types of semiconductor also can make this due the carrier density variation under different optical pumping. Another type of active component is the gain medium. For example, in near infrared, we can get the gain in GaAs at around 800nm wavelength. And in 1.5um wavelength, we have InGaAs or some rare earth materials like erbium to get the gain. At longer wavelength to mid infrared (mid-IR) to THz range where there is no natural semiconductor has such narrow bandgap, quantum cascade structure provides an approach to get the gain in these frequencies.

Why we need the gain medium? Gain mediums play a very important role in the demonstration of population inversion which results in laser. No matter the

tradition laser or the plasmonic laser, the design approach is “gain medium+cavity”. Then the research of cavity will date back to the design of waveguide, which is highlighted in chapter four. Another important reason, gain medium can compensate the loss in the devices to demonstrate the wave amplifier or loss-free devices. Loss is a very important issue in metal optics which is determined by the properties of the metal, especially in visible or near infrared range. In some other research area like metamaterials or negative refractive index materials, loss is also a fatal problem to be solved.

For surface plasmon, dispersion relation is a key to discuss the propagation properties in different waveguide. Plasmonic provide a powerful approach to manipulate the photon in nanoscale. The deviation of the dispersion curve from the light line shows that surface plasmon waveguide can provide a much larger k -vector than dielectric. But it is a pity that this large k -vector, which means short wavelength, is always associated with high loss. When we design a structure, it actually means a tailor of the dispersion curve to demonstrate a tradeoff between the k -vector and the loss. Then the gain medium in the plasmon waveguide becomes a very interesting research topic attracting many researchers' attention.

In mid-IR and THz range, the flexible design for the spoof surface plasmon structure provides a versatile platform to tailor the dispersion curve. In introduction of plasmon structure in gain medium devices such as quantum cascade laser (QCL) results in a possibility of demonstration of compact devices with rich physics. And the integration of gain medium and plasmon waveguide also results in a real

plasmon laser which is a very good coherent source for the research in surface plasmon.

5.2 Quantum cascade laser in mid-IR and THz range

Quantum cascade laser (QCL) [10, 11] emits in the mid- to far-infrared and terahertz range. The repeated stack of semiconductor multiple quantum well heterostructures provide gain media in this spectrum range. In this part, we give a brief introduction to the QCL and fabrication process of the laser which is related to our design based on spoof surface plasmon.

5.2.1 Introduction

In 1994, the event that Bell lab in U.S. invented the QCL opens a virgin area for the research on semiconductor laser in mid-IR range. The laser differs in fundamental way from diode laser has been demonstrated. It is based on intersubband transition. In the spectrum, mid-IR with wavelength of 3-5 μm and 8-14 μm is a very important atmosphere window. The laser in this range is very important for national security applications. But the development of semiconductor laser in this region is very slow. Before 1970s, all the design for lasing in mid-IR is based on the recombination of electrons in conduction band and holes in valence band. Then the lasing wavelength is defined by the bandgap of the semiconductor. The lack of natural semiconductor in mid-IR makes the development slow. In 1971, the scientist Kazatinov and Suris in Soviet Russia proposed amplification by means of stimulated emission of electrons between quantized subbands in two-dimensional quantum wells [12]. This concept was developed by the scientist in Bell lab. In

1986, Dr. Capasso proposed the sequential resonant tunneling in multi quantum well lattice. But scientists gradually recognized that the population inversion above the optical phonon energy (36meV) is difficult to be demonstrated due to the carrier life time is in nano second scale which is much higher than that of phonon (pico second). To overcome this problem, the scientists in Bell lab successfully invented the first quantum cascade laser at the 4.3um wavelength in 1994 [14]. This is a milestone in the development of mid-IR laser.

Fig. 5-1 [15] shows the difference between traditional diode laser (Fig. 5-1(a)) and quantum cascade laser (Fig. 5-1(b)). In diode laser, the light emission is due to the electron-hole recombination which depends on the bandgap of the semiconductor. The gain is limited by the absorption coefficient of the band structures. In this case, one photon is generated by one electron-hole pairs during the recombination event above the threshold. For QCL, the light is emitted by quantum jumps between subbands which is defined by the thickness. The gain is limited by the electron density in the excited state, for example, the maximum current one can injected. And each electron injected above the threshold can generate N photons. N is the number of stages.

The QCL has many advantages. The flexible design can cover a wide range of spectrum range from mid-IR to THz. And its wavelength is tunable by changing the working temperature. The output power is high and it can work in room temperature for mid-IR laser. Distributed feedback (DFB) quantum cascade lasers were first commercialized in 2004 [16], and broadly-tunable external cavity quantum cascade

lasers first commercialized in 2006 [17]. The high optical power output, tuning range and room temperature operation make QCLs useful for spectroscopic applications such as remote sensing of environmental gases and pollutants in the atmosphere[18] and homeland security. They may eventually be used for vehicular cruise control in conditions of poor visibility, collision avoidance radar, industrial process control, and medical diagnostics such as breath analyzers. QCLs are also used to study plasma chemistry. Their large dynamic range, excellent sensitivity, and failsafe operation combined with the solid-state reliability should easily overcome many of the technological hurdles that impede existing technology in these markets. When used in multiple-laser systems, intrapulse QCL spectroscopy offers broadband spectral coverage that can potentially be used to identify and quantify complex heavy molecules such as those in toxic chemicals, explosives, and drugs [19].

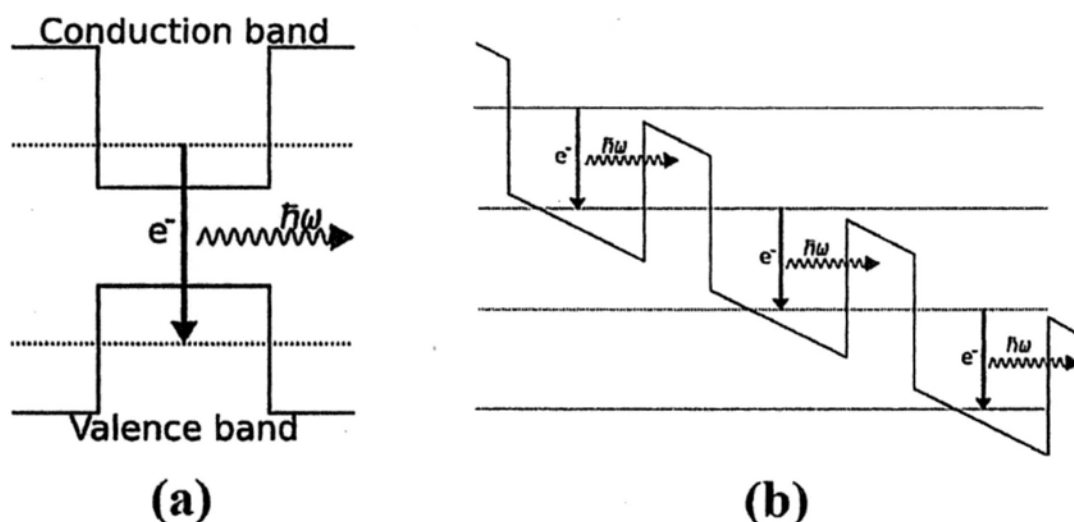


Fig. 5-1 (a) Interband transition in conventional semiconductor laser; (b) intersubband transition in quantum cascade laser.

5.2.2 Laser fabrication and characterization

The wafer we used in our experiment is bound-to-continuum design with broad gain at around 10 μ m wavelength which is identical to Ref. [20]. Fig. 5-2 shows the schematic of the quantum well structure. The 35 stages of AlGaAs-InGaAs quantum cascade lattice is the gain region of the laser. Above the active region, there is a 3 μ m InP:Si cladding layer and a 1 μ m InP:Si plasmon layer. We also fabricate our sample in THz range whose structure is based on GaAs multi quantum well with 10 μ m-thick active region on which is a 5 μ m cladding layer.

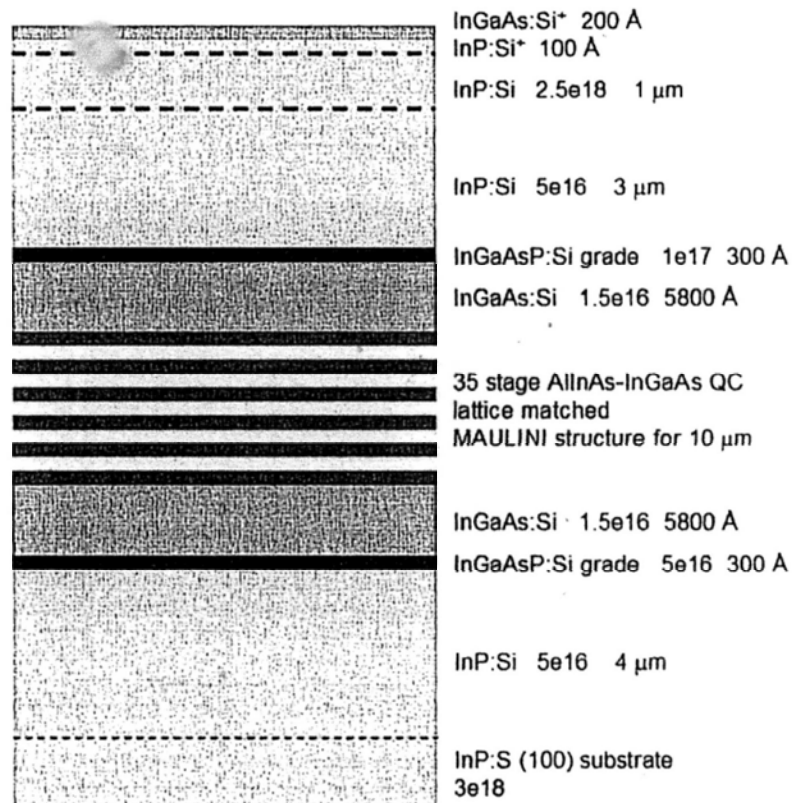


Fig. 5-2 QCL with bound-to-continuum design for broad gain at 10 μ m wavelength.

Before the fabrication of the QCL structure, we fabricate the nano grating on top

of the gain region first. For the principle of the design, we will discuss in the next section. The fabrication process is performed mainly by electron beam lithography (EBL). The process is shown by Fig. 5-3. It includes the following steps:

Step#1: InGaAs top protection layer etching (not shown by the figure). The top InGaAs layer will stop the etching of InP so we have remove this layer first. We mix the etchants (50mL water+10mL HBr+20mL Bromide water) in this order. Etch the sample for 30-60s then rinse in water.

Step#2: Thin down the InP layer by using hydrochloric acid (HCl). The etchant is prepare by mixing HCL and DI water with 1:1. Clean the sample by plasma cleaner after the etching.

Step#3: Reactive Ion Etching (RIE) process to thin down the InGaAs layer.

Step#4: Plasma-enhanced chemical vapor deposition (PECVD) for depositing silicon nitride (SiN) layer for mask of RIE.

Step#5: Grating pattern writing. Electron beam lithography (EBL) is applied for this process and the ebeam resist is PMMA 495A for our process.

Step#6: RIE process to etch down the InGaAs layer above the active region and the SiN. Then remove SiN also by RIE.

The grating is done after these processes.

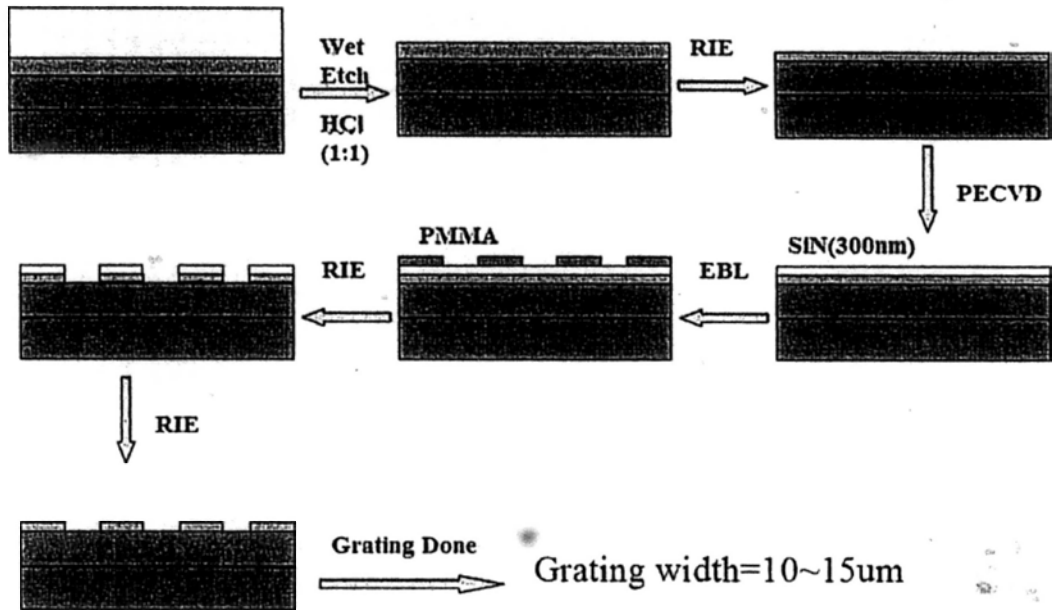


Fig. 5-3 Fabrication of nano grating on active region of QCL.

The fabrication process for mid-IR QCL is shown by Fig. 5-4 which is a standard process for QCL fabrication. The whole process includes the following steps:

Step#1: Photolithography to define the ridge waveguide. Before we start the photolithography process, we put the bare wafer in beaker with acetone for 30s. Immediately after this, put the sample in beaker with isopropanol for 15s then blow dry sample with nitrogen gun. We use the photoresist (PR) S1822 with primer LOR3A for adhesive. Under the spinner setting of 4000rpm/40s, we can get a 2.2 μ m-thick resist layer.

Step#2: Laser ridge etching. The etchant is mixed by 50mL water+10mL HBr+15mL Bromide water. After the etching process, strip the PR using acetone and isopropanol. To make sure there is no PR remains, O₂ plasma cleaning is performed.

Step#3: SiN deposition by PECVD. This layer of SiN is for isolation of the electrode with the active layer.

Step#4: Another round of photolithography to define the metal contact region for injection of electron. PR maP1275 is applied in this process. It is basically the same with the previous step.

Step#5: Passivation by RIE. Etch the exposed SiN layer.

Step#6: Top metallization. This step includes two processes. We firstly define the gap between different ridge waveguide by PL. Then one layer of gold is deposited by ebeam evaporation. At the end, liftoff is performed to isolate the ridge waveguides.

Step#7: Backside thinning and backside contact. After this, cleave the waveguide for ridge length definition and mount the laser for testing.

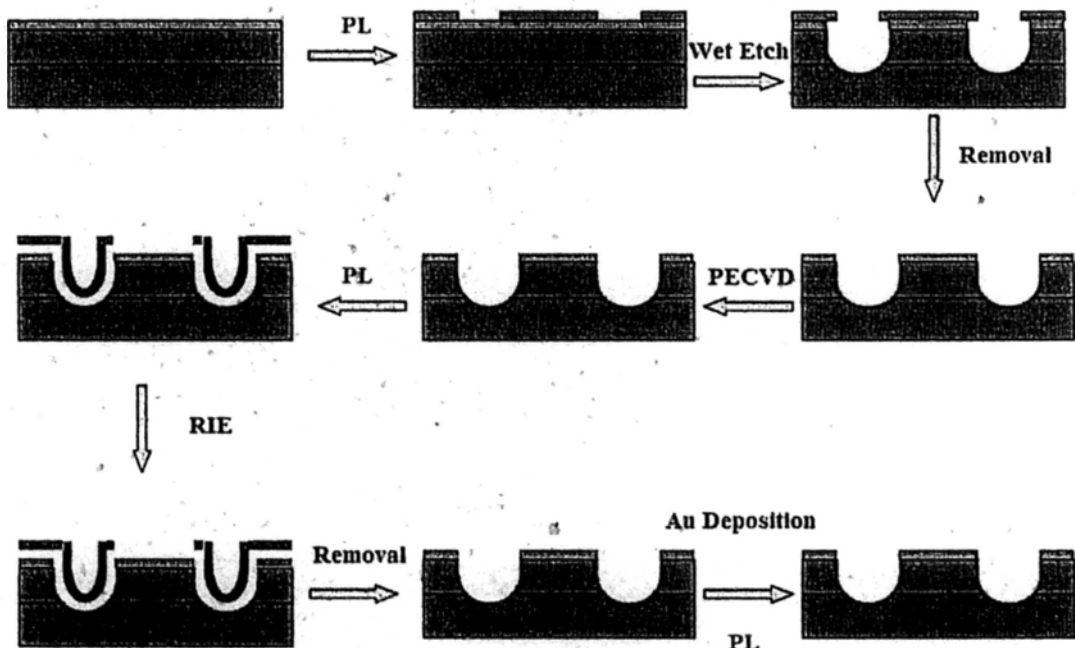


Fig. 5-4 Fabrication process for mid-IR QCL

After the device is prepared, we measure the spectrum of the laser in a commercialized model of fourier transform infrared (FTIR) spectroscopy system which is shown by Fig. 5-5 as an example. The system is provided by Bruker Inc.

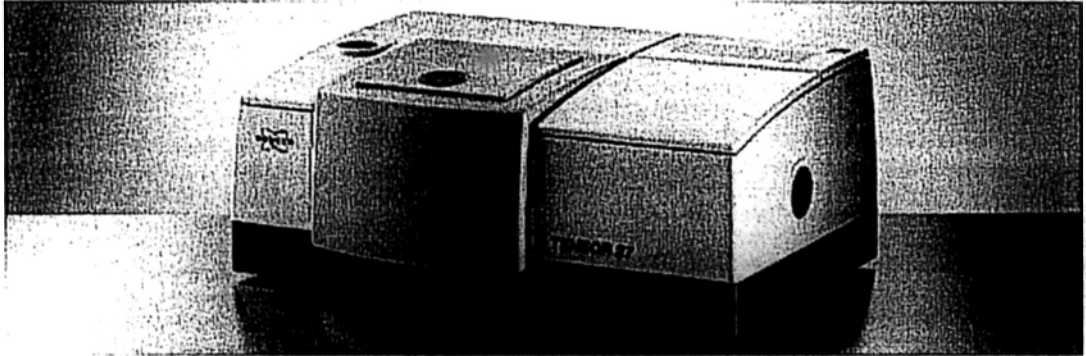


Fig. 5-5 FTIR manufactured by Bruker Inc.

The fabrication of the laser is quite complicated though the number of steps is limited. But attention to the details during the process is very critical. For the fabrication of THz QCL, the process is similar but with simpler details since the wavelength is much longer than mid-IR. But characterization of THz QCL is more complicated since low-temperature bolometer is needed as THz detector.

5.3 Plasmon laser based on 1D deep subwavelength grating

With the discussion on the basics of spoof surface plasmon, theoretical fundamentals for this part is clear. In this section, we combine the active medium in mid-IR and THz with the spoof surface plasmon structures. The introduction of metal structure in the laser waveguide will make the laser properties changed a lot. The possibility of demonstrating a tiny, low-threshold QCL with plasmon lasing is demonstrated. The experimental result will be presented.

5.3.1 Dispersion tailoring

We simulate the propagation of the by the commercial software COMSOL and Lumerical FDTD. Fig. 5-6 shows a result for propagation for 10 μ m-wavelength TM-mode wave in QCL waveguide. The far field profile is also shown in this figure.

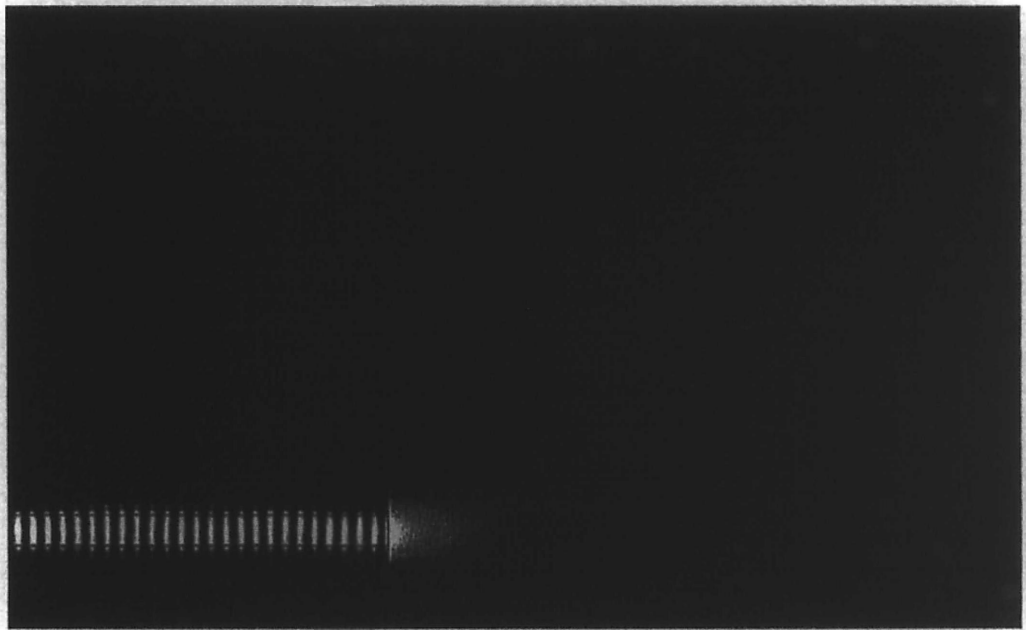
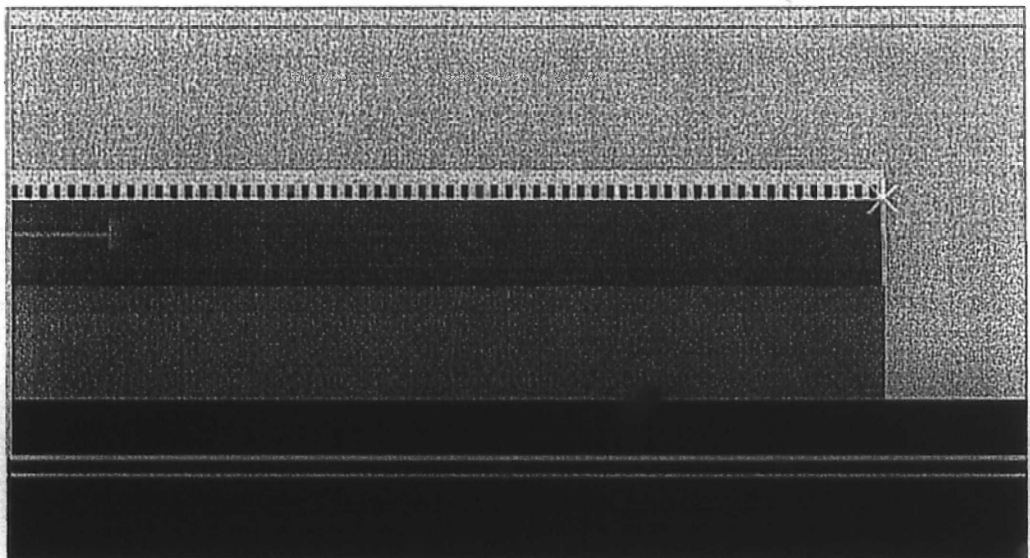
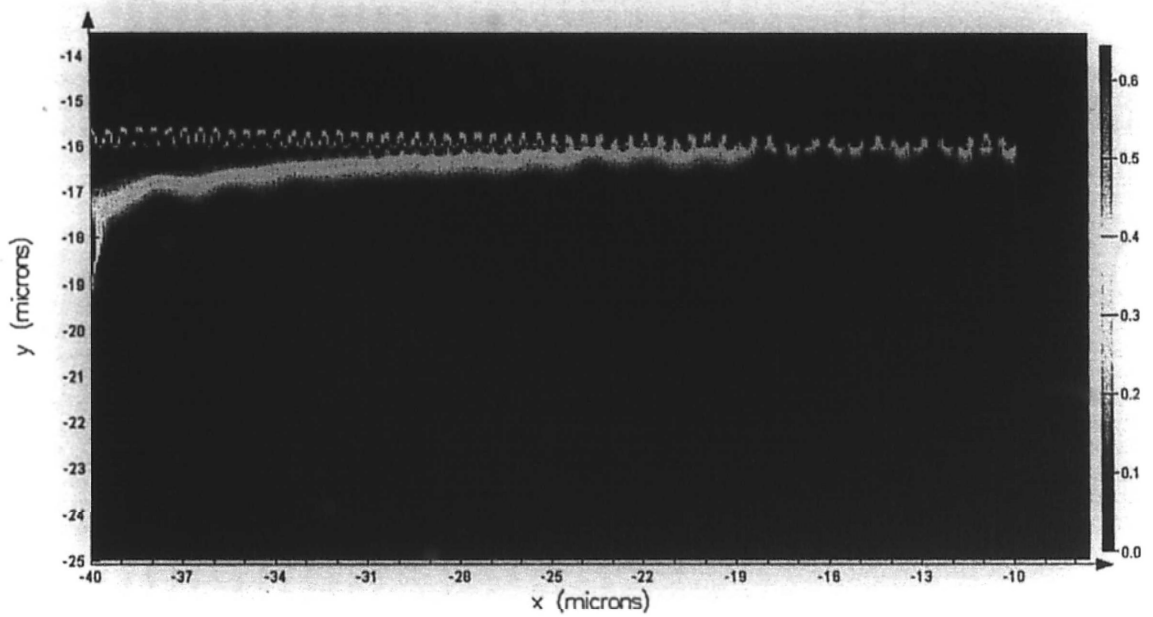


Fig. 5-6 Propagation and emission in QCL waveguide.



(a)



(b)

Fig. 5-7 (a) Model setup in FDTD. (b) Propagation of spoof surface plasmon in QCL.

By introducing the deep subwavelength metal grating, the spoof surface plasmon is excited. A proof-of-concept simulation is performed in Lumerical FDTD. Fig. 5-7 shows the simulation model setup in FDTD (Fig. 5-7(a)) and the result (Fig. 5-7(b)) in the high-loss region of the dispersion curve. As we mentioned in chapter 2, the grating can be treated as coupled nano cavities. Each cavity is formed by the bottom of the metal and the open end of the grating and the waveguide is the MIM waveguide. The resonance in the cavity results in high loss which can be observed in Fig. 5-7. The surface wave decays fast in both y direction and x direction.

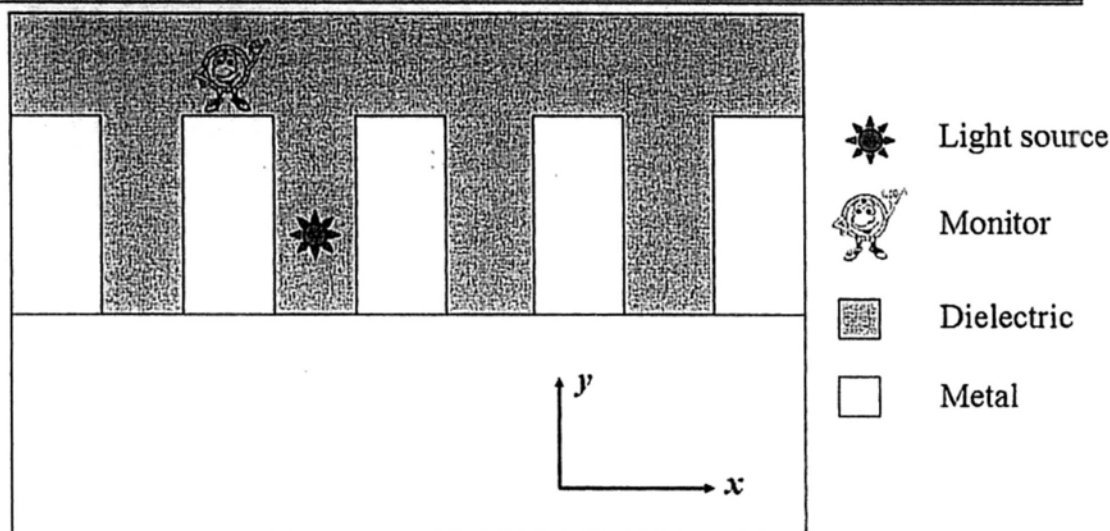
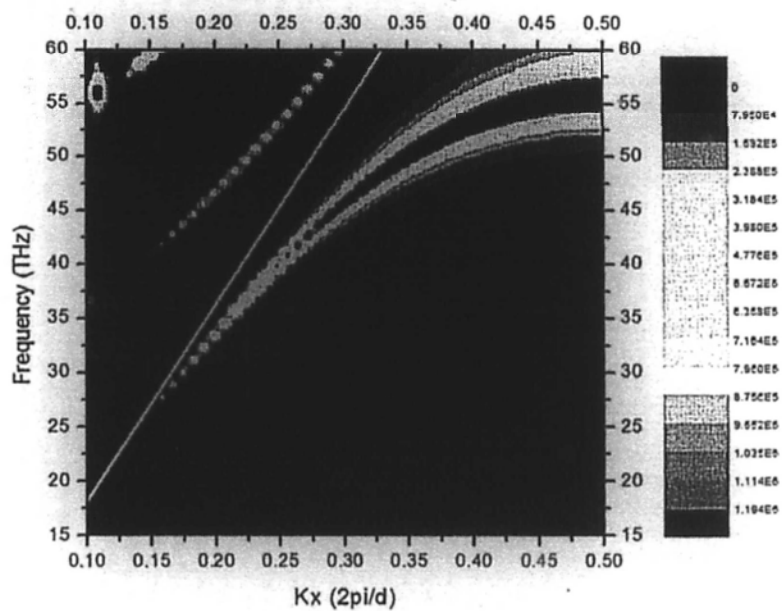
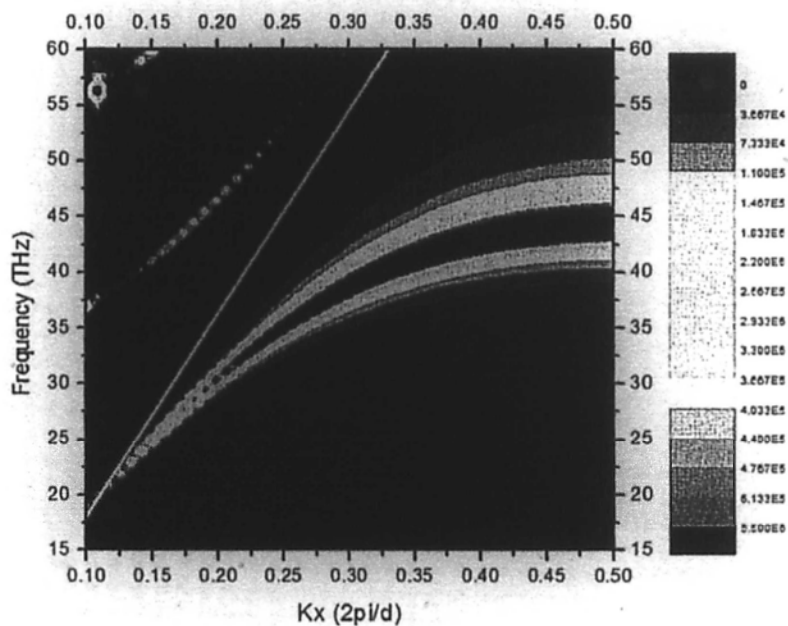


Fig. 5-8 Simulation setup for calculating the dispersion of the metallic grating in Lumerical FDTD.

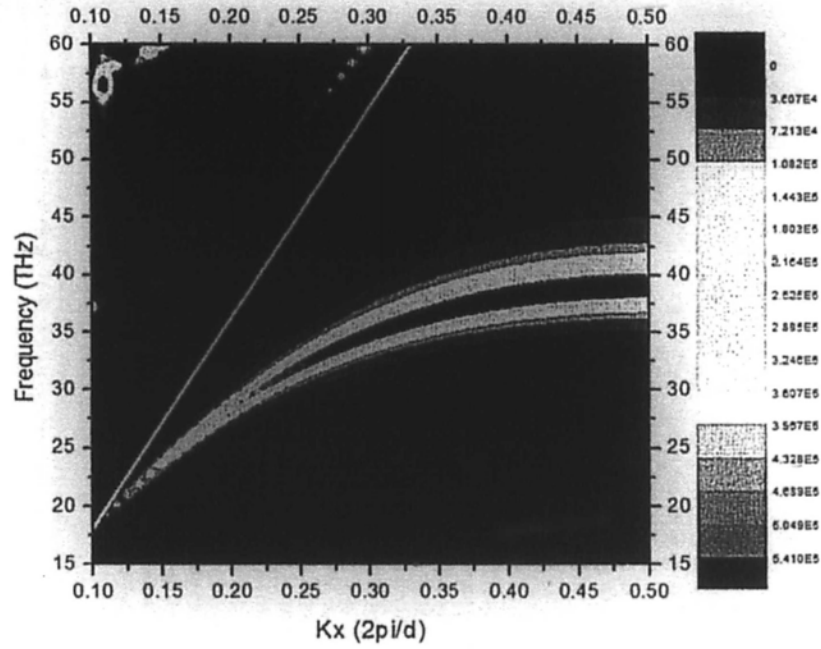
The simulation shows that the design for the QCL with grating-capped active region supports the propagation of surface plasmon. To go deeper insight of the physics and to get a practical design for experimental demonstration, quantized study is needed to determine the properties of the laser such as threshold. As we emphasized before, the dispersion of the surface plasmon is very important for its property discussion. How to calculate the dispersion of the grating? A solution is demonstrated in FDTD. The schematic of the simulation setup is shown by Fig. 5-8. The dielectric is defined by n - κ material in the software with the parameters of QCL. A point source is located in the groove and a monitor is located on top of the grating to monitor the field. Bloch boundary condition is applied to the unit cell boundary in x -direction. With different k_x , the value of the monitor will show the field intensity. When phase matching condition is satisfied, the field intensity on top of the grating will be larger than the mismatch condition. Then we can get the

dispersion relation by scanning k_x .

(a)



(b)



(c)

Fig.5-9 Simulated dispersion relation for 500nm-pitch grating with depth= (a) 250nm, (b) 400nm, (c) 500nm.

Fig. 5-9 shows the simulated result for the grating with fixed pitch (500nm) but different groove depth. The white line is the light line in dielectric. From the simulation result, we can get two primary conclusions. First, the spoof surface plasmon can be described by effective medium whose dispersion can be determined by Drude model. Since the importance of the equation for our calculation, we show the equation here again:

$$\epsilon_m(\omega) = \epsilon_{\text{inf}} - \frac{\omega_p^2}{\omega^2 + i\gamma\omega} \quad (5.1a)$$

$$k_x = \frac{\omega}{c} \left(\frac{\epsilon_m \epsilon_d}{\epsilon_m + \epsilon_d} \right)^{1/2} \quad (5.1b)$$

Another conclusion we can deduce here is that the surface plasmon frequency is

roughly inverse proportional to groove depth h , which has been shown in chapter two for the spoof surface plasmon discussion:

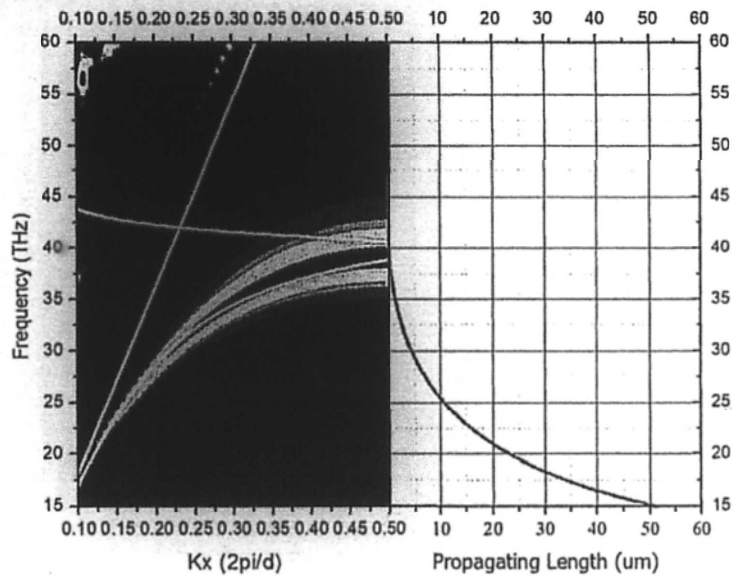
$$\omega_{sp} \propto \frac{\pi c}{2h}. \quad (5.2)$$

Through the dimension of the structure, we can tailor the dispersion curve to make the laser waveguide work with different mode index.

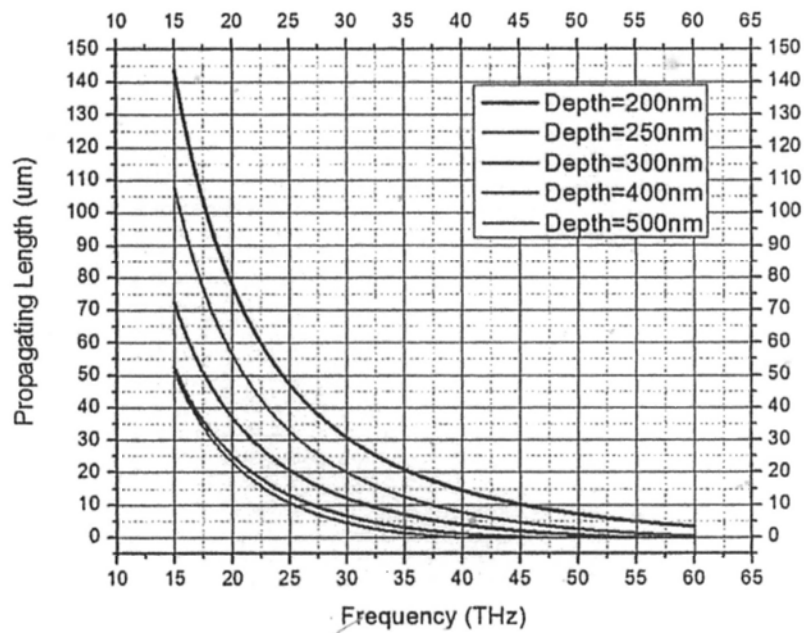
5.3.2 Group velocity and loss

In QCL, the major loss comes from the material loss and the mirror loss related to the reflection of the facet of the laser waveguide can be ignored. Then our discussion on the waveguide loss makes sense to the actual properties of the laser performance. According to basic laser theory, the laser gain is inverse proportional to the group velocity. The surface plasmon can get a much larger propagating constant which potentially results in large gain in the laser. But an interesting argument here is that when the group velocity becomes larger, according to the dispersion relation, the loss also greatly increased. Then how does these two factors be balance in the plasmon laser?

We treat the deep subwavelength gratings as effective metals described by Drude model. Then we have an effective ϵ_{inf} , ω_p and γ . The first two parameters are mainly determined by the dispersion curve shown in Fig. 5-9. The damping rate is determined by the propagating length of the waveguide which has a direct relation with the imaginary part of k_x .



(a)



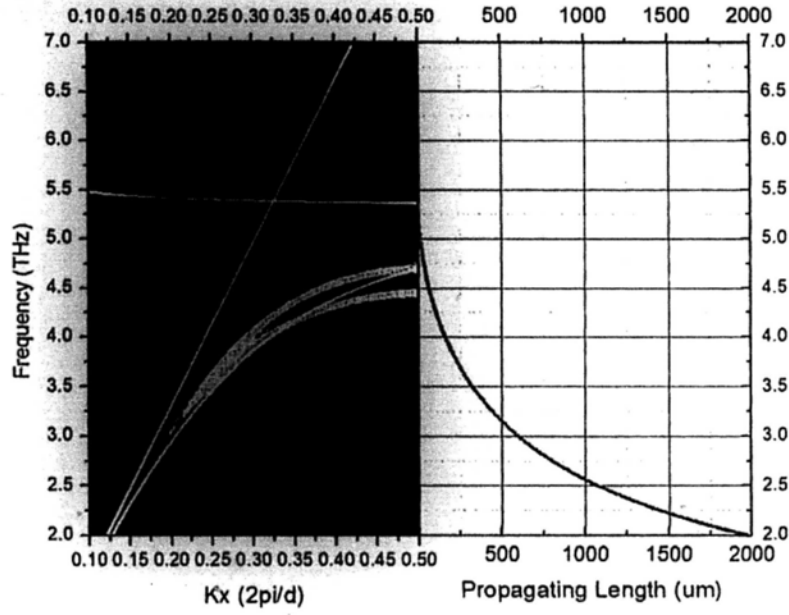
(b)

Fig. 5-10 (a) The simulation result (color 3D image) and Drude model fitting curve (white line) for 500nm-pitch grating with depth=500nm. (b) Propagating length in different groove depth.

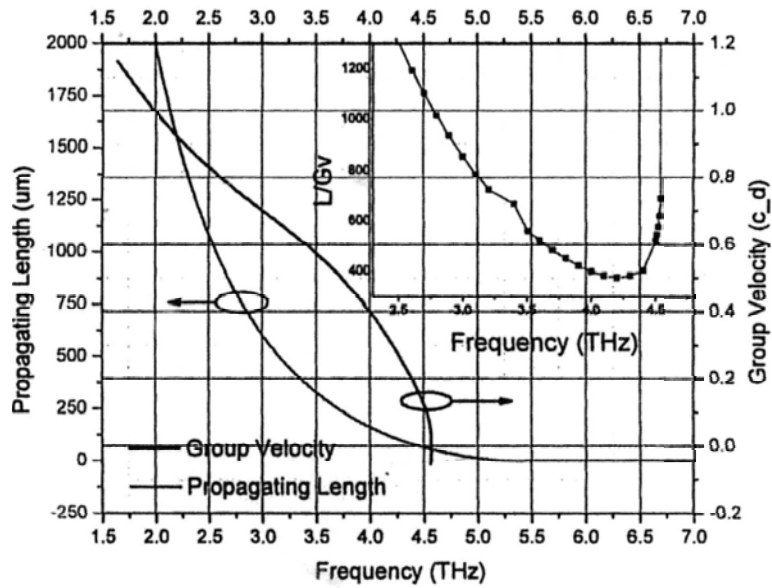
Fig. 5-10 shows the result in mid-IR range. The effective Drude metal fit the

grating dispersion quite well in this case. Fig. 5-10(a) reflects that with the increase of the k -momentum of the surface wave, the propagating length dramatically decreased. At the frequency of 30THz corresponding to 10 μ m wavelength, the loss coefficient, which is defined as the imaginary part of the k -vector, can reach as large as 1000 cm^{-1} . But it is a pity that the QCL usually can only provide the gain of 40-60 cm^{-1} . Fig. 5-10(b) shows the propagating length of the surface plasmon in different groove depth. Even when the depth is 200nm, the loss coefficient still has 166.7 cm^{-1} . The introduction of metal into the active waveguide results in large loss in mid-IR range which makes the experimental consideration not so optimistic.

But for the case in THz range, since the loss of the metal is smaller, the situation is much better. Fig. 5-11 shows the simulation result for THz range. At the frequency of 3THz, the loss coefficient is 8.33 cm^{-1} which is much smaller than that in mid-IR. This value shows a potentially lasing design since the loss is much smaller than the gain in THz frequencies. For the balance between the loss and the k -vector, Fig. 5-11(b) shows the calculated group velocity and the loss versus frequencies. At low frequencies, the propagating length drops dramatically with the increase of the frequency but at this range, the group velocity just vary slowly. At higher frequencies approaching the surface plasmon frequency, the group velocity decreases dramatically with the curve approaching the surface plasmon frequency. But at this range, though the value of propagating length is small, it varies slowly. Then when our working frequency is located at this region, the increase of gain due to the decrease of group velocity is possibly overcome the variation of the loss.

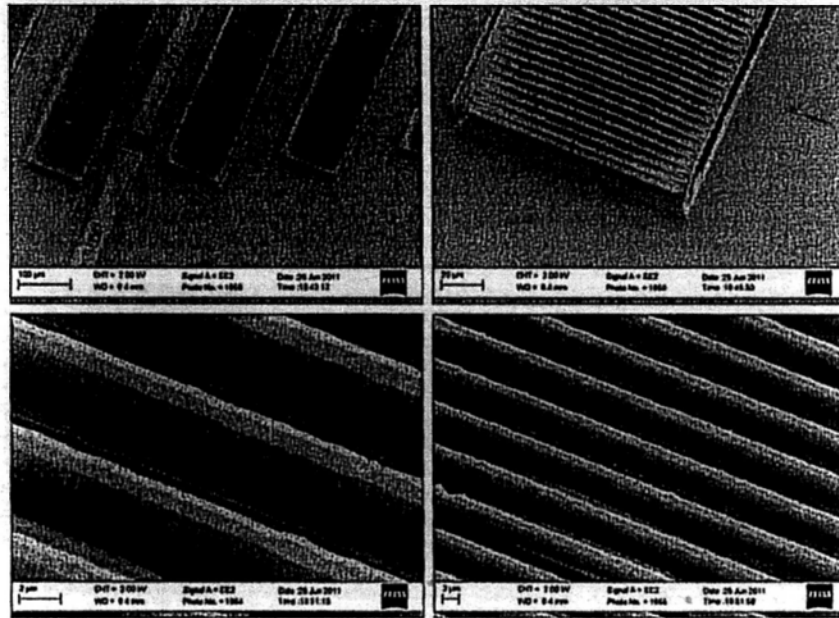


(a)

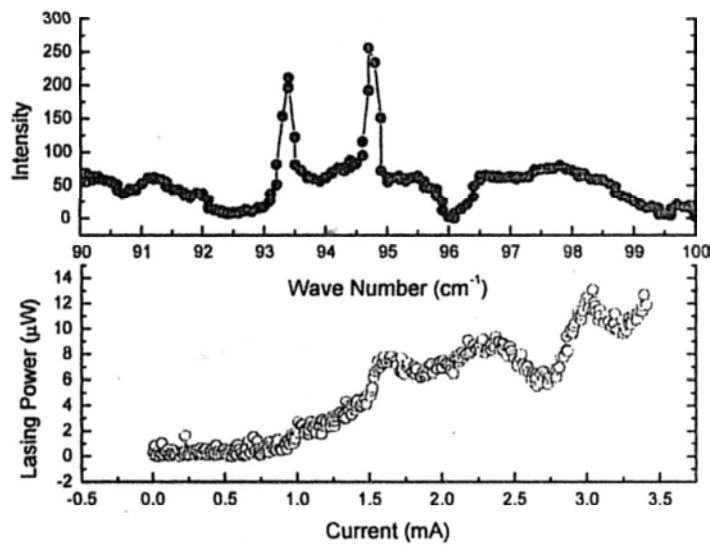


(b)

Fig. 5-11 (a) The simulation result (color 3D image) and Drude model fitting curve (white line) for 5um-pitch grating with depth=3um. (b) Group velocity and propagating length v.s. frequency.



(a)



(b)

Fig. 5-12 (a) SEM image of the SPASER chips; (b) Initial measurement result for the chip with 4.2 μ m-depth grooves.

Fig. 5-12 (a) shows the SEM image of fabricated chips. Three chips are fabricated and their groove depths are around 4.2 μ m, 4.8 μ m and 5.2 μ m, respectively.

Fig. 5-12 (b) shows a initial measurement result for the chip with 4.2 μ m-depth. The result shows the evidence of lasing in the devices. Comprehensive characterization is ongoing to elucidate the performance of these SPASERs.

5.4 Summary

By introducing the gain medium into waveguide-based cavities with spoof plasmonic structures in mid- or far-infrared range, novel devices with geometry-tailored dispersion can be demonstrated. By optimize the structure, a very good balance between the loss in the plasmonic waveguide and group velocity can be demonstrated. Inspired by the research on low threshold laser with surface plasmon propagating mode, the device in THz and mid-IR will be fabricated and tested.

References

1. Pochon, S., MacDonald, K.F., Knize, R.J., Zheludev, N.I., 2004, *Phys. Rev. Lett.* **92**, 145702.
2. Pieter Neutens, Pol Van Dorpel, Iwijn De Vlaminck, Liesbet Lagael and Gustaaf Borghs, "Electrical detection of confined gap plasmons in metal-insulator-metal waveguides," *Nat. Photonics* **3**, 283 (2009).
3. R.F. Oulton, V.J. Sorger, T. Zentgraf, R.M. Ma, C. Gladden, L. Dai, G. Bartal and X. Zhang, "Plasmon lasers at deep subwavelength scale," *Nature* **461**, 629-632 (2009).
4. Soon-Hong Kwon, Ju-Hyung Kang, Christian Seassal, Sun-Kyung Kim, Philippe Regreny, Yong-Hee Lee, Charles M. Lieber and Hong-Gyu Park, "Subwavelength Plasmonic Lasing from a Semiconductor Nanodisk with Silver Nanoparticle Cavity," *Nano Lett.* **10**, 3679 (2010).
5. Ren-Min Ma, Rupert F. Oulton, Volker J. Sorger, Guy Bartal & Xiang Zhang, "Room-temperature sub-diffraction-limited plasmon laser by total internal reflection," *Nat. Materials* **10**, 110 (2011).
6. Maziar P. Nezhad, Aleksandar Simic, Olesya Bondarenko, Boris Slutsky, Amit Mizrahi, Liang Feng, Vitaliy Lomakin and Yeshaiah Fainman, "Room-temperature subwavelength metallo-dielectric lasers," *Nat. Photonics* **4**, 395 (2010).
7. Israel De Leon & Pierre Berini, "Amplification of long-range surface plasmons by a dipolar gain medium," *Nat. Photonics* **4**, 382 (2010).

8. Soares, B.F., MacDonald, K.F., Fedotov, V.A., Zheludev, N.I., 2005, "Strong Coupling between Nanoscale Metamaterials and Phonons," *Nano Lett.* **5**, 2104.
9. Zheludev, N.I., "Single nanoparticle as photonic switch and optical memory element," *J. Opt. A: Pure Appl. Opt.* **8**, S1 (2006).
10. Jerome Faist, Federico Capasso, Deborah L. Sivco et al., "Quantum cascade laser," *Science* **264**, 553 (1994);
11. Benjamin S. Williams, "Terahertz quantum cascade lasers," *Nature Photonics* **1**, 517 (2007);
12. Kazarinov, R. F. & Suris, R. A. "Possibility of the amplification of electromagnetic waves in a semiconductor with a superlattice," *Sov. Phys. Semiconductors* **5**, 707–709 (1971).
13. F.Capasso, K.Mohammed, and A.Y.Cho, "Sequential resonant tunneling through a multiquantum well superlattice," *Appl. Phys. Lett* **48**, 478 (1986).
14. Faist, J. et al. "Quantum cascade laser," *Science* **264**, 553–556 (1994).
15. http://en.wikipedia.org/wiki/Quantum_cascade_laser.
16. "Alpes offers CW and pulsed quantum cascade lasers," *Laser Focus World*. PennWell Publications (2004).
17. "Tunable QC laser opens up mid-IR sensing applications," *Laser Focus World*. PennWell Publications (2006).
18. Normand, Erwan; Howieson, Iain; McCulloch, Michael T., "Quantum-cascade lasers enable gas-sensing technology," *Laser Focus World* **43** (4): 90 (2007).
19. Howieson, Iain; Normand, Erwan; McCulloch, Michael T., "Quantum-cascade

lasers smell success,” *Laser Focus World* **41** (3): S3 (2005).

20. R. Maulini, et al, “Broadband tuning of external cavity bound-to-continuum quantum-cascade lasers,” *Appl. Phys. Lett.* **84**, 1659 (2004).

Chapter 6: Conclusions and future work

6.1 Conclusions

Plasmonics is an exciting and fast-spreading frontier which involves rich physics, and has been not only developing a lot of novel devices for integrated optics researchers, but also getting more and more significant results in fundamental science. In our works, we build up a THz-TDS system to characterize the electromagnetic dynamics of plasmonic structures in THz range. In this thesis, we mainly investigated the planar structures in THz range. The dual-layer structure provides a versatile platform to get the multi-mode transmission in amplitude and 2π phase shift due to the coupling. These geometry-tunable properties make the structure potentially for variable planar devices such as multi-mode filter, THz wave plate, THz planar lens, sensor et al.

In communication wavelength, we propose a plasmon waveguide based on mature fiber fabrication technique with hexagonally arranged wire array. The coupling between the nano wires in fiber exhibit novel dispersion evolution with the diameter variation. This is due to the hybridization of the gap plasmon mode and the nano wire mode. The geometry study gives out a solution to reach an optimized design for the fiber-based plasmonic waveguide. Based on the studies on plasmon waveguide, plasmon cavity is investigated by FEM simulation. The result shows an

optimistic result to get a high-Q plasmonic resonator. This kind of resonator takes the advantage of traditional surface plasmon biosensor with integration potential.

At the end of this thesis, we examine the gain medium in mid-IR and THz range integrated with the surface plasmon waveguide. The samples based on mature QCL fabrication technique are being fabricated and to be tested. The high k -momentum provided by the spoof surface plasmon with an optimal low-loss design potentially leads to a low-threshold plasmon laser in THz range.

The research on surface plasmon will pave an efficient way to get the integration of photonics and electronics and results in more and more novel devices.

6.2 Future works

6.2.1 Phase engineering devices in THz range

As we mentioned chapter three, the coupling between the two layer structures provide a geometry-dependent 2π phase shift. Most dipole resonance may results in π -phase shift. Then the phase response of the dual-layer structure gives much more exotic and rich design flexibility for the phase engineering devices. We take the THz wave plate as an example to show this point.

In optical range, the $\lambda/4$ wave plate, which is shown by Fig. 6-1, can be easily demonstrated by some crystals with birefringence. But in THz range, it is not that easy. The birefringence materials and wave plate in THz range have been investigated in one dimensional photonic crystal [1] and precisely stacked quartz plate [2]. Circular single cycle THz pulse is also study [3]. Some of these designs face the problems that the structure based on complex and precisely constructed.

And some of them are based on bulk materials which will result in complex alignment in the system. For the dual-layer complementary design, since we can map all the phase depending on the geometry and polarization, we can look for any phase value in this “map” to construct the planar devices, such as half-wave plate, quarter wave plate. Another advantage for this kind of device is that it is a very thin layer compared with the wavelength then it would not change the beam path a lot. This may be convenient for the application in some well aligned system such as THz-TDS system. Based on the basic phase profiles of the geometry, we can try to design many phase-modulated planar devices such as THz planar lens.

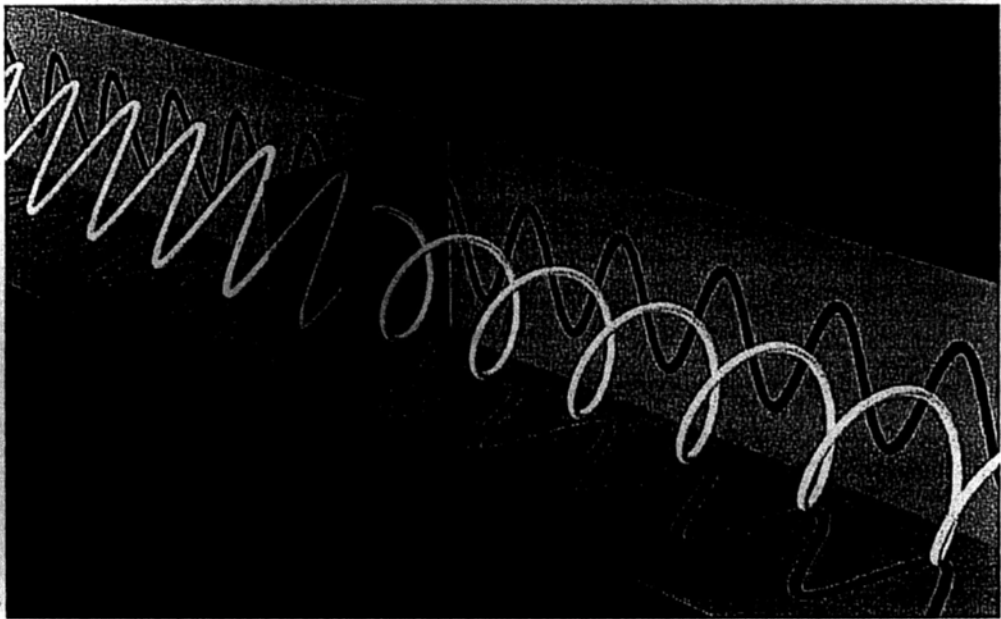


Fig. 6-1 $\lambda/4$ wave plate

6.2.2 Passive and active sensor in infrared range

We have discussed some primary simulation results in chapter four for the applications of plasmon cavity in biosensor. There has been an explosion of new and exciting science and engineering that has direct bearing on the ability of optical

biosensors to have increased and widespread applications. The inherently cross-disciplinary nature of biosensing creates fertile ground for new perspectives for addressing critical challenges. Many methods have been developed and the successful marriage of biomolecules, cells, and tissues with optoelectronic platforms provides some powerful tools to construct the detection platform. Along with the development of the research on plasmon, which is one kind of evanescently-decay electromagnetic wave existing on the interface of metal and dielectrics, surface plasmon resonance (SPR) technology has been commercialized in the past 20 years and label-free SPR biosensor have become a main tool for characterizing and quantifying biomolecular interactions both in life science and pharmaceutical research. Most of the recent SPR techniques base on the original design of the simple metal layer design though many improvements have been proposed and demonstrated, such as SPR phase measurement. Proper spatial structuration of the biofunctionalized surface into smaller subareas allows a biochip to be achieved. We plan to study how to rightly select a plasmon waveguide and optimize the coupling mechanism between the target molecule and the optical field to make the biosensor sensitivity and robust. Here we propose a method by using the plasmon waveguide and plasmonic cavity which might pave a new way to get a good label-free biosensor. The proposed method maintains advantages of SPR biosensor and potentially highly improve the sensitivity, integration and robustness than lead to an optimal solution for the SPR biosensor.

The inclusion of active components in the sensor provides another solution for

the sensor design. Rapid detection of chemical and biological samples is a purchased goal in a variety of fields, including biology, health, environmental monitoring, and homeland security. Laser based biosensors, such as Raman optical tweezers [4] and biocavity lasers [5] have been used for the detection of human blood cells. The limit for sensors bases on different mechanisms is shown by Fig. 6-2 [6]. Plasmon-based sensors including the label-free and labeled detection are close to the line of “present state of the art”. By introducing the plasmon cavity and active components, new record for the SPR-based sensor may be created.

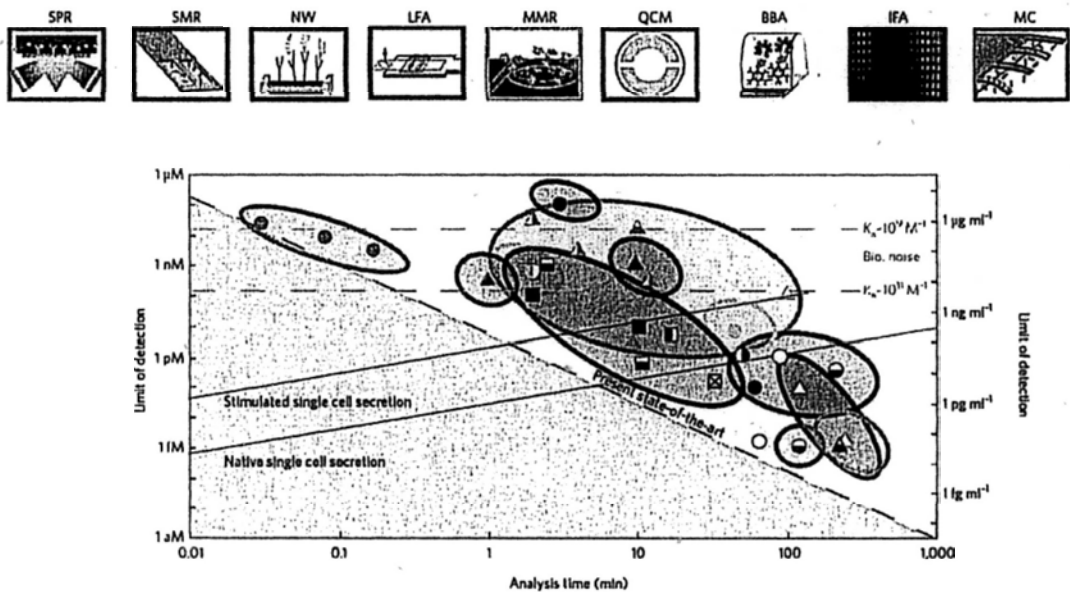


Fig. 6-2 Fluidic detection limits for protein sensing [6]

6.2.3 Nonlinearity in plasmonic structures

The efficient enhancement of nonlinearity optical phenomena in gold has been demonstrated recently [7]. In this work, a novel plasmonic structure called plasmonic nanocavity grating (PNCG) is shown to dramatically enhance surface nonlinear optical processes. It consist of resonant cavities that are periodically

arranged to combine local and grating resonance. The schematic for the structure is shown by Fig. 6-3. The four-wave mixing (FWM) signal generated in the gold nanocavity is enhanced by a factor up to 2000, two orders of magnitude higher than that previously reported.

To follow this work, the enhanced nonlinearity of the structure can be applied in observation of Raman scattering signals of molecules. A combination with the research on graphene, which is a very hot topic recently, is possible to get much more discoveries.

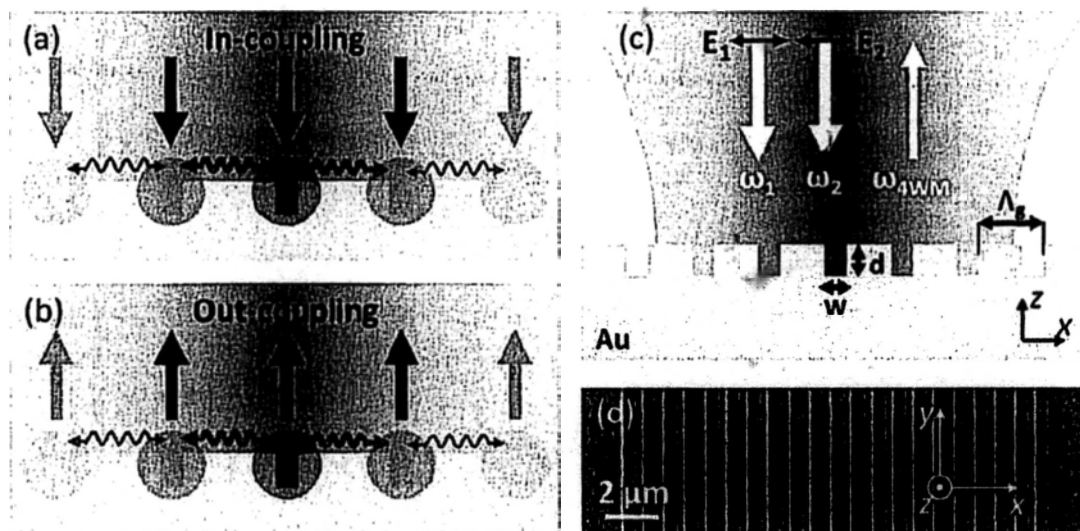


Fig. 6-3 Gratings in a metal surface can enhance nonlinearity originated from intense field enhancement involving both localized and propagating surface plasmons. (a) Light is coupled into a localized nanocavity mode, assisted by propagating surface plasmons (red wavy arrows). (b) An emitter positioned in a groove exhibits enhanced emission and collimation effect. (c) Schematic of the four-wavemixing experiment.

References

1. Maik Scheller, Christian Jördens, and Martin Koch, "Terahertz form birefringence," *Opt. Express* **18**, 10137 (2010).
2. Jean-Baptiste Masson and Guilhem Gallot, "Terahertz achromatic quarter-wave plate," *Opt. Lett.* **31**, 265(2006).
3. Jie Shan, Jerry I. Dadap, and Tony F. Heinz, "Circularly polarized light in the single-cycle limit: the nature of highly polychromatic radiation of defined polarization," *Opt. Express* **17**, 7431 (2009).
4. C. G. Xie and Y. Q. Li, "Confocal micro-Raman spectroscopy of single biological cells using optical trapping and shifted excitation difference techniques", *J. of Appl. Phys.* **93** (5), pp. 2982 (2003).
5. P. L. Gourley, "Biocavity laser for high-speed cell and tumor biology", *J. of Appl. Phys. D* **36**, R228-239 (2003).
6. J.L. Arlett, E.B. Myers and M.L. Roukes, "Comparative advantages of mechanical biosensors," *Nat. Nano.* **6**, 203 (2011).
7. Patrice Genevet, Jean-Philippe Tetienne, Evangelos Gatzogiannis, Romain Blanchard, Mikhail A. Kats, Marlan O. Scully, and Federico Capasso, "Large Enhancement of Nonlinear Optical Phenomena by Plasmonic Nanocavity Gratings," *Nano Lett.* **10**, 4880 (2010).

Publication List

1. **Zhongxiang Zhang**, Kam Tai Chan, "Polarization-dependent plasmonic coupling in dual-layer metallic structures at terahertz frequencies," *Opt. Express* **19**, 2791 (2011);
2. **Zhongxiang Zhang**, Minglie Hu, Kam Tai Chan, and Chingyue Wang, "Plasmonic waveguiding in hexagonally ordered metal wire array," *Opt. Lett.* **35**, 3901 (2010);
3. **Zhongxiang Zhang**, Kam Tai Chan, Yanxia Cui, Sailing He, Changlei Wang, Qirong Xing, Qingyue Wang, "Multimode transmission in complementary plasmonic structures at terahertz frequencies," *Appl. Phys. Lett.* Vol **96**, 073506 (2010);
4. **Zhongxiang Zhang**, Changlei Wang, Mengyu Chen, Kam Tai Chan, Qirong Xing, Minglie Hu, Qingyue Wang, "Coupled dispersive modes in dual-layer fishnet structures in terahertz regime," *Photonics Global Conference 2010*, Oral 1-4D-5, Singapore;
5. **Zhongxiang Zhang**, Kam Tai Chan, Ming Lie Hu, Chingyue Wang, "Flexible plasmonic waveguides based on metal-filled fibers," *Microoptics Conference (MOC) 2010*, HsinChu, Taiwan (invited);
6. **Zhongxiang Zhang**, Kam Tai Chan, "Parametric investigation of isotropic fishnet metamaterials in terahertz regime," *CLEO/QELS 2010 JWA121*, San Jose, U.S.;

Publication List

7. **Zhongxiang Zhang**, Minglie Hu, Kam Tai Chan, Qingyue Wang, "Plasmonic Waveguiding in Nano-metallic-wire-filled Photonic Crystal Fiber Taper," Nanophotonics 2010 Tu-A-1 O-15, Tsukuba, Japan;
8. **Zhongxiang Zhang**, Mengyu Chen, Kam Tai Chan, "Multi-Mode Resonance in Complementary Dual-Layer Sub-Wavelength Structure at THz Frequencies," OptoElectronics and Communications Conference, OECC 2009 Tu14. IEEE;
9. Mengyu Chen, **Zhongxiang Zhang**, Kam Tai Chan, "Dual-Band Polarization-Insensitive Left-Handed Metamaterial in Terahertz Range," OptoElectronics and Communications Conference, OECC 2009 Th14. IEEE;